Tesis Doctoral

Temporal Variability of Zonal Circulation and Anthropogenic Carbon in the Western North Atlantic Ocean

por

Daniel Santana Toscano

ULPGC Universidad de Las Palmas de Gran Canaria | IOCAG Instituto Universitario de Oceanografía y Cambio Global

Doctorado en Oceanografía y Cambio Global
Universidad de Las Palmas de Gran Canaria

Las Palmas de Gran Canaria, mayo de 2025

Dra. MAGDALENA SANTANA CASIANO, COORDINADORA DEL PROGRAMA DE DOCTORADO EN OCEANOGRAFÍA Y CAMBIO GLOBAL DE LA UNIVERSIDAD DE LAS PALMAS DE GRAN CANARIA

INFORMA,

De que la Comisión Académica del Programa de Doctorado, en su sesión de fecha ____ de mayo de 2025 tomó el acuerdo de dar el consentimiento para su tramitación, a la tesis doctoral titulada "*Temporal Variability of Zonal Circulation and Anthropogenic Carbon in the Western North Atlantic Ocean*" presentada por el doctorando D. Daniel Santana Toscano y dirigida por el Doctor Alonso Hernández Guerra y la Doctora María Dolores Pérez Hernández.

Y para que así conste, y a efectos de lo previsto en el Artículo 11 del Reglamento de Estudios de Doctorado (BOULPGC 04/03/2019) de la Universidad de Las Palmas de Gran Canaria, firmo la presente en Las Palmas de Gran Canaria, a ___ de mayo de dos mil veinticinco.

UNIVERSIDAD DE LAS PALMAS DE GRAN CANARIA
ESCUELA DE DOCTORADO

Programa de doctorado en Oceanografía y Cambio Global.

Título de la tesis: Temporal Variability of Zonal Circulation and Anthropogenic Carbon in the Western North Atlantic Ocean.

Tesis doctoral presentada por D. Daniel Santana Toscano.

Dirigida por el Dr. Alonso Hernández Guerra.
Codirigida por la Dra. María Dolores Pérez Hernández.

Las Palmas de Gran Canaria, a ____ de mayo de 2025.

El Director, La Codirectora, El Doctorando,

A mi familia, la de sangre y la elegida

Agradecimientos / Acknowledgements

A veces, al mirar atrás, me sorprende la cantidad de experiencias y aprendizajes que han forjado este camino. Cada paso que doy al final de esta etapa me hace recordar momentos compartidos, desafíos superados y la constante búsqueda de conocimiento que, en definitiva, me ha llevado hasta aquí.

Quiero expresar mi más profundo agradecimiento a mis directores, Alonso Hernández Guerra y Lola Pérez Hernández, quienes han sido mucho más que guías académicos desde el inicio. Su sabiduría y perspectiva no solo han enriquecido mi percepción sobre la ciencia, sino que también me han brindado una visión amplia y profunda de la vida.

Agradezco de corazón a Peter Brown, quien me acogió durante mi estancia en Southampton y facilitó de manera extraordinaria mi aprendizaje sobre el carbono antropogénico en el océano. Su generosidad y conocimientos fueron fundamentales para ampliar mis horizontes.

De la misma manera, quiero agradecer a los científicos principales responsables de la recolección de los datos de los transectos A20 y A22: T. Joyce, W. Smethie, R. Curry, V. Menezes, R. Pickart, J. Toole, A. MacDonald, M. McCartney y R. Woosley.

Un agradecimiento muy especial a María Casanova-Masjoan, cuyas sonrisas y actitud positiva echamos de menos profundamente. A Cris y Vero, quienes hicieron del doctorado un lugar ameno y estimulante (nunca faltaron los pañuelos) pese a las innumerables dudas que he tenido en mi camino. No puedo olvidar a mis amigos de la universidad, tanto a los de siempre como a los que he conocido en esta última etapa, todos ustedes siempre tendrán un huequito en mi corazón.

A mis amistades de toda la vida, y en especial a Diego, gracias por estar a mi lado en los momentos más oscuros y por celebrar conmigo en los instantes de mayor alegría. Tu apoyo incondicional ha sido como un salvavidas para un náufrago.

A Sara, quien desde el primer momento ha visto en mí mi mejor versión. Gracias a ti la vida se siente como una noche de Luna llena en un mar calmado de verano. Contigo sé que cualquier camino que elija, será el correcto.

Finalmente, mi gratitud es infinita para mi familia. A todos ustedes, gracias por el apoyo y el interés inquebrantable hacia todo aquello que amo. A mi hermano, por enseñarme que tropezar mil veces en el camino no te hace menos valiente, siempre y cuando te levantes mil y una. A mi hermana, por hacerme mejor persona, por mantener mis pies en la tierra y por sacarme una sonrisa cuando más lo necesitaba. A mis padres, por inculcarme los valores que abrazo cada día, por impulsarme a perseguir mis sueños desde el principio y por brindarme un cariño y un apoyo incondicionales.

A todos, gracias por ser parte esencial de este viaje.

Abstract

The North Atlantic Subtropical Gyre (NASG) plays a key role in large-scale ocean circulation and climate regulation, particularly through its connection to the Atlantic Meridional Overturning Circulation (AMOC). This thesis investigates the physical and biogeochemical dynamics of the western NASG, with a focus on zonal circulation, heat and freshwater transport, and anthropogenic carbon (C_{anth}) trends. To achieve this, the study utilizes hydrographic data from the A20 and A22 sections, collected in 1997, 2003, 2012, and 2021, combined with inverse box modeling techniques. A key methodological advancement is the application of a three-box inverse model, which improves upon single-box approaches by incorporating additional observational constraints, thereby enhancing estimates of mass transport and variability at decadal scales. These results are further compared with numerical models, including GLORYS, ECCO, and MOM, to evaluate their ability to reproduce observed transport patterns. Findings reveal that while individual currents such as the Gulf Stream (GS) and Deep Western Boundary Current (DWBC) exhibit seasonal and interannual variability, their long-term average transports remain consistent with previous estimates, supporting the robustness of the inverse box model methodology. The GS is identified as the dominant carrier of heat and freshwater poleward, while the DWBC serves as the primary conduit for southward export of dense water, forming the lower limb of the AMOC. The estimated heat fluxes indicate a net ocean-to-atmosphere exchange at the A20 section, with variability across different survey years reflecting the influence of atmospheric forcing. Freshwater fluxes suggest an overall increase in precipitation and runoff relative to evaporation over the decades, a trend corroborated by reanalysis products. In addition to circulation, the thesis examines the role of the western NASG in C_{anth} uptake and transport. Results indicate that the GS and North Atlantic Current play a crucial role in advecting C_{anth}-rich waters from subtropical to subpolar regions, contributing to the long-term sequestration of atmospheric CO_2. Rising CO_2 levels worsen ocean acidification—evidenced by significantly fewer carbonate ions and a shoaling aragonite horizon—making high-resolution monitoring essential for future predictions.

Contents

AGRADECIMIENTOS / ACKNOWLEDGEMENTS III

ABSTRACT V

CONTENTS VII

CHAPTER 1: INTRODUCTION 1

1.1 Atlantic Ocean Dynamics 1
1.2 Observational Programs: From WOCE-WHP to GO-SHIP 2
1.3 Advancements in Inverse Modeling: From Single to Three-Box Approaches 3
1.4 The NASG in the Global Carbon Cycle and Ocean Acidification .. 3
1.5 Research Motivation 4
1.6 Thesis Outline 4

CHAPTER 2: ZONAL FLOW PATTERNS IN THE NORTH ATLANTIC AT 52°W 5

2.1. INTRODUCTION 7

2.2. DATA AND METHODS 8

2.2.1 Hydrographic Data 8
2.2.2 Numerical Ocean Model Data 12
2.2.3 Geostrophic Transport and Inverse Model 13

2.3. RESULTS 20

2.3.1 Adjusted Geostrophic Transport 20
2.3.2 Heat and Freshwater Transports 26

2.4. DISCUSSION 30

CHAPTER 3: ZONAL CURRENTS IN THE WESTERN NORTH ATLANTIC GYRE (2021): SINGLE- VS. THREE-BOX MODELS 35

3.1. INTRODUCTION 37

3.2. DATA AND METHODS 42

3.2.1 Hydrographic Data 42
3.2.2 Geostrophic Transport 45
3.2.3 Inverse Box Model 47

3.3. RESULTS 52

3.3.1 Adjusted Zonal Circulation 52
3.3.2 Heat and Freshwater Fluxes 55

3.4. DISCUSSION 59

CHAPTER 4: ANTHROPOGENIC CARBON TRENDS IN THE WESTERN NASG 67

4.1. INTRODUCTION **69**

4.2. DATA AND METHODS **71**

4.2.1 HYDROGRAPHIC DATA 71
4.2.2 ATMOSPHERIC DATA 73
4.2.3 GEOSTROPHY AND INVERSE MODEL 73
4.2.4 C_{ANTH} ESTIMATIONS 76

4.3. RESULTS **77**

4.4. DISCUSSION **83**

CHAPTER 5: CONCLUSIONS **89**

APPENDIX A: DATA AVAILABILITY **89**

APPENDIX B: THREE-BOX INVERSE MODEL **90**

APPENDIX C: RESUMEN EN CASTELLANO **95**

BIBLIOGRAPHY **97**

Chapter 1: Introduction

1.1 Atlantic Ocean Dynamics

The Atlantic Ocean's dynamic circulation is fundamentally shaped by its wide basin configuration, the presence of the Mid-Atlantic Ridge, and the pronounced influence of wind-driven processes (Talley et al., 2011). At the surface, large-scale gyres and zonal currents emerge from the interaction between prevailing winds and the Earth's rotation. In the subtropical regions, anticyclonic gyres—such as those found in the North and South Atlantic—play a decisive role in transporting warm, saline waters across vast distances (Bower et al., 2019; Schott et al., 2004). In contrast, the subpolar regions are dominated by cyclonic gyres that help redistribute cooler waters along the continental margins (Hátún et al., 2005).

Within this dynamic framework, the North Atlantic Subtropical Gyre (NASG) is of particular significance. The western portion of the NASG is characterized by the robust and energetic Gulf Stream (GS), which efficiently transports warm water (Joyce & Zhang, 2010). As these surface waters progress into higher latitudes, they undergo significant modifications through interactions with the atmosphere and the ocean's inherent buoyancy forces. Specifically, as the warm water loses heat via air–sea interactions, it undergoes convective overturning, evaporation, and cooling, which in turn increases its density (Talley et al., 2011). This transformation is a central process in the formation of deep water masses, such as the North Atlantic Deep Water (NADW), that contribute to the Atlantic Meridional Overturning Circulation (AMOC). The conversion of relatively light, warm surface waters into denser intermediate and deep waters is not merely a local phenomenon; it is a critical mechanism that sustains the overall structure of the AMOC. As the waters cool and become denser, they subduct and join the deep circulation pathways, ultimately flowing along the continental margins as part of the Deep Western Boundary Current (DWBC; Bower & Hunt, 2000). This process effectively links the vigorous, wind-driven surface circulation with the slower, buoyancy-controlled deep ocean currents, ensuring the continuous redistribution of thermal energy and salt throughout the Atlantic basin. Variations in the rate and efficiency of water mass transformation—often modulated by atmospheric variability such as the North Atlantic Oscillation

(NAO)—carry profound implications for both regional climate dynamics and the long-term stability of the AMOC (Schott et al., 2004).

1.2 Observational Programs: From WOCE-WHP to GO-SHIP

The evolution of our understanding of the AMOC and more regional circulation as the NASG has been greatly enhanced by a series of coordinated international observational programs. From 1990 to 2002, the World Ocean Circulation Experiment Hydrographic Program (WOCE-WHP) systematically collected and analyzed hydrographic data from across the globe. This initiative laid the foundation for later programs such as the Climate and Ocean: Variability, Predictability and Change (CLIVAR) and the Global Ocean Ship-based Hydrographic Investigations Program (GO-SHIP), which have continued the legacy of standardized ship-based surveys and open-access data sharing.

These programs have enabled interannual comparisons and fostered global collaboration by merging the contributions of individual countries, thereby providing a comprehensive view of ocean circulation and variability. Among the standardized hydrographic sections, the A20 and A22 meridional sections have emerged as key observational transects in the western NASG. The A20 section, located along 52°W, traverses the primary currents of the AMOC—including the GS and the DWBC. Since its first sampling in 1997, and with subsequent reoccupations in 2003, 2012, and 2021 (Santana-Toscano et al., 2023), the A20 section has provided decadal-scale resolution to investigate changes in the NASG's circulation and its interaction with the broader climate system.

Complementing the A20 section is the A22 section, located at 66°W. Together, these transects not only capture the principal pathways of the GS and DWBC but also extend into the Caribbean Sea, thereby offering a more complete picture of the western boundary dynamics of the NASG. Data collected from these sections have been instrumental in estimating mass transports using inverse box modeling techniques—a methodology that also quantifies oceanic heat and freshwater fluxes by balancing mass inflows and outflows across the sections (Casanova-Masjoan et al., 2018; Hall, 2004; Joyce et al., 2001; Santana-Toscano et al., 2023).

1.3 Advancements in Inverse Modeling: From Single to Three-Box Approaches

Traditional approaches to estimating the transport of key currents in the NASG have relied on single-section, one-box inverse models. Although these models yield valuable insights into the transport values for the GS, DWBC, and regional currents like the North Brazil Current (NBC) and the North Equatorial Current (NEC), they are inherently limited. Single-section models are susceptible to aliasing and tend to capture only a snapshot of the ocean's state during the specific period of a cruise (Caínzos et al., 2023). In response to these limitations, in this work we have introduced a significant methodological advancement by employing a three-box inverse model. This approach integrates data from both the A20 and A22 sections—sampled most recently in 2021—to account for interactions between the sections and their respective boundary regions.

1.4 The NASG in the Global Carbon Cycle and Ocean Acidification

Beyond its role in ocean circulation, the NASG is a critical component of the global carbon cycle. The subtropical North Atlantic is among the strongest oceanic carbon dioxide (CO_2) sinks, largely due to its efficient uptake of atmospheric CO_2—a process driven by low Revelle factors and favorable physical conditions that enhance the solubility of CO_2. Once absorbed, the anthropogenic CO_2 (C_{anth}) is transported poleward by the GS and subducted during deep-water formation in the subpolar regions (Khatiwala et al., 2013; Sabine et al., 2004).

This poleward transport and subsequent subduction play a key role in sequestering CO_2 from the atmosphere, thereby mitigating the impacts of climate change. However, the capacity of the NASG to act as a carbon sink is subject to significant seasonal and interannual variability, influenced by factors such as air-sea disequilibria, temperature fluctuations, biological processes, and physical drivers like the NAO and AMOC (García-Ibáñez et al., 2016; Gruber et al., 2019; Pérez et al., 2018).

Ocean acidification (OA) adds another layer of complexity to the carbon dynamics of the western NASG. The increasing atmospheric CO_2 levels are not only enhancing the ocean's capacity to absorb CO_2 but are also altering the marine carbonate system. The reduction in the buffering capacity of seawater leads to changes in pH and decreases in carbonate ion concentrations ($[CO_3^{2-}]$), which in turn can accelerate the shoaling of the aragonite saturation horizon, which is the depth where the aragonite begins to dissolve rather than precipitate —a phenomenon with profound implications for marine ecosystems (Caldeira & Wickett, 2003; Doney et al., 2009). In this context, understanding the fine-scale distribution, transport, and temporal evolution of C_{anth} is critical. Traditional ship-based measurements, complemented by innovative tools such as Argo-O_2 floats and neural network-based estimation methods, are beginning to shed light on these complex processes (Asselot et al., 2024; Talley et al., 2016).

1.5 Research Motivation

The primary objective of this thesis is to advance our understanding of the western NASG by examining its physical dynamics, its role in the AMOC, and its significance in the global carbon cycle. To further this aim, the research also focuses on methodological advancements in transport estimation by implementing a three-box inverse model that integrates data from both the A20 and A22 sections, thereby enhancing our ability to estimate mass transports compared to traditional single-section inverse models (Caínzos et al., 2023). Additionally, the thesis investigates the contribution of the western NASG to the global carbon cycle, particularly in terms of C_{anth} uptake and transport, and explores the implications of ocean acidification on the carbonate system in this region, including how changes in circulation patterns might affect the long-term sequestration of atmospheric CO_2 (Doney et al., 2009; Khatiwala et al., 2013; Sabine et al., 2004).

1.6 Thesis Outline

This thesis examines zonal circulation and carbon trends in the western NASG. Chapter 2 studies temporal changes along the A20 section at 52°W using hydrographic data and inverse modeling to quantify mass, heat, and freshwater transports. Chapter 3 compares single-box and three-box inverse models using 2021 data from the A20 and A22 sections. Chapter 4 explores C_{anth} trends by estimating carbon inventories and evaluating how circulation changes affect carbon sequestration and ocean acidification.

Chapter 2: Zonal Flow Patterns in the North Atlantic at 52°W

This chapter has been published as:

Santana Toscano, D., Pérez Hernández, M.D., Macdonald, A. M., Arumí Planas, C., Caínzos Díaz, V., Hernández Guerra, A. 2023. Zonal Circulation in the North Atlantic Ocean at 52°W from WOCE-WHP and CLIVAR sections: 1997, 2003 and 2012 https://doi.org/10.1016/j.pocean.2023.103069

2.1. Introduction

From 1990 to 2002 the World Ocean Circulation Experiment Hydrographic Program (WOCE-WHP) collected and analyzed hydrographic data across the globe. This experiment set the basis for the later Climate Variability Hydrographic Program (CLIVAR). All international, WOCE-WHP and CLIVAR have globally organized ship-based hydrographic surveys and have established standard sections that have allowed interannual comparisons. In addition, by creating an open-access database, they have merged the effort of individual countries and have given visibility to single surveys.

The meridional A20 section is located along 52ºW, in the western North Atlantic Subtropical Gyre (NASG), where the main currents of the Atlantic Meridional Overturning Circulation (AMOC) are present (Fig. 2.1). It was firstly sampled in 1997, and, later, in fall of 2003 and spring of 2012. The western basin of the NASG is the main route for the warm poleward waters that feed the upper limb of the AMOC. The Gulf Stream (GS) is the main current flowing towards higher latitudes along the North American slope. The GS splits into two branches, the weaker branch recirculates to the eastern Subtropical Gyre and the stronger one flows northward to high latitudes (Pérez-Hernández et al., 2013; Vélez-Belchí et al., 2017; Worthington, 1976). This stronger branch exchanges heat with the atmosphere and becomes colder, denser and, therefore, sinks into deep layers of the ocean forming the Deep Western Boundary Current (DWBC; Casanova-Masjoan et al., 2020; Pérez-Hernández et al., 2019; Reid, 1994; Schott et al., 2004; Våge et al., 2013). The DWBC forms the lower limb of the AMOC and is the main southward flow carrying dense cold water formed at high latitudes through the western NASG Gyre (Bower et al., 2019; Munk, 1950; Reid, 1994; Schott et al., 2004; Stommel et al., 1958; Stommel, 1948).

In this work, the main goal was to quantify the circulation pattern in the western boundary of the NASG and to estimate the changes in the main components of the AMOC using the three A20 hydrographic sections carried out in 1997, 2003 and 2012. These results are compared with output from climatology-forced and ocean reanalysis models to determine which had better agreement with the results from in-situ observations. Heat and freshwater transports are estimated and compared with the output of the numerical models.

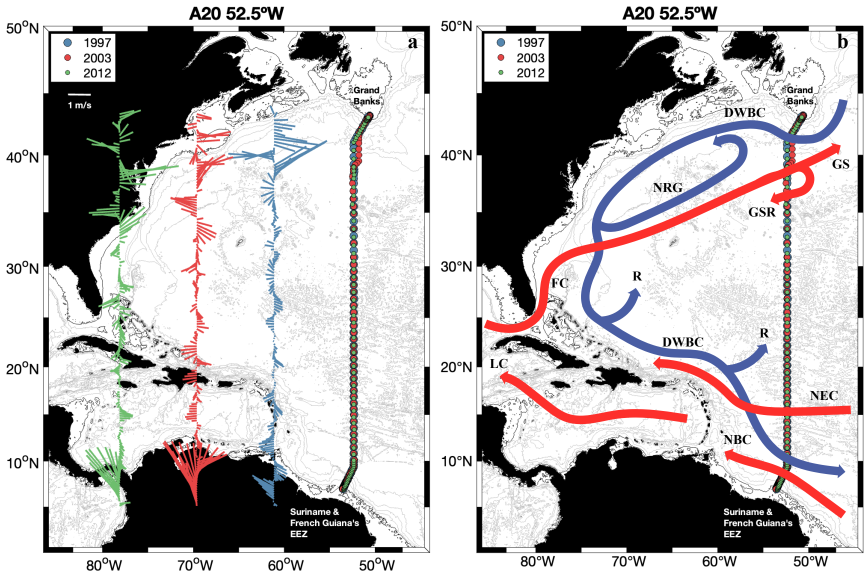

Figure 2.1. a) Station positions carried out repeatedly at 52ºW (A20) in 1997 (blue), 2003 (red) and 2012 (green). Daily mean for the time of the cruise sea surface velocities from the GLORYS model output at 52ºW for 1997, 2003 and 2012 are presented shifted to the west to be better displayed. b) The main currents are represented in dark blue and red arrows for cold and warm currents, respectively. DWBC stands for Deep Western Boundary Current, NRG stands for Northern Recirculation Gyre, GS for Gulf Stream, GSR for Gulf Stream Recirculation, FC for Florida Current, R for Recirculation, LC for Loop Current, NEC for North Equatorial Current, and NBC for North Brazil Current (adapted from Bower et al., 2019).

2.2. Data and Methods

2.2.1 Hydrographic Data

Hydrographic data from 1997, 2003 and 2012 were collected along the A20 section at nominally 52°W in the North Atlantic (Fig. 2.1). The sections were sampled in summer, fall and spring, respectively. The 1997 section was part of WOCE-WHP, while both the 2003 and 2012 sections were part of the successive international CLIVAR. The sampling direction changed between sections, starting in the north, and going south in 1997 and 2003, and *vice versa* in 2012. The northern tip of all transects is the Grand Banks of Newfoundland, while the southern edge is Suriname's Exclusive Economic Zone

(EEZ) for the 1997 and the 2003 occupations, and French Guiana's EEZ for the 2012 transect.

The data were collected using a rosette equipped with Niskin bottles for biogeochemical data, a Lowered Acoustic Doppler Current Profiler (LADCP), a Neil Brown Instrument Systems Mark III (NBIS MK3) Conductivity-Temperature-Depth sensor (CTD) for the 1997 occupation, and a SeaBird 911plus CTD for the other two occupations. In addition, Shipboard ADCP (SADCP) data were collected in each survey. A total of 95, 88 and 83 stations were sampled in 1997, 2003 and 2012, respectively. The 1997 survey lacks LADCP data on stations 1 to 4, 55, 57, 61 and 92 to 95. Likewise, the 2003 survey lacks LADCP data on stations 85 to 88.

Wind data from the National Center for Environmental Prediction Reanalysis II (NCEP-DOE) project from the National Oceanic and Atmospheric Administration (NOAA) are used to estimate Ekman transports for each survey (Kanamitsu et al., 2002). The daily wind data is retrieved from the specific time of each cruise.

A θ-S diagram for the southern part of the A20 section and the vertical distribution of potential temperature (θ) and salinity, together with neutral density (γ^n; Jackett & McDougall, 1997) are shown in Figs. 2.2, 2.3 and 2.4, respectively. These property distributions help to identify the reference level as in Casanova-Masjoan et al. (2018) and in Joyce et al. (2001). This reference level is then used to integrate the thermal wind equation and to calculate the transports between density layers. Moreover, the property characteristics are used also to assess the water mass distribution throughout the years. The water mass distribution in the A20 section (Figs. 2.3 and 2.4, Table 1) varies slightly from that given in Casanova-Masjoan et al. (2018) for the A22 section. The slight variations between the two sections are caused by their geographical location. The A22 section at 66ºW is located west of A20 and it crosses the Antilles and samples part of the Caribbean Sea, A20 samples the western part of the North Atlantic Subtropical Gyre. It also reaches further north than A22, extending all the way to the Grand Banks at 43ºN. These geographical differences lead to the presence of more meridionally extended Antarctic Intermediate Water (AAIW) and Antarctic Bottom Water (AABW) layers in A20 than in A22. AAIW appears as a distinguishable low salinity lobe of water in 250-1250 m depth range in the southern part of the A20 section (Fig. 2.4). AABW is a cool (<2ºC) and low salinity (<34.88) water mass at the bottom of the ocean, below 4500 m depth (Figs. 2.3 and 2.4). Additionally, two freshwater masses appear in the first few meters of the water column both at the northernmost and southernmost tips of A20: Polar Surface Water (PSW) occupying from the surface to 250 m depth at the northern end of the section, and Amazonian runoff waters extending a few meters depth at the southern end only in 2012 (Figs. 2.2, 2.3 and 2.4). All three sections sampled the Subtropical Mode Water (STMW), which is formed by convection in late winter south of the GS (Joyce et al., 2013) with salinities in the range of 36-36.5 (Fig. 2.4). North Atlantic Subtropical UnderWater (STUW) appears as a maximum in salinity (>36.5) in the shallow layers on the southern side of the section, from 5°N to 15°N (Fig. 2.4). It is formed as the result of the positive result of evaporation-precipitation in the central tropical Atlantic (Worthington, 1976). Labrador Sea Water (LSW), the upper branch of the North Atlantic Deep Water (NADW), flows southward from the Labrador Sea into the study region. On A20, it is sampled at latitudes >40°N and nominally at 750-1000 m depth (Figs. 2.3 and 2.4). Iceland-Scotland Overflow Water (ISOW) and Denmark Strait Overflow Water (DSOW), the lower branches of the NADW, can be found below LSW at 2500-4500 m depth. These three water masses form the NADW carried southward by the DWBC that flows to the South Atlantic Ocean after two crossings of the A20 section.

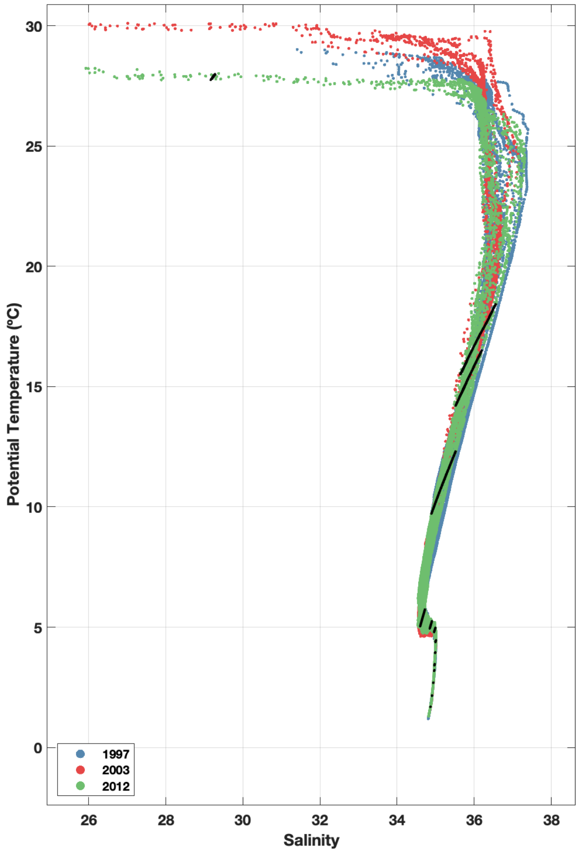

Figure 2.2. θ-S diagram of stations 60-90 (1997 and 2003) and 1-30 (2012) of the A20 hydrographic section at 52ºW in the Atlantic Ocean. Blue, red and green dots are for 1997, 2003 and 2012, respectively. Black lines are the neutral density layers in which the ocean has been divided.

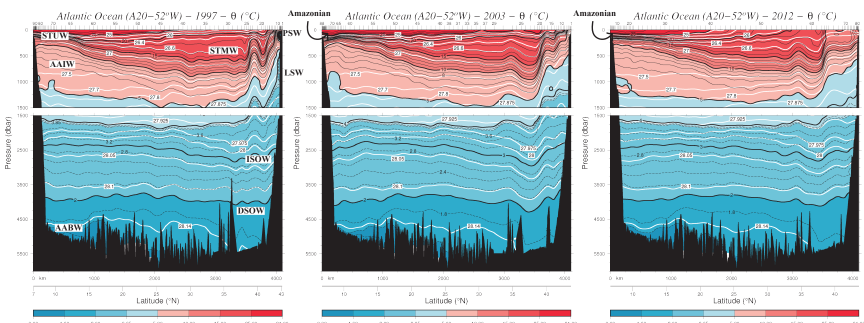

Figure 2.3. Vertical sections of potential temperature (θ, ºC) at 52ºW in the Atlantic Ocean for (a) 1997, (b) 2003 and (c) 2012. Neutral density (γ^n, kg m^{-3}) is overlayed in white lines.

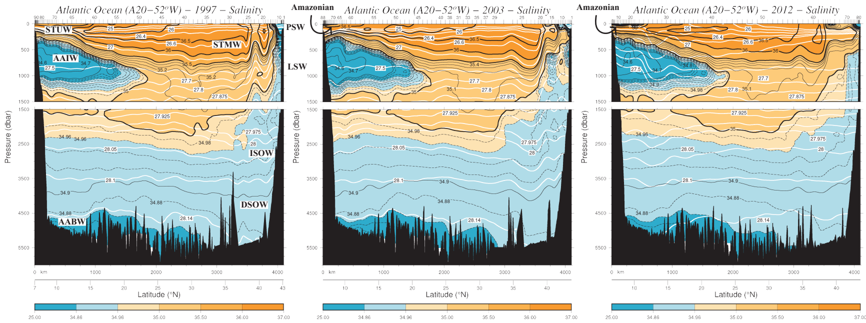

Figure 2.4. Same as Fig. 2.3 but for salinity.

2.2.2 Numerical Ocean Model Data

A free-running model and two data-assimilating models with monthly resolution are compared to the hydrographic observations to assess which provides the best match. This match is based on which one follows closely the mass transports of each current studied in this work. After that, the best one is used to inform a study of the interannual variability existing between the cruises. The model products were obtained at 52ºW, for latitudes between 5º and 50ºN, and for the full water column.

The 6th version of the Modular Ocean Model (MOM6) produced by the Geophysical Fluid Dynamics Laboratory (Adcroft et al., 2019) is a free running model. It has a nominal 1/4° horizontal resolution and 50 vertical levels. It is forced with the JRA55-do atmospheric reanalysis product (Stewart et al., 2020; Tsujino et al., 2020), yielding monthly averaged products for the years 1958-2018.

The "Estimating the Circulation and Climate of the Ocean Version 4 Release 4" (ECCOV4r4) model is a data-assimilating model produced by the Jet Propulsion Laboratory. Its vertical gridding varies from 10 m to 457 m from the surface to the bottom. Its spatial horizontal resolution is 1/2º over the entire globe, whereas the temporal resolution used for this work is one month (Forget et al., 2015; Fukumori et al., 2021).

The "Global Ocean Physics Reanalysis" (GLORYS) model is a global ocean reanalysis and data-assimilating model produced by the Copernicus Marine Environment Monitoring Service. It describes ocean circulation at eddy-resolving resolution with a spatial resolution of 1/12° and a temporal resolution of one month, and the depth is gridded in 50 standard levels (Lellouche et al., 2018).

Table 2.1. Neutral density layers and water masses. Level of no motion indicated in bold.

Layer	Neutral density (γ^n) range	Water Mass
1	Surf.-26.4	STUW
2	26.4-26.6	STMW
3	26.6-27	AAIW
4	27-27.5	AAIW
5	27.5-27.7	AAIW
6	27.7-27.8	AAIW
7	27.8-27.875	LSW
8	27.875-27.925	LSW
9	27.925-27.975	LSW
10	27.975-28	ISOW
11	28-28.05	ISOW
12	28.05-28.1	DSOW
13	28.1-**28.14**	DSOW
14	**28.14**-bot.	AABW

2.2.3 Geostrophic Transport and Inverse Model

The initial geostrophic velocity is computed for each station pair using the thermal wind equation. Following Casanova-Masjoan et al. (2018) and Joyce et al. (2001), the neutral density layer of γ^n =28.14 kg m^{-3} has been used as the reference layer to calculate the geostrophic velocity. This layer lies between the eastward flowing NADW and the westward flowing AABW in section A20. When the seafloor is shallower than this layer, the closest common depth layer existing on the station pair is used as the reference level.

Additionally, the relative geostrophic velocity is adjusted to ADCP measurements following Comas-Rodríguez et al. (2010): the vertical profiles of the SADCP, LADCP and geostrophic velocities are visually compared at each station pair (Fig. 2.5). Then, an adjustment is made by selecting a depth interval where any of the ADCP velocities match the geostrophic velocity. When both SADCP and LADCP velocity profiles match with the geostrophic velocity, the SADCP profile is selected for the adjustment. The SADCP vertical shear used for the comparison has been computed as suggested by E. Firing (personal communication): a range of 2 nautical miles from the CTD location is established for each CTD/LADCP station sampled. SADCP data sampled within this range is averaged and associated to that station. Velocities between two stations are averaged separately from the on-station velocity. Then, the SADCP velocity used for the comparison is computed as the average velocity between station n^{th}, station $n^{th}+1$ and the value between those two stations. This final value is taken as the best approximation of the SADCP vertical shear between station pairs. Fig. 2.5 shows several adjustments for 1997, 2003, and 2012 at the GS location. However, not every station pair has undergone the adjustment due to lack of a similarity pattern between the S/LADCP and the geostrophic velocity profiles. The ADCP uses the particles in the water column to measure the shear, hence when the water column is low backscattered (low particle concentration), the ADCP might not resolve the velocity shear appropriately.

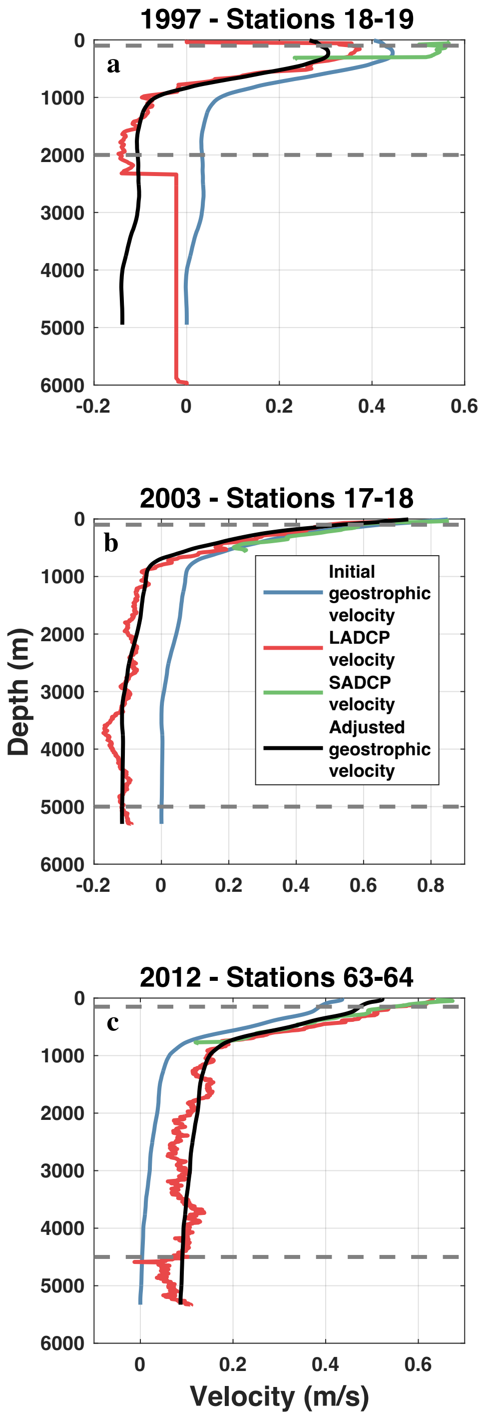

Figure 2.5. Examples of comparison between the initial geostrophic velocity profile (blue line), the LADCP (red line) and SADCP (green

line) velocities normal to station pairs and the geostrophic velocity profile adjusted to ADCP data (black line) for (a) 1997, (b) 2003 and (c) 2012. Gray dashed lines indicate the depth range where the adjustment is made. Axes range vary between figures.

The water column is divided into 14 neutral density layers (Table 2.1). Casanova-Masjoan et al. (2018), Hall (2004) and Joyce et al. (2001) used 17 layers, however the outcropping of several isopycnals in 2012 (Fig. 2.3c) forms a set of large artificial eddies when the inverse model is applied. Therefore, we combined several shallower layers including the outcropped layers to avoid this issue. The deeper layers are the same as those used in the above-mentioned studies (Table 2.1). The initial net mass imbalances, computed as the net transport across each section, are -7.4 Sv, 57.0 Sv and 0.4 Sv for 1997, 2003 and 2012, respectively. After the ADCP adjustments, the net mass imbalances increase to -8.2 Sv, 62.8 Sv and -10.4 Sv, respectively (Fig. 2.6). The ADCP-adjusted overall distribution (red) presents some minor changes over the original distribution (blue). For 1997, the thermocline and intermediate transports (γ^n =26.4 kg m^{-3} to γ^n =27.5 kg m^{-3}) decrease to almost zero, and the mass transport over the deep layers (γ^n=28.1 kg m^{-3} to γ^n =28.14 kg m^{-3}) significantly increases. For 2003, the intermediate transport (γ^n=27.0 kg m^{-3} to γ^n =27.5 kg m^{-3}) decreases while the deep transport (γ^n =28.1 kg m^{-3} to γ^n =28.14 kg m^{-3}) increases. The vertical distribution does not change in 2012 except in the deep and bottom layers (γ^n =28 kg m^{-3} to the bottom), where the slightly eastward transport changes to westward transport.

After the use of ADCP data to estimate the new mass transport, an inverse model is applied to adjust the imbalance of the mass transport (Wunsch, 1996). The inverse model uses a set of constraints and uncertainties, with mass conservation being the most important constraint (Wunsch, 1996; Wunsch, 1978). The inverse model follows previous studies in the region (Casanova-Masjoan et al., 2018; Hall et al., 2004; Joyce et al., 2001) but with two major differences: the original 17 neutral density layers has been reduced to 14 layers, as explained before, and the total silica conservation has not been included in the inverse model. Silica conservation has been achieved when imposing mass conservation (34.9±150.2 Kmol/s, 15.1±177.1 Kmol/s and 39.2±142.6 Kmol/s for 1997, 2003 and 2012, respectively). Therefore, the silica conservation equations do not introduce independent equations.

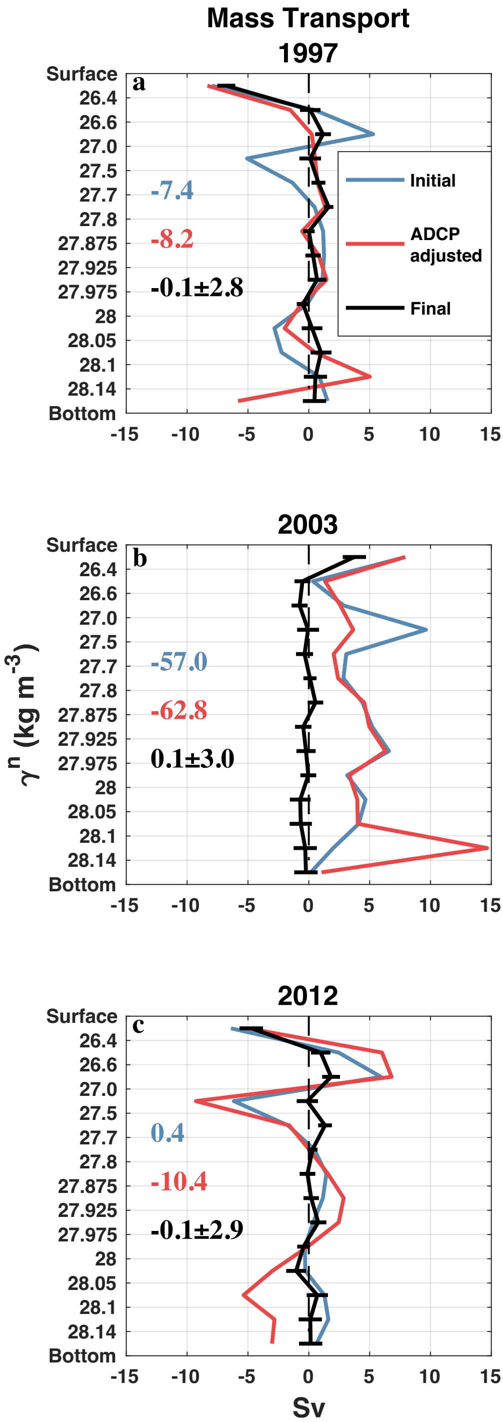

Figure 2.6. Meridionally integrated mass transport (Sv) across the A20 section for (a) 1997, (b) 2003 and (c) 2012. Blue lines are the

initial (unbalanced) mass transports, red lines are the ADCP (unbalanced) adjusted mass transports and black lines are the inverse model solution's derived mass transports. Total mass transports are shown in their respective colors.

The inverse problem is formulated as follows:

$$Ab + n = -Y$$

where A is an $M \times N_T$ matrix, N_T is the number of unknowns and M is the number of transport constraints. b is a column vector of length N_T ($N_T = N + 1$) containing the unknown geostrophic reference velocities for each of the N^{th} station pairs, plus the adjustment to the Ekman transport. n is a column vector of length M of the noise of each constraint. Y is a column vector of length M representing the mass transport initially unbalanced in each layer.

The inverse problem is solved through the Gauss-Markov method (Wunsch, 1996), which provides a solution for the initial estimates with minimum error variances. This method requires a priori variances for the velocities and the constraints. Following Joyce et al. (2001), the chosen velocity variances are $(0.05 \text{ m s}^{-1})^2$ for the ADCP-adjusted velocities and $(0.1 \text{ m s}^{-1})^2$ for the non-ADCP-adjusted velocities. The mass variances are $(0.5 \text{ Sv})^2$ for the total mass conservation, $(2 \text{ Sv})^2$ for the shallowest layer and $(1 \text{ Sv})^2$ for the remaining layers.

The inverse model is applied to the water volume enclosed by the American continent coastline and the A20 section to the east. There is not a significant flow through the Panama Canal (Joyce et al., 2001), and, therefore, the water volume is fully enclosed. The sum of the velocities at the reference level (with their error estimates) from the inverse model plus the ADCP velocities are presented in Fig. 2.7 (black). The added ADCP velocities are represented in red. Both velocities show a similar distribution: features like the DWBC and the GS velocities are remarkably different from zero while the ocean interior shows velocities not significantly different from zero. This set of velocities adjusted from the ADCP and from the inverse model are used to calculate the adjusted mass, heat and freshwater transports.

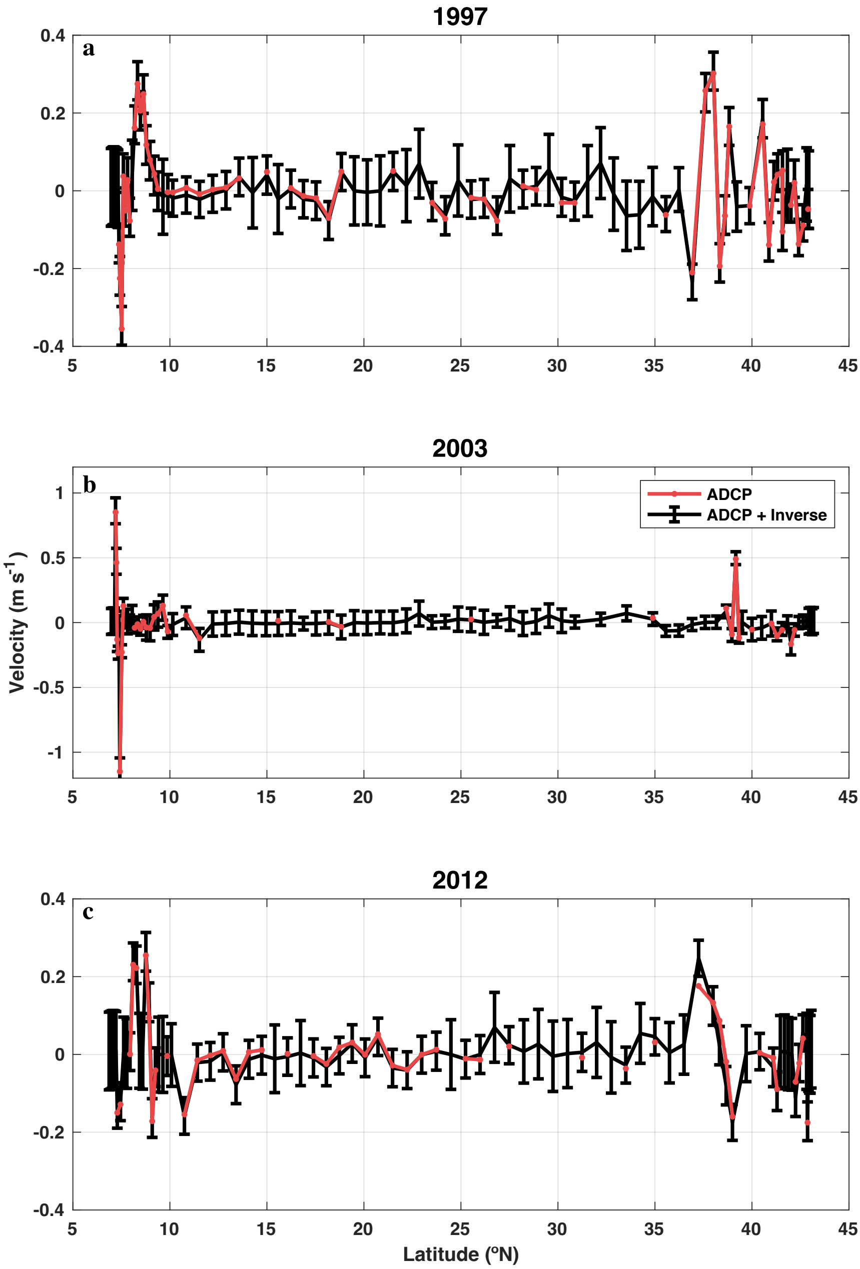

Fig. 2.7. ADCP-adjusted geostrophic velocity (red line) and ADCP-adjusted velocity plus the reference level velocity estimated from the inverse model (black line) versus latitude for (a) 1997, (b) 2003 and (c) 2012. Black error bars correspond to inverse modeling calculations. Gaps in the ADCP-adjusted velocity correspond to station pairs where the initial geostrophic velocity could not be

adjusted to ADCP velocity. The 2003 y-axis has a different range than for 1997 and 2012.

2.3. Results

2.3.1 Adjusted Geostrophic Transport

The zonal mass transport per neutral density layer with its net imbalance is shown in Fig. 2.6. The inverse model has reduced the ADCP-adjusted imbalances to values not significantly different from zero (-0.1±2.8 Sv, 0.1±3.0 Sv and -0.1±2.9 Sv for 1997, 2003 and 2012, respectively). The shallowest layer of the zonal transport presents a westwards imbalance in both 1997 (-6.8±0.7 Sv) and 2012 (-4.7±1.0 Sv), and eastwards in 2003 (3.7±1.0 Sv). The zonal transport distribution through latitudes and density layers provides the variability of mass transport of the main currents of the AMOC (Fig. 2.8). Mass transports were computed by subtracting the mass transport at the current's starting location from that at its ending location. Ocean General Circulation Models (OGCMs) are used to determine the most reliable mass transports compared to hydrographic data (Figs. 2.9, 2.10 and 2.11) and to estimate the time variation of heat and freshwater transports.

The North Brazil Current (NBC) flows between the southernmost station pair and 7.7/7.8ºN in 1997/2003. The northern limit of the current extends to 8.3ºN in 2012 (Figs. 2.1 and 2.8a, b). We have considered the northern limit of the NBC as the starting location of the eastward flow as seen in Fig. 2.1. The NBC extends from the surface to γ^n =27.7 kg m^{-3} (~1100 m depth) in all surveys. The NBC mass transport (Table 2.2) presents a minimum in 1997 (–5.6±0.7 Sv) followed by an intensification in 2003 (-15.8±1.2 Sv) and a non-significant change in 2012 (–15.6±1.6 Sv). The OGCMs outputs resemble the hydrographic NBC differently in each survey. The MOM6 and ECCO outputs only resemble the hydrographic NBC in 1997, where the GLORYS output presents a stronger NBC (Fig. 2.9a). However, the 2003 (Fig. 2.10a) and 2012 (Fig. 2.11a) MOM6 and ECCO outputs do not match the NBC, but the GLORYS output does.

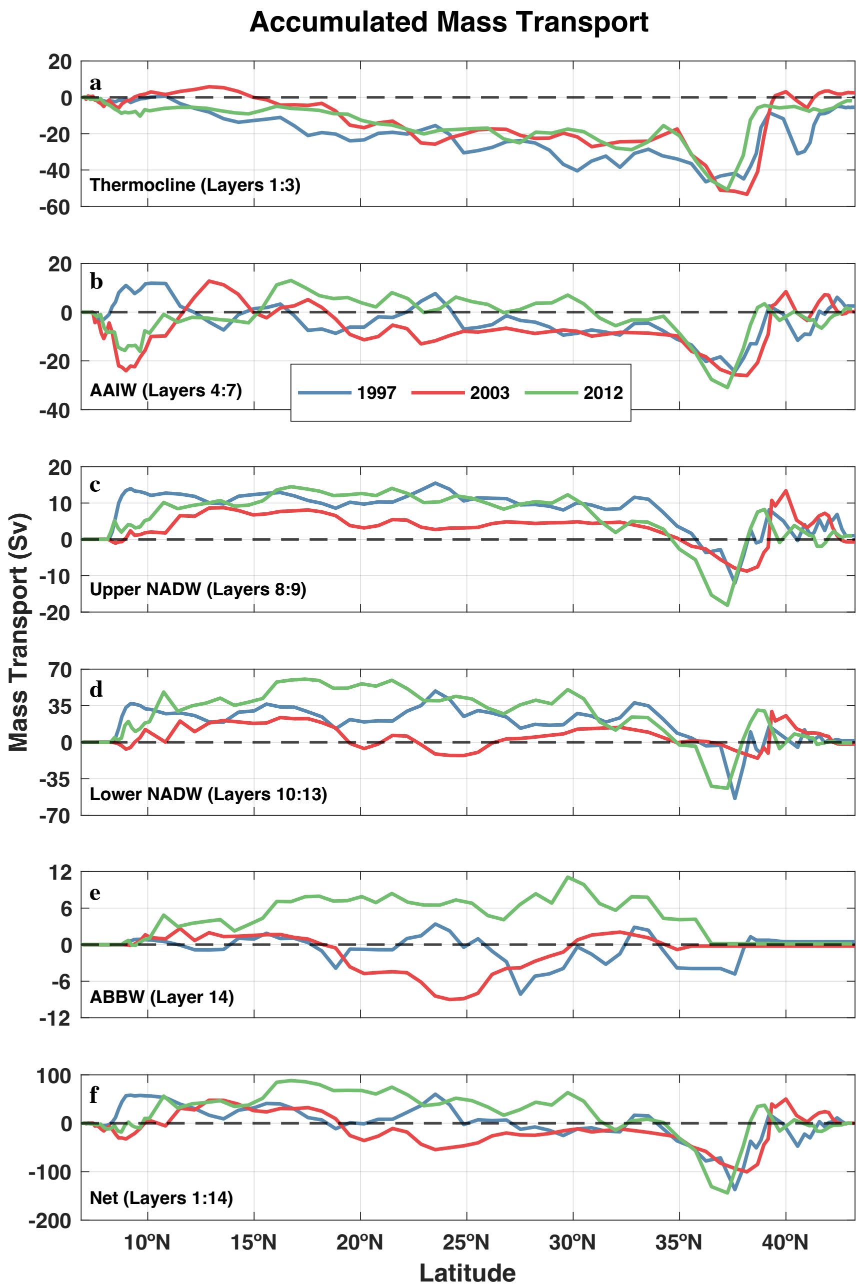

Fig. 2.8. Northward accumulated mass transport (Sv) after the inverse model for 1997 (blue), 2003 (red) and 2012 (green) occupations. (a) Thermocline transport estimated for layers 1 to 3. (b) AAIW transport estimated for layers 4 to 7. (c) Upper NADW transport estimated for layers 8 to 9. (d) Lower NADW transport estimated for layers 10 to

13. (e) AABW transport estimated for layer 14. (f) Net transport estimated for layers 1 to 14. Y-axis range varies between subplots.

North of the NBC, the NEC flows westward between the surface and γ^n =27 kg m^{-3} (~500 m depth). The NECs northern limit is considered at approximately 24.2ºN, 25.5ºN and 25.2ºN for 1997, 2003 and 2012, respectively (Fig. 2.8a). This flow is fed by the southern branches of the Azores Current and the Canary Current (Hernández-Guerra et al., 2002; Stramma, 1984). The northernmost part of this westward flow is called Antilles Current when flowing north of the Puerto Rico Island (Bryden et al., 2005; Hernández-Guerra et al., 2010; Johns et al., 2008). The northern limit of the NEC has been chosen as the latitude where the mass transport of the GSR is not significantly different than zero (–2.0±3.8, 0.1±4.0 and 1.4±4.0 Sv in 1997, 2003 and 2012, respectively). The NEC mass transport weakens between 1997 and 2003 (–28.6±2.5 Sv and –12.3±3.6 Sv, respectively) and stays with a similar mass transport to that of 2003 in 2012 (–10.6±2.8 Sv) (Table 2.2). The NEC estimated from the OGCMs resembles the pattern of the NEC circulation from hydrography, showing stronger mesoscale patterns in the in-situ data (Figs. 2.9a, 2.10a and 2.11a).

The GSR and GS mass transports are computed between the surface and the ocean bottom. The latitudinal ranges of the GSR are 32.9-36.9ºN, 34.9-38.2ºN and 34.2-37.3ºN for 1997, 2003 and 2012, respectively (Fig. 2.8f). Thus, the GSR width (445, 367 and 345 km in 1997, 2003 and 2012, respectively) presents a narrowing between each survey, and its location shifts to the north in 2003 compared to 1997 and 2012. The mass transport of the GSR is –152.1±17.0 Sv, -72.3±17.4 Sv and -145.3±19.8 Sv in 1997, 2003 and 2012, respectively (Table 2.2). The significant weakening in 2003 compared to 1997 and 2012 is also observed in the GS mass transports (155.3±11.1 Sv, 102.7±13.5 Sv and 181.1±14.9 Sv for 1997, 2003 and 2012, respectively). Moreover, the GS also presents a northern shifting in 2003 (38.2-41.0ºN) compared to 1997 (36.9-38.8ºN) and 2012 (37.3-38.9ºN; Fig. 2.8f). However, the GS does not follow the same narrowing present in the GSR because it is wider in 2003 (311 km) than in 1997 (212 km) and 2012 (178 km). The GSR and GS from the OGCMs outputs show lower mass transports than the hydrographic results (Figs. 2.9d, 2.10d, 2.11d). The GSR mass transport from the OGCMs output and from 1997, 2003 and 2012 are 3.6, 13.0, 6.0 Sv (MOM6), 20.6, 12.3, 3.0 Sv (ECCO) and –73.8, -

17.6, -32.2 Sv (GLORYS), respectively. The results for the GS are 0.4, 6.9, -11.4 Sv (MOM6), 28.2, 0.6, 1.4 Sv (ECCO) and 182.3, 24.2, 84.7 Sv (GLORYS), respectively. Only the GLORYS output resembles the pattern of circulation of the GS system (Fig. 2.9d).

The DWBC flows at deep layers (γ^n =27.875 kg m^{-3} to γ^n =28.14 kg m^{-3}) and crosses the northern/southern boundaries at the latitudinal ranges of 39.2-42.8/8.1-13.6ºN, 41.0-42.8/8.2-14.1ºN and 38.9-42.8/8.1-14.1ºN for 1997, 2003 and 2012, respectively (Fig. 2.8c, d). In the northern crossing, the DWBC presents a narrowing in 2003 (200 km) compared to 1997 (401 km) and 2012 (434 km). In the southern crossing, the DWBC exhibits a widening from 1997 (612 km) to 2003 (657 km) which maintains to 2012 (668 km). The estimations of the DWBC mass transports at the northern/southern crossing are -21.2±8.9/29.0±9.1, -14.4±10.8/14.2±8.1 and -37.9±10.2/44.5±9.8 Sv for 1997, 2003 and 2012, respectively (Table 2.2). The northern-crossing DWBC from hydrography is only well represented by the GLORYS output with mass transports of –39.5 (1997), -5.8 (2003) and –33.8 (2012) Sv (Figs. 2.9b, 2.10b, 2.11b). All three OGCM outputs present a weaker southern-crossing DWBC (Figs. 2.9b, 2.10b, 2.11b) than the obtained from hydrography, except the GLORYS output in 1997 (Fig. 2.9b).

The bottom transport of the AABW is computed between the neutral density layer (γ^n =28.14 kg m^{-3}, ~4750 m depth) and the bottom of the ocean (~5500 m depth). Its southern edge is in all cases 7.0ºN, but its northern edge shifts to the south between 1997 (27.5ºN) and 2003 (24.2ºN) (Fig. 2.8e). It flows westwards with a mass transport of -8.1±7.0 Sv and –9.0±7.9 Sv in 1997 and 2003, respectively. Layers 13 (γ^n =28.1 kg m^{-3}) and 14 (γ^n =28.14 kg m^{-3}) appear to be coupled in 2012 as they present a similar pattern. Therefore, there is not a mean westward flow in layer 14 (Fig. 2.8e) to define and estimate the mass transport of AABW crossing the 2012 hydrographic section. The OGCM outputs present a very weak transport, almost nonexistent, of the AABW (Figs. 2.9c, 2.10c, 2.11c).

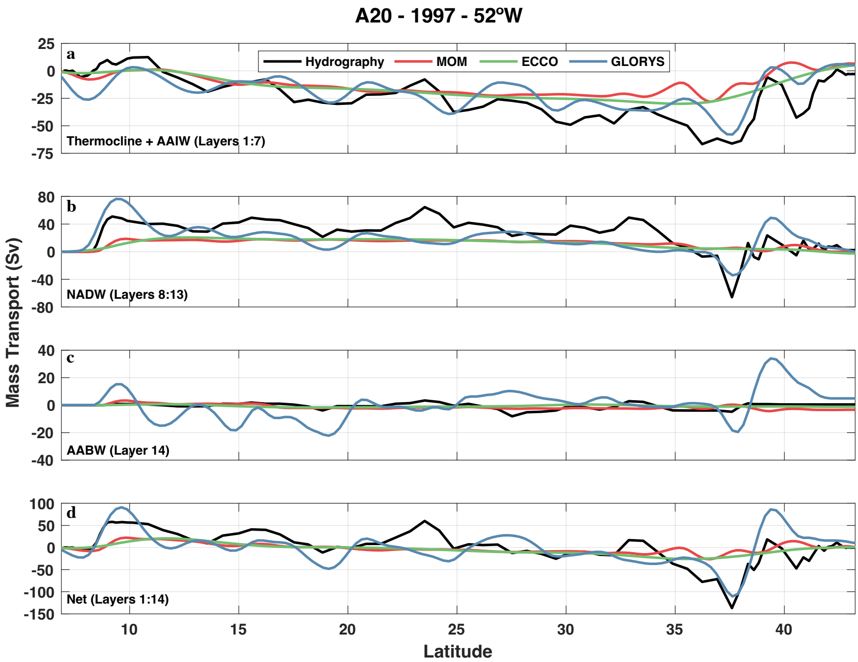

Fig. 2.9. Northward accumulated mass transport (Sv) after the inverse model (black), from the MOM6 model (red), from the ECCO model (green) and from the GLORYS model (blue) for 1997. (a) Thermocline and AAIW transport estimated for layers 1 to 7. (b) NADW transport estimated for layers 8 to 13. (c) ABBW transport estimated for layer 14. (d) Net transport estimated for layers 1 to 14. Y-axis range varies between subplots.

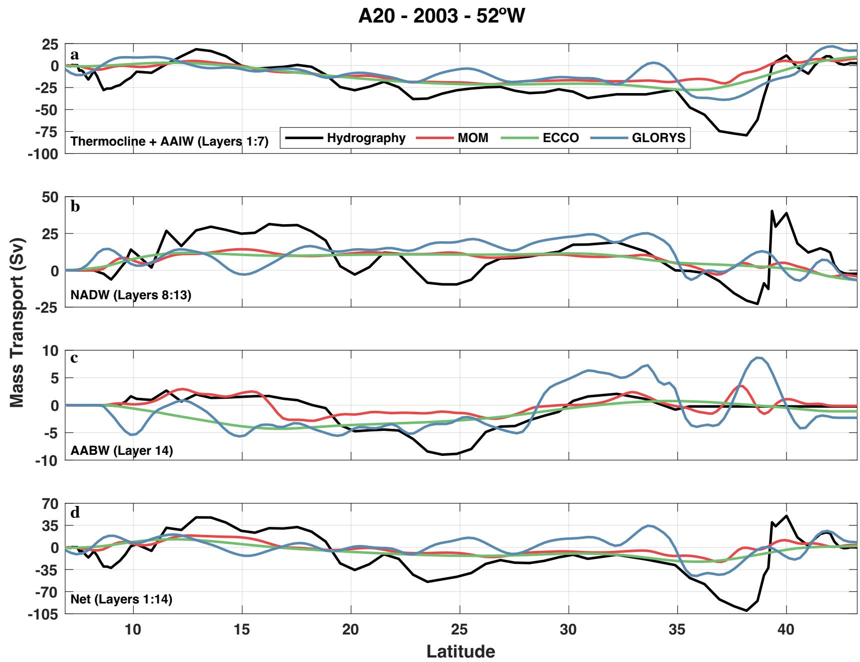

Figure 2.10. Same as Fig. 2.9 but for 2003.

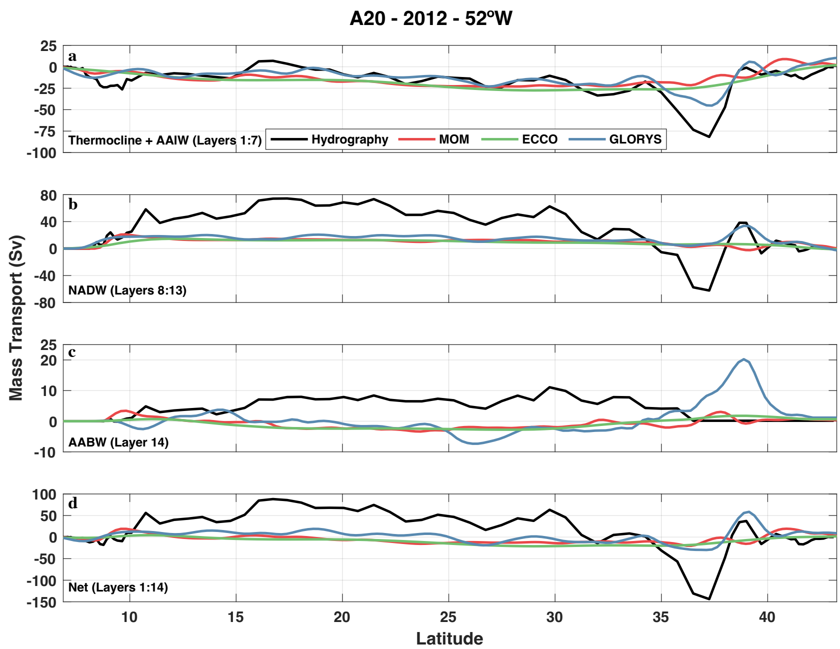

Figure 2.11. Same as Fig. 2.9 but for 2012.

2.3.2 Heat and Freshwater Transports

The heat transport across our section is estimated from the inverse box model results:

$$\overline{H} = \sum_{i}\sum_{j} C_{p_{ij}} pt_{ij}\rho_{ij}y_{ij}z_{ij}u_{ij}$$

where H is the net heat transport across the A20 section, Cp_{ij} is the specific heat capacity in layer i at station pair j, pt_{ij} is the potential temperature, r_{ij} is the density, y_{ij} is the distance between adjacent stations, z_{ij} is the vertical distance between adjacent layers and u_{ij} is the perpendicular velocity to the A20 section from the inverse model. In 1997 and 2012, the heat flux is to the west and with similar transports (-0.7±0.1 PW and -0.6±0.1 PW, respectively; 1 PW = 10^{15} W). This results in a heat transport from the ocean to the atmosphere. In contrast, 2003 presents a non-significant heat transport (0.1±0.1 PW). Figure 2.12a, b, c presents the heat transport from OGCM outputs together with the heat transport estimated in each survey.

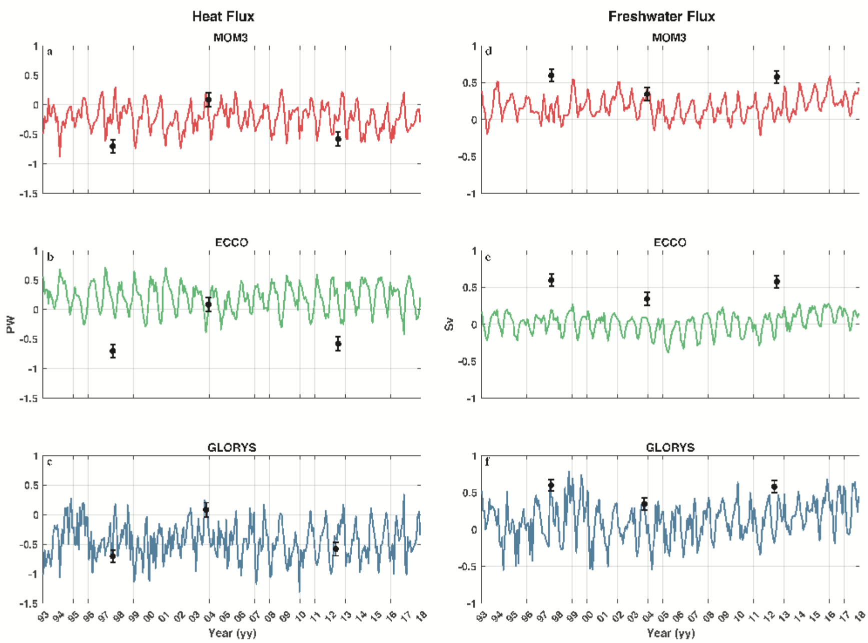

Figure 2.12. Time series of heat (PW) and freshwater (Sv) fluxes between 1993 and 2018 estimated from the MOM6 (a, d, red line), ECCO (b, e, green line) and GLORYS (c, f, blue line) model. Black dots with error bars represent the values estimated from the inverse

model in the month-year when the hydrographic section was carried out.

Heat transports estimated by MOM6 and ECCO are higher than those estimated from the hydrographic cruises in 1997 and 2012 (Fig. 2.12a, b). The 2003 heat flux of the survey is the only result that lies within the MOM6 and ECCO ranges. On the other hand, heat transports estimated from GLORYS roughly match the heat transport estimated from hydrography, being -0.6 PW, 0.2 PW and -0.4 PW in 1997, 2003 and 2012, respectively (Fig. 2.12c and Table 2.3).

The monthly mean heat flux and standard deviation is computed from the GLORYS time series (Fig. 2.13a). The monthly mean heat flux is always negative providing heat from the ocean to the atmosphere. Additionally, a Mann-Kendall Tau test is applied to the GLORYS output to assess the trend over the 1993-2020 period (Fig. 2.13b). The result of this test shows that the heat flux presents a trend of -2.6×10^{-2} PW per decade over the period with a confidence level of 72.1%. However, the heat flux does not show a significant trend when the confidence level is 95%.

The understanding of the global water cycle and the climate variability can be improved by the knowledge obtained in enclosed oceanographic sections. Specifically, the freshwater flux shows the air-sea interactions of the waters enclosed by an oceanographic section. In this work, the freshwater fluxes of the three surveys are estimated as in Joyce et al. (2001):

$$\bar{F} = -\sum_i \sum_j T_{ij} S'_{ij} / S_0$$

where F is the excess of precipitation plus runoff over evaporation in the closed volume, T_{ij} is the mass transport in layer i at station pair j, from the inverse model, S_0 is the mean salinity of the section and $S'_{ij}=S_{ij}-S_0$.

The resulting freshwater fluxes (0.6±0.1, 0.3±0.1 and 0.6±0.1 Sv in 1997, 2003 and 2012, respectively) may be coupled with the heat fluxes, as they weaken and strengthen in the same surveys. The results provide that the precipitation and river runoff are higher than the evaporation for these surveys. As in heat flux, the freshwater flux from MOM6 and ECCO at the time of the cruises are different than those from the cruises (Fig. 2.12d, e). As in heat flux, the GLORYS output coincides with the freshwater flux from hydrography in 1997

(0.5 Sv) and 2003 (0.3 Sv) although it is significantly different in 2012 (-0.1 Sv) (Table 2.3; Fig. 2.12f).

Table 2.2. Mass transports, latitude range and layers of the main currents of the A20 section in 1997, 2003 and 2012.

	Layers	Latitude Range (ºN)			Transports (Sv)		
		1997	2003	2012	1997	2003	2012
GS	1:14	36.9-38.8	38.2-41.0	37.3-38.9	155.3±11.1	102.7±13.5	181.1±14.9
GSR	1:14	32.9-36.9	34.9-38.2	34.2-37.3	-152.1±17.0	-72.3±17.4	-145.3±19.8
NBC	1:5	7.0-7.7	7.0-7.8	6.9-8.3	-5.6±0.7	-15.8±1.2	-15.6±1.6
NEC	1:3	7.7-24.2	7.8-25.5	8.3-25.2	-28.6±2.5	-12.3±3.6	-10.6±2.8
Upper North DWBC	8:9	39.2-42.8	41.0-42.8	38.9-42.8	-7.2±3.1	-3.9±4.3	-7.3±3.5
Lower North DWBC	10:13	39.2-42.8	41.0-42.8	38.9-42.8	-14.0±8.4	-10.5±9.9	-30.6±9.6
Net North DWBC	8:13	39.2-42.8	41.0-42.8	38.9-42.8	-21.2±8.9	-14.4±10.8	-37.9±10.2
Upper South DWBC	8:9	8.1-13.6	8.2-14.1	8.1-14.1	9.8±2.0	1.9±2.1	9.2±2.2
Lower South DWBC	10:13	8.1-13.6	8.2-14.1	8.1-14.1	19.3±8.9	12.2±7.8	35.3±9.6
Net South DWBC	8:13	8.1-13.6	8.2-14.1	8.1-14.1	29.0±9.1	14.2±8.1	44.5±9.8
Net	1:14	6.9-43.3	6.9-43.3	6.9-43.1	-0.1±2.8	0.1±3.0	-0.1±2.9

The monthly mean freshwater transport and its trend in the time series has been estimated from GLORYS following the same procedure used for the heat flux (Fig. 2.13c. d). The freshwater flux from the

GLORYS output presents positive values except in spring, which means that overall, there is more precipitation and runoff than there is evaporation in the closed volume except in spring, when it reverses. A Mann-Kendall test applied to the freshwater flux estimated by the GLORYS output (Fig. 2.13d) provides a trend of 8.1x10^{-2} Sv per decade over that period with a confidence level of 99.9%, which is a more reliable result than the heat flux result. These results document an increase of precipitation in the area bounded by the section A20 at 52ºW and the North, Central and South American continents from 1993 to 2020.

Table 2.3. Heat and freshwater fluxes from inverse calculations and from MOM6, ECCO and GLORYS model for A20 in 1997, 2003 and 2012.

	Heat (PW)			Freshwater (Sv)		
	1997	2003	2012	1997	2003	2012
Hydrography	-0.7	0.1	-0.6	0.6	0.3	0.6
MOM	-0.2	0.0	-0.2	0.2	0.3	0.0
ECCO	-0.1	0.1	-0.2	0.2	0.1	-0.2
GLORYS	-0.6	0.2	-0.4	0.5	0.3	-0.1

2.4. Discussion

The main currents and the heat and freshwater fluxes across the A20 section (52ºW) in 1997, 2003 and 2012 have been investigated. In addition, the OGCMs outputs have been compared to the hydrographic results to find which one presents a better match and to estimate the seasonal and interannual variability of the heat and freshwater fluxes.

At the southernmost part of the A20 section, the NBC presents a high variability between summer (1997, –5.6±0.7 Sv) and fall/spring (2003/2012, -15.8±1.2 Sv/-15.6±1.6 Sv). All three results are within the mass transport range -10 to -30 Sv estimated by Garzoli et al. (2004) from continuous measurements between 2-3ºN and 47.4-

47.1ºN. The NEC mass transport presents an opposite behavior compared to the NBC mass transport. The NEC is stronger in summer (1997, –28.6±2.5 Sv) than in fall (2003, –12.3±3.6 Sv) and in spring (2012, –10.6±2.8 Sv). Using the Sverdrup relation, Hellerman (1980) estimated a NEC mass transport of -9 Sv in fall and -23 Sv in spring. The lack of an error estimate and the fact that these results were obtained at 38ºW may explain the difference in the results.

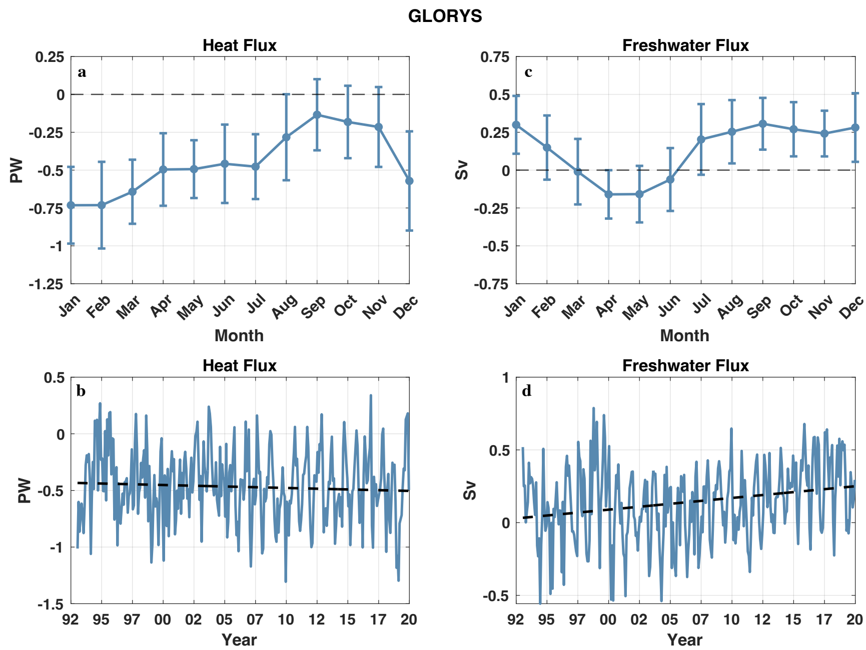

Figure 2.13. Monthly mean and time series of heat (a, b; PW) and freshwater (c, d; Sv) fluxes estimated from the GLORYS model. Black thick dashed lines in (b) and (d) indicate the trend of the time series.

The GS system (GSR/GS) presents an oscillatory behavior of weakening and strengthening of its mass transports between the pair of surveys 1997-2003 (summer: –152.1±17.0 / 155.3±11.1 Sv; fall: -72.3±17.4 / 102.7±13.5 Sv) and 2003-2012 (spring, -145.3±19.8 / 181.1±14.9 Sv). In addition, the GS system is in its northernmost position in fall (2003, 38.2-41.0ºN) compared to summer (1997, 36.9-38.8ºN) and spring (2012, 37.3-38.9ºN), which coincides with the results of Lee & Cornillon (1995), Rayner et al. (2011), Sato & Rossby (1995), Tracey & Watts (1986) and Pérez-Hernández and Joyce (2014).

The mass transport of the northern/southern-crossing DWBC does not significatively change between summer (1997, -21.2±8.9 / 29.0±9.1 Sv) and fall (2003, -14.4±10.8 / 14.2±8.1 Sv). However, the mass transport of the DWBC is stronger in spring (2012, -37.9±10.2 / 44.5±9.8 Sv). Comparing these results with those from Toole et al. (2011) and Toole et al. (2017) at Line W, all of them are within their mass transport range of -79.9 Sv to -3.5 Sv obtained with data ranging 2004-2014. As Le Bras et al. (2019) suggests, the NASG may respond to forcing through fast barotropic adjustments. Furthermore, Meinen & Garzoli (2014) found that the temporal variability of the DWBC at 26.5ºN and 75ºW is caused by Baroclinic Rossby Waves. The dominant period of these events is 70-90 days. Nevertheless, mass transport variations are observed in both larger and shorter time periods (Meinen & Garzoli, 2014).

The comparison of the mass transport from OGCM outputs with the mass transport from hydrographic data reveals that only the GLORYS model resembles the main currents studied in this work. In addition, the mass transport from MOM6 and ECCO numerical models present different estimations than the results obtained from the hydrography. This result may be caused by how each OGCM has been developed. The MOM6 model is a free-running model with no assimilation of data. GLORYS is a reanalysis model with assimilation of data and, in contrast, ECCO only assimilates data. Moreover, different parametrizations of physical processes, rates of mixing and the finer spatial resolution of the GLORYS (1/12 degree compared to ½ degree for ECCO and ¼ degree for MOM6) are responsible of the best fit to the observations. Finally, the atmospheric forcing applied to each model differs substantially: MOM6 is forced with the JRA55-do reanalysis product (6 hourly fields aggregated to monthly averages for 1958–2018; Stewart et al., 2020; Tsujino et al., 2020), ECCO v4 uses the same JRA55-do forcing but applies adjoint-based bias corrections within its assimilation framework (Fukumori et al., 2021), and GLORYS2V3 relies on ERA-Interim surface fields (3 hourly wind stress and daily bulk fluxes computed with CNRM bulk formulae; Lellouche et al., 2018). Variations in forcing origin, temporal resolution, and bias-correction methodology introduce further differences in simulated currents and mass transports, helping to explain the disparities with the hydrographic estimates.

The 1997 and 2012 heat fluxes are a net exchange from the ocean to the atmosphere (-0.7±0.1 PW and -0.6±0.1 PW, respectively). In contrast, the 2003 heat flux presents a non-significant transport (0.1±0.1 PW). These results agree with the variability shown in the GLORYS heat flux. The monthly mean heat flux is always negative. This implies that the basin enclosed by the A20 section exports heat from the ocean to the atmosphere year-round. Moreover, the negative trend of -2.6×10^{-2} PW per decade shown in GLORYS implies that the basin will export heat to the atmosphere in a greater amount each decade.

The freshwater fluxes from hydrography (0.6±0.1, 0.3±0.1 and 0.6±0.1 Sv in 1997, 2003 and 2012, respectively) show that the precipitation and river runoff is higher than the evaporation. When analyzed by monthly means with the GLORYS output, only the spring season shows an evaporation higher than precipitation and runoff. Moreover, the positive trend of 8.1×10^{-2} Sv per decade of the freshwater flux implies that the precipitation and runoff has increased over the evaporation over the decades.

Chapter 3: Zonal Currents in the Western North Atlantic Gyre (2021): Single- vs. Three-Box Models

This chapter has been published as:

Santana-Toscano, D., Pérez-Hernández, M. D., Arumí-Planas, C., & Hernández-Guerra, A. (2025). Estimating the western North Atlantic Subtropical Gyre zonal currents in 2021 through single- and three-box inverse models. Progress in Oceanography, 103415. https://doi.org/10.1016/J.POCEAN.2025.103415

3.1. Introduction

The Atlantic Meridional Overturning Circulation (AMOC) plays a key role in the global climate system since it makes the largest oceanic contribution to the meridional transport of heat (Ganachaud, 2003). It is generally thought that its weakening/strengthening would lead to the cooling/warming of the northern Atlantic (Rayner et al., 2011). The AMOC consists of two limbs. The upper warm limb, mainly represented by the Gulf Stream (GS), carries warm upper waters northward through the North Atlantic Ocean (Bower et al., 2019; Pérez-Hernández and Joyce, 2014). This upper limb gives up heat to the atmosphere in its path to the subpolar regions, where it becomes cold and salty enough to sink to deep layers. This process forms the cold deep limb that returns southward through the Atlantic Ocean in, mainly, the Deep Western Boundary Current (DWBC; Caínzos et al., 2023; Ganachaud, 2003). Once past the Grand Banks (46ºN, 51.3ºW), the DWBC continues along the western boundary relatively undisturbed until Cape Hatteras (35.2ºN, 75.5ºW), where the upper portion of the DWBC is redirected offshore and becomes part of the deep GS (Biló & Johns, 2019; Bower et al., 2009; Bower & Hunt, 2000; Chomiak et al., 2023; Chomiak et al., 2022; Fischer & Schott, 2002; Gary et al., 2011; Van Sebille et al., 2011; Spall, 1996). South of the crossover region, part of the DWBC detaches at the Blake Spur (30°N; Bower and Hunt, 2000). Transport at 26.5°N offshore of Abaco was approximately 30 Sv (1 Sv = 10^6 m^3/s ~10^9 kg/s; Biló and Johns, 2019).

Both current systems are components of the western boundary of the North Atlantic Subtropical Gyre (NASG), which is also mainly composed of the North Brazil Current (NBC), the North Equatorial Current (NEC), and the Antilles Current (Casanova-Masjoan et al., 2020; Pérez-Hernández et al., 2019; Santana-Toscano et al., 2023). The A20 and A22 meridional sections are precisely located in this region and are therefore convenient for quantifying these currents (Fig. 3.1).

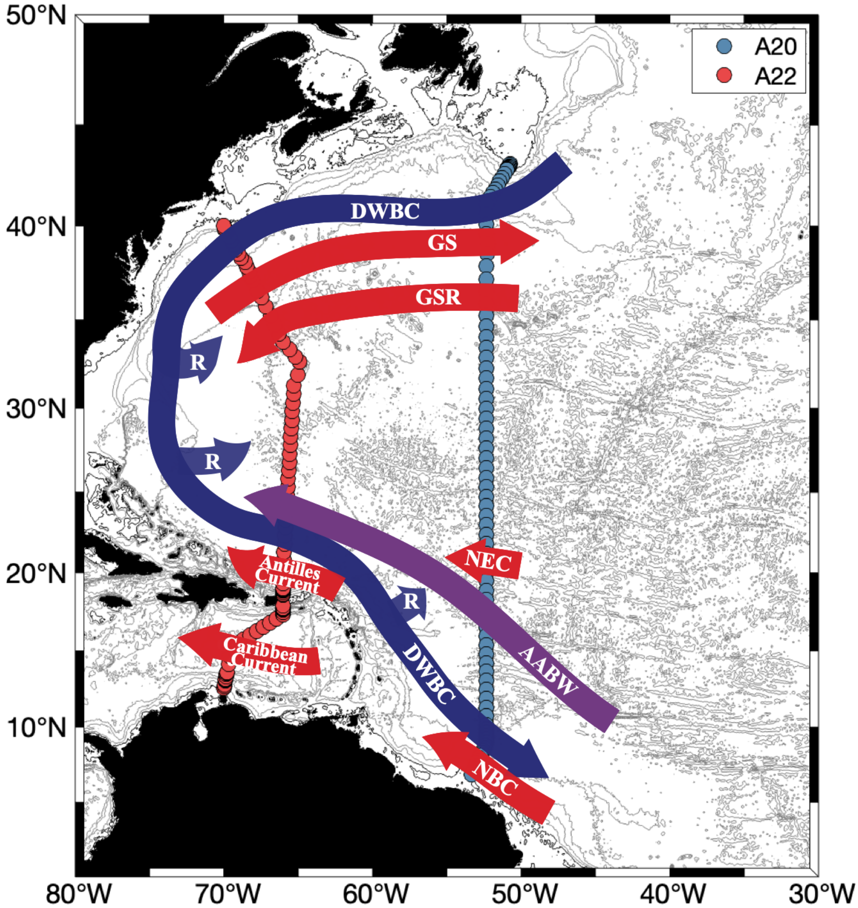

Figure 3.1. Map of the hydrographic sections that form the boundaries of the inverse box model. Red dots are the stations sampled during the spring-2021 occupation of the A22 (66ºW) section. Blue dots are the stations sampled during the spring-2021 occupation of the A20 (52ºW) section. The main currents are represented in red (warm/superficial), dark blue (cool/deep) and purple (bottom) arrows. DWBC stands for Deep Western Boundary Current, GS for Gulf Stream, GSR for Gulf Stream Recirculation, NEC for North Equatorial Current, AABW for Antarctic Bottom Water, NBC for North Brazil Current and R for Recirculation.

The A20 and A22 are hydrographic sections situated at 52ºW and 66ºW, respectively. They were first surveyed in the summer of 1997 as part of the World Ocean Circulation Experiment Hydrographic Program (WOCE-WHP), which aimed to assess the global ocean circulation state in the 1990s. This program served as the foundation for subsequent initiatives such as the Climate Variability Hydrographic Program (CLIVAR) and the Global Ocean Ship-based Hydrographic Investigations Program (GO-SHIP). These programs were created to provide decade-scale resolution for key WOCE-WHP legs. The A20 and A22 sections were reoccupied twice during the CLIVAR era, once in each subsequent decade (fall 2003 and spring 2012). The most recent reoccupation of both sections occurred in spring 2021 as part of the GO-SHIP program (Fig. 3.1). The A20 and A22 sections were sampled consecutively for each of the reoccupations (1997, 2003, 2012, and 2021) as shown in Table 3.1. Both hydrographic sections sample the western NASG, including the GS and the DWBC. Additionally, the A22 section is the only GO-SHIP transect that samples the Caribbean Sea and the Antilles Current (Casanova-Masjoan et al., 2018).

The 1997 A20 leg was first studied by Hall (2004) with a one-box inverse model. Mass transport values were estimated for the main currents of the western NASG, such as the GS (168.7 Sv, positive/negative values will stand for eastward/westward transport) and the northern and southern crossings of the DWBC (-29.5 Sv and 64.1 Sv, respectively). Data from the three decades (1997, 2003, and 2012) of the A20 leg were studied later by Santana-Toscano et al. (2023) with the same inverse model. The mass transports of the GS (155.3±11.1 Sv, 102.7±13.5 Sv and 181.1±14.9 Sv, respectively), the northern/southern crossings of the DWBC (-21.2±8.9 / 29.0±9.1 Sv, -14.4±10.8 / 14.2±8.1 Sv and -37.9±10.2 / 44.5±9.8 Sv), the NBC (-5.6±0.7 Sv, -15.8±1.2 Sv and -15.6±1.6 Sv, respectively) and the NEC (-28.6±2.5 Sv, -12.3±3.6 Sv and -10.6±2.8 Sv, respectively) were estimated. The differences between the 1997 southern crossing of the DWBC of Hall (2004) and Santana-Toscano et al. (2023) are related to the meridional extension considered. Santana-Toscano et al. (2023) chose a wider extension to estimate the net eastward transport of the DWBC including its recirculation, whereas Hall (2004) only chose the DWBC extension without including its northern recirculation.

Table 3.1. Key information of the A22 and A20 sections

	A22				A20			
	1997	2003	2012	**2021**	1997	2003	2012	**2021**
Station number	77	82	81	**90**	95	88	83	**90**
Sampling dates	Aug. 15 – Sept. 03	Oct. 23 – Nov. 13	Mar. 24 – Apr. 17	**Apr. 20 – May 16**	July 17 – Aug. 10	Sept. 22 – Oct. 20	Apr. 19 – May 15	**Mar. 21 – Apr. 13**
Season	Boreal summer	Boreal fall	Boreal spring	**Boreal spring**	Boreal summer	Boreal fall	Boreal spring	**Boreal spring**
Chief scientist	Terrence Joyce	Terrence Joyce & William Smethie Jr.	Ruth Curry	**Viviane Menezes**	Robert Pickard	John Toole & Alison MacDonald	Michael McCartney	**Ryan Woosley**
CTD	NBIS MK3	SeaBird 911plus	SeaBird 911plus	**SeaBird 911plus**	NBIS MK3	SeaBird 911plus	SeaBird 911plus	**SeaBird 911plus**
ADCP	S/LADCP	S/LADCP	S/LADCP	**S/LADCP**	S/LADCP	S/LADCP	S/LADCP	**S/LADCP**

The first estimates of the currents sampled in 1997 at the A22 location were shown by Joyce et al. (2001) using a one-box inverse model (refer to Appendix B). The GS mass transport was about 155 Sv. To the north of Puerto Rico, the DWBC transported 44 Sv, whereas it transported -37.5 Sv at the northern crossing. The net flow towards the Caribbean was -24 Sv. Casanova-Masjoan et al. (2018) used the data sampled during the 2003 and 2012 reoccupations to estimate the mass transports of these currents with the same inverse model. The GS transport was 100.1±4.6 Sv and 123.8±4.4 Sv, respectively. The northern/southern estimates of the DWBC were −17.3±2.9/30.9±10.3 Sv and −14.9±2.5/17.6±8.6 Sv, respectively. The net flow towards the Caribbean was −23.9±0.9 Sv in both years. Moreover, Casanova-Masjoan et al. (2018) also estimated the Antilles Current mass transport, which was −9.2±3.1 Sv in 2003 and −15.9±2.0 Sv in 2012.

This study, conducted in the same area as Casanova-Masjoan et al. (2018), Hall (2004), Joyce et al. (2001) and Santana-Toscano et al. (2023), introduces significant methodological differences. While previous studies applied a one-box inverse model separately to data from both the A20 and A20 sections, our research aims to compare the results from one-box inverse model to those from a three-box inverse model, using the hydrographic sections of A20 and A22 collected in 2021. According to Caínzos et al. (2023), single-section inverse models closely match data from the Rapid Climate Change–Meridional Overturning Circulation and Heat Flux Array (RAPID) and SAMoc Basin-wide Array (SAMBA) programs, as well as monthly outputs from ocean general circulation models (OGCM), when evaluated during the specific period of a given cruise. However, when inverse models integrate data from multiple sections across different latitudes and times of year over decadal timescales, they exhibit stronger alignment with decadal averages from the same OGCM models. This distinction underscores the limitations of single-section inverse box models, which are susceptible to aliasing and capture only the ocean’s state during the cruise period. In contrast, multi-section approaches effectively reduce aliasing, providing a more reliable assessment of low-frequency variability (Caínzos et al., 2023). This three-box model encompasses the water mass transport between three distinct boxes: between the A20 and the American Continent, between the A22 and the American Continent, and between the A20 and the A22 sections. This approach allows for a more complex representation of the system by considering the interactions between both sections. Thus, one of the primary objectives of this paper is to determine whether the three-box approach better captures the circulation regime in the area than the one-box approach. The one-box inverse models for the A20 and A22 have been developed using the same procedure as in prior studies (e.g., Casanova-Masjoan et al. (2018), Hall (2004), Joyce et al. (2001) and Santana-Toscano et al. (2023)).

3.2. Data and Methods

3.2.1 Hydrographic Data

Hydrographic data from spring 2021 were sampled along the A22 and A20 sections in the North Atlantic Ocean (Fig. 3.1). A total of 90 hydrographic stations were sampled in each survey using a rosette equipped with a SeaBird 911plus Conductivity-Temperature-Depth sensor (CTD), a set of two Teledyne RDI WH300 Lowered Acoustic Doppler Current Profilers (LADCP), a Teledyne RDI WH150 LADCP replacing the master ADCP in some stations of the A20 section, and 36 Niskin bottles with an absolute volume of 10.6L each. Additionally, Shipboard ADCP (SADCP) data were collected in both surveys (Table 3.1). Wind velocity data required to estimate the Ekman transport were retrieved from the National Center for Environmental Prediction Reanalysis II (NCEP-DOE) project from the National Oceanic and Atmospheric Administration (NOAA; Kanamitsu et al., 2002). The hourly data collected was averaged over the duration of each cruise, calculated at a height of 10 meters above the sea surface, and covered the distance between each section and the American coastline in a 2.5x2.5º grid, maintaining the same latitudinal boundaries as the cruises.

The property distributions of potential temperature (θ) and salinity show the water mass distribution for the A22 and A20 hydrographic sections (Figs. 3.2 and 3.3, respectively). Neutral density (γ^n; Jackett and McDougall, 1997) layers are shown in the background of both figures and are listed in Table 3.2 as the boundaries between the main water masses (Casanova-Masjoan et al., 2018; Santana-Toscano et al., 2023). A brief description of the water masses distribution follows.

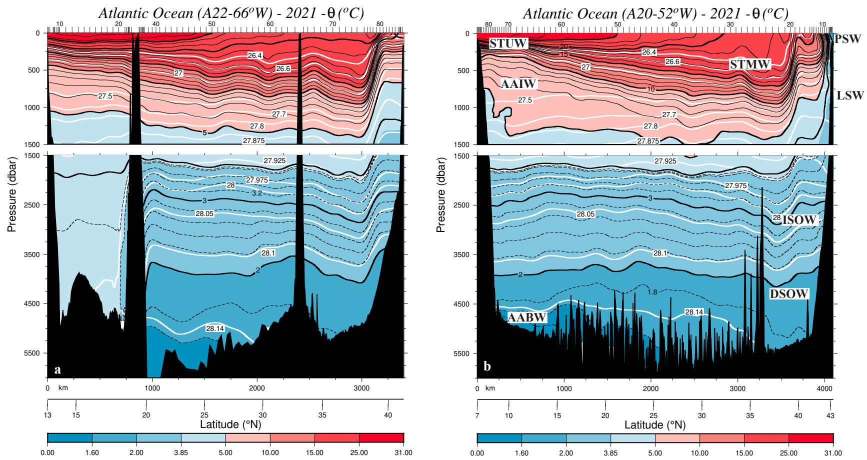

Figure 3.2. Vertical sections of potential temperature (θ, ºC) at A22 (66ºW) (a) and A20 (52ºW) (b) in the Atlantic Ocean. Neutral density (γ^n, kg m^{-3}) is overlayed in white lines. PSW: Polar Surface Water. STMW: Subtropical Mode Water. STUW: Subtropical Underwater. AAIW: Antarctic Intermediate Water. LSW: Labrador Sea Water. NADW: North Atlantic Deep Water. ISOW: Iceland-Scotland Overflow Water. DSOW: Denmark Strait Overflow Water. AABW: Antarctic Bottom Water.

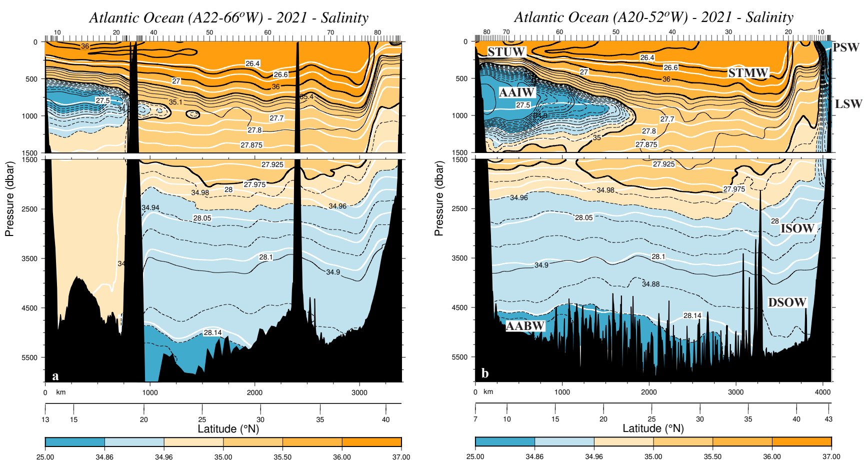

Figure 3.3. Same as Figure 3.2 but for salinity.

For the A20 hydrographic section, Polar Surface Water (PSW) appears to occupy the surface to 250 m depth at the northern end of the section with both low temperature (Fig. 3.2) and salinity (Fig. 3.3). Subtropical Mode Water (STMW), which is formed by convection in late winter (Joyce et al., 2013), is sampled south of the GS with salinities in the range of 36-36.5 (Fig. 3.3) in both sections. North Atlantic Subtropical UnderWater (STUW) shows a maximum in salinity (>36.5) in the upper 100 m depth on the southern side of both sections, from 5°N to 15°N (Fig. 3.3). AAIW arises as a distinguishable low salinity lobe of water below the STUW (Fig. 3.3) in both sections, occupying from 250 to 1250 m depth in the A20 section, and from 500 to 1250 m depth in the A22 section. Labrador Sea Water (LSW), the upper branch of the North Atlantic Deep Water (NADW), flows southwards from the Labrador Sea into the northern tip of the A20 section. It is sampled at latitudes >40°N and from below the PSW to 2000 m depth (Figs. 3.2 and 3.3). Iceland-Scotland Overflow Water (ISOW) and Denmark Strait Overflow Water (DSOW), the lower branches of the NADW, are found at 2000-4500 m depth.

Finally, AABW is a cool (<2ºC) and low salinity (<34.88) water mass found at the bottom of the ocean, below 4500 m depth (Figs. 3.2 and 3.3). The slight variations of the water masses meridional extension between the two sections were caused by their geographical location. The A22 section at 66ºW was located west of A20 and crosses the Antilles and samples part of the Caribbean Sea, while the A20 samples the western part of the NASG. The A20 also reaches further north than the A22, extending to the Grand Banks at 43ºN. Although the AAIW reaches the same latitude in both sections, it is observed further south in the A20 section than in the A22 section as they start at 7ºN and 13ºN, respectively. A similar case occurs in the sampling of the AABW because the A22 section samples it from outside of the Caribbean Sea at 10ºN to 30ºN, while the A20 section samples it from 7ºN to 30ºN.

Additionally, heat and freshwater fluxes between the ocean and the atmosphere have been analyzed using daily-averaged hourly data from ERA5, corresponding to the timing of each cruise.

3.2.2 Geostrophic Transport

The geostrophic velocity between station pairs is estimated using the thermal wind equation with the neutral density layer of γ^n=28.14 kg m^{-3} as the reference layer. This layer of no motion lies between the NADW and the AABW as they flow in opposite directions (Casanova-Masjoan et al., 2018; Joyce et al., 2001; Santana-Toscano et al., 2023). If the seafloor in a station pair is shallower than the level of no motion, as it happens in the northern part of the sections, the closest common depth layer is used as the reference level. Additionally, this relative geostrophic velocity is adjusted to the ADCP measurements following Comas-Rodríguez (2010) and Santana-Toscano et al. (2023). A brief explanation of the adjustment follows. The vertical profiles of mean SADCP between station pairs, mean LADCP of each station pair, and geostrophic velocities are visually compared at each station pair. An adjustment is then performed by selecting a depth interval where the velocities measured by ADCP match the geostrophic velocity. In cases where both SADCP and LADCP velocity profiles align with the geostrophic velocity, the SADCP profile is chosen for the adjustment because the LADCP velocities are located at each station rather than over the whole interval over which the geostrophic velocity is computed. In other words, the underway SADCP continuously collects data, so the SADCP can better match the location of the geostrophic calculation (Arumí-Planas et al., 2023). However, not every station pair undergoes this adjustment process due to the lack of a consistent similarity in shear between the ADCP and geostrophic velocity profiles. Therefore, the geostrophic velocity profile is not adjusted to any ADCP data, and the velocity of that station pair only has the geostrophic component. It is worth noting that the ADCP relies on particles within the water column to measure shear, and thus, when the backscatter is low (indicating low particle concentration), the ADCP may not accurately resolve the velocity shear. Examples of good adjustments at the GS location at A22/A20 are shown in Figure 3.4a, b, where the backscatter is high.

Although Casanova-Masjoan et al. (2018), Joyce et al. (2001) and Hall et al. (2004) used 17 neutral density layers, we have found the same outcropping of several isopycnals described in Santana-Toscano et al. (2023) and, therefore, we have followed their approach of dividing the water column into 14 neutral density layers (Table 3.2). The net mass imbalances computed from the geostrophic velocities are shown in Fig. 3.5a. The mass imbalances from the A20 (43.4 Sv), A22 (-27.1 Sv) and the net imbalance between the two sections (16.1 Sv) are reduced when ADCP velocities were added to the velocity field (-5.0 Sv, 12.9 Sv and 7.9 Sv, respectively; Fig. 3.5a).

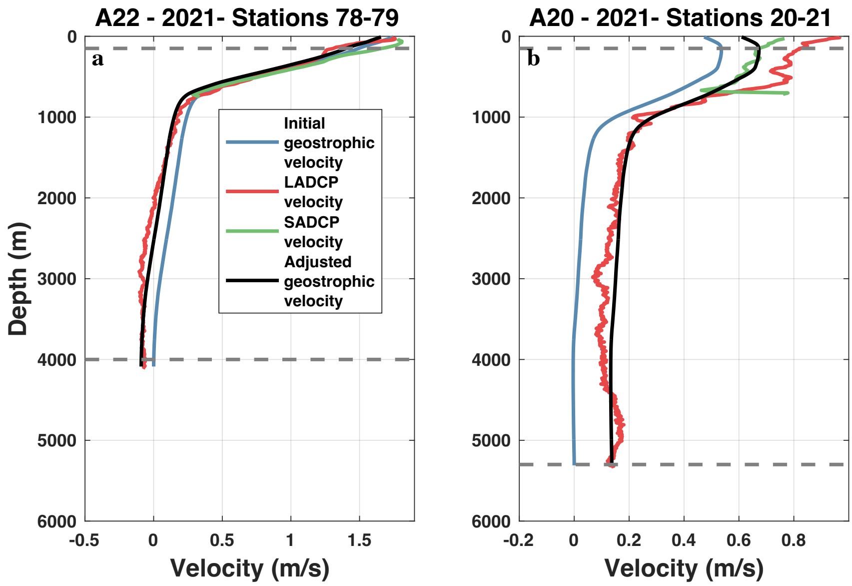

Figure 3.4. Initial geostrophic velocity (blue lines), LADCP (red lines) and SADCP velocities (green lines) and ADCP-adjusted geostrophic velocity (black lines) for the Gulf Stream location at the a) A22 (66ºW) and b) A20 (52ºW) sections. Gray dashed lines correspond to the depth range where the adjustment is made. X-axis varies between subplots.

Table 3.2. Neutral density limits for each layer and the corresponding water masses. Level of no motion is indicated in bold.

Layer	Neutral density (γ^n) range	Water mass
1	$\gamma^n < 26.4$	North Atlantic Subtropical Underwater (STUW)
2	$26.4 < \gamma^n < 26.6$	Subtropical Mode Water (STMW)

3	$26.6 < \gamma^n < 27$	Antarctic Intermediate Water (AAIW)
4	$27 < \gamma^n < 27.5$	
5	$27.5 < \gamma^n < 27.7$	
6	$27.7 < \gamma^n < 27.8$	
7	$27.8 < \gamma^n < 27.875$	Labrador Sea Water (LSW) / upper North Atlantic Deep
8	$27.875 < \gamma^n < 27.925$	Water (uNADW)
9	$27.925 < \gamma^n < 27.975$	
10	$27.975 < \gamma^n < 28$	Iceland-Scotland Overflow Water (ISOW) / lower NADW
11	$28 < \gamma^n < 28.05$	(lNADW)
12	$28.05 < \gamma^n < 28.1$	Denmark Strait Overflow Water (DSOW) / lNADW
13	$28.1 < \gamma^n <$ **28.14**	
14	**28.14** $< \gamma^n <$ bot.	Antarctic Bottom Water (AABW)

3.2.3 Inverse Box Model

Inverse box models are useful tools to estimate the unknown geostrophic reference velocity provided by the thermal wind equation and are needed to estimate the absolute mass, heat, and freshwater transports (Wunsch, 1996). The inverse model requires a set of equations and uncertainties, from which mass conservation is the most important equation (Wunsch, 1996; Wunsch, 1978). The inverse box model equations, formulated in a matrix form, are as follows (Hernández-Guerra & Talley, 2016):

$$Ab + n = -Y$$

where A is an mxn matrix with elements a_{ij} equal to the mass of the layer i at the station pair j; b is a column vector of length n containing the unknown geostrophic reference velocities b_j for each station pair plus the adjustment to the Ekman transport; n is a column vector of length m with elements n_i taking into account the noise of each equation; and Y is a column vector of length m with elements y_i equal to the mass transport imbalance in each layer resulting from the relative velocity plus the ADCP velocity. Appendix B contains a thorough explanation of the inverse model and the error estimates computation for each transport/flux.

In previous studies of the data collected from the hydrographic cruises carried out at 66ºW and 52ºW in 1997, 2003, and 2012, one box inverse model was applied (Casanova-Masjoan et al., 2018; Hall, 2004; Joyce et al., 1999, 2001; Santana-Toscano et al., 2023). On this occasion, we have carried out an inverse model consisting of three boxes for the hydrographic data measured in 2021 and compared its results with those from one box inverse model applied to each hydrographic section independently, as previously done. Thus, the inverse model consists of three boxes comprising the water mass between the A20 section and the American continent (box 1), the A22 section and the American continent (box 2), and the A20 and A22 sections (box 3). The inverse problem consists of 49 mass conservation equations built as follows (Table 3.3). Each box contains 14 mass conservation equations, one for each layer of the ocean obeying the distribution shown in Table 3.2, plus an additional mass conservation equation for each whole box (equation numbers 1-15 for box 1, 16-22 and 25-32 for box 2 and 35-49 for box 3). Two additional equations were added in box 2 as the deep transport of the Caribbean in layers 8 and 9 is not connected to the deep transport in the Atlantic Ocean (equation numbers 23-24). Equations 33 and 34 of box 2 refer to the total deep transport of the Caribbean (layers 8 and 9) and the total deep transport of the Atlantic Ocean without the Caribbean basin (layers 8 to 14), respectively. At the same time, the total unknowns are 176: 89 from the number of station pairs of the A20 section, 85 for station pairs of the A22 section, and 2 unknowns from the adjustments of each Ekman transport added to the shallowest layer in each hydrographic section. Likewise, the one-box inverse models for the A20-continent and A22-continent have been configured with the same terms as previous boxes 1 and 2, respectively. The inverse problem is solved through the Gauss-Markov method, which provides a solution for the initial estimates with minimum error variances. This method requires a priori variances for each velocity and each equation (Wunsch, 1996). For the a priori velocity variance, a value of $(0.03 \text{ m s}^{-1})^2$ is considered for all station pairs with ADCP-adjusted velocities and a higher value of $(0.06 \text{ m s}^{-1})^2$ for the rest (Joyce et al., 2001). For the equation's a priori variance, higher values are considered in surface layers than in the deep layers and the total mass transport equations (Joyce et al., 2001). These values are $(2 \text{ Sv})^2$ for the first seven layers, and $(1 \text{ Sv})^2$ for the rest of the deep layers and the overall equation (Table 3.3).

The velocities at the reference level (with their error estimates) from the single-box/three-box inverse models are presented in Fig. 3.6.a/b (green/red, A22) and Fig. 3.6.d/e (orange/blue, A20). The added ADCP velocities are represented in black in Fig. 3.6.a, b, d, e. The distribution of the A22 velocities does not differ significantly from zero (Fig. 3.6.a, b; the significance between two values has been asserted as the overlap of the two values ± their respective errors). The DWBC and the GS velocities are remarkably different from zero in the A20 section, while the ocean interior shows velocities not significantly different from zero (Fig. 3.6.d, e) as previous inverse models found (Arumí-Planas et al., 2023; Caínzos et al., 2022; Caínzos et al., 2023; Hernández-Guerra et al., 2005, 2014, 2019; Pérez-Hernández et al., 2023; Vélez-Belchí et al., 2017). Fig. 3.6c, f, which represents the difference between the velocities from the three-box and one-box inverse models, shows slight velocity disparity but not statistically different from zero. Therefore, the results of the three-box inverse model have been used to estimate the adjusted zonal circulation and the heat and freshwater transports. Since there is negligible difference between the results of the single and three-box inverse models' velocities, any derived outcomes (e.g., mass transports) reflect the same underlying conclusions. Thus, presenting the results of the three-box inverse model in this paper is equivalent to presenting those of the single-box model. Therefore, there is not a source of discrepancy when these results are compared to previous single-box model outcomes.

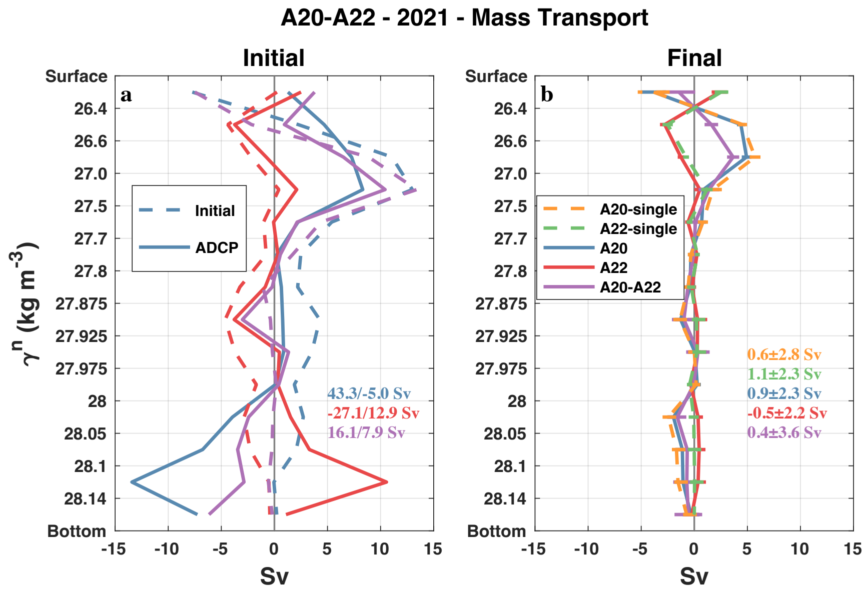

Figure 3.5. Meridionally integrated mass transport (Sv) across the A22 (66ºW) section (red), the A20 (52ºW) section (blue) and the sum of both sections (purple) estimated from the initial geostrophic velocity (a, dashed lines), from the ADCP-adjusted geostrophic velocities (a, solid lines) and from the inverse-adjusted velocities (b, solid lines). Same results from the single A22 (66ºW) and A20 (52ºW) inverse-adjusted velocities are shown in b (green and yellow dashed lines, respectively). Total mass transport imbalances are shown in their respective colors.

Table 3.3. Mass conserving equations applied to the inverse three-box model. All equations are the mass conserving equation presented in Appendix A, but applied to either a single layer or the entire water column, as specified.

Box	Layers	Equation number	A priori uncertainty
1: A20-continent	1-7	1-7	$(2\ Sv)^2$
	8-14	8-14	$(1\ Sv)^2$
	Overall (sum of equations 1-14)	15	$(1\ Sv)^2$
2: A22-continent	1-7	16-22	$(2\ Sv)^2$
	8-9 (Caribbean)	23-24	$(1\ Sv)^2$
	8-14 (Atlantic)	25-31	$(1\ Sv)^2$
	Overall (sum of equations 16-22 and 25-31)	32	$(1\ Sv)^2$
	Overall (sum of equations 23-24)	33	$(1\ Sv)^2$
	Overall (sum of equations 25-31)	34	$(1\ Sv)^2$
3: A20-A22	1-7	35-41	$(2\ Sv)^2$
	8-14 (only Atlantic)	42-48	$(1\ Sv)^2$
	Overall (sum of equations 35-41 and 42-48)	49	$(1\ Sv)^2$

3.3. Results

3.3.1 Adjusted Zonal Circulation

The zonal mass transport per neutral density layer with its net imbalance is shown in Fig. 3.5b. Both the single-box and three-box inverse models have reduced the ADCP-adjusted imbalances to values not significantly different from zero (0.6±2.8 Sv and 1.1±2.3 Sv for the single-box A20 and A22 inverse models and 0.9±2.3 Sv, -0.5±2.2 Sv, and 0.4±3.6 Sv for the box 1, 2 and 3 inverse models, respectively). Ekman transports of the A22 and A20 sections were initially -0.2±0.1 Sv and -1.4±0.3 Sv, respectively. After the inverse model, the Ekman transports are -0.1±0.2 Sv and -0.9±0.5 Sv. The zonal transport distribution through latitudes and density layers provides the estimates of mass transport of the main currents of the AMOC (Fig. 3.7). In this figure, we have also added the zonal distribution of mass transport as a result of the one-box inverse models for comparison although we will only mention the results for three-box inverse models. As our integration starts in the southern latitude, we start our description from there. All mass transports are computed following the latitudinal ranges and methodological approaches established in previous works using one-box inverse models by Casanova-Masjoan et al. (2018) and Hernández-Guerra and Joyce (2000). By using the same latitudinal ranges and similar hydrographic sections used in these one-box inverse models, it is ensured that our three-box inverse model results are directly comparable to earlier studies, facilitating an accurate comparison of transport estimates over time.

The NBC originates south of the equator when the South Equatorial Current (SEC) reaches the South American coast (da Silveira et al., 1994). This current encompasses the northward flow of the upper and intermediate layers of the tropical South Atlantic, resulting in a highly variable transport of approximately 16 Sv between 11°S and 5°S (Dossa et al., 2021; Garzoli et al., 2004; Johns et al., 1998; Schott et al., 2005; Stramma et al., 1995). Dossa et al. (2021) calculated a northwestward transport of 14.2 ± 4.2 Sv at 5ºS, 36ºW, highlighting that the NBC represents a reduction in transport compared to the stronger flow of the Brazil Current further south in the South Atlantic (below 11ºS). As it crosses the equator, the NBC transport diminishes again due to seasonal retroflection into the equatorial current system (Johns et al., 1998). At the A20 location (52ºW) and between 6.9-

9.5ºN, the NBC exhibits a mass transport of -17.4±1.9 Sv (Table 3.4), estimated from the surface to γ^n=27.8 kg m^{-3} (~1400 m depth, layers 1-6, Fig. 3.7a, b). Simultaneously, the NEC flows westwards (-23.4±4.3 Sv, Table 4) and is situated north of the NBC (in the latitude range 17.4-25.0ºN, Fig. 3.7a, b). The NEC is fed by the southern branches of the Azores Current and the Canary Current (Hernández-Guerra et al., 2002; Stramma, 1984). At the A22 section (12.6-21.1ºN), the net westward flow of the NBC and NEC contributes to both the flow of the Caribbean Sea and the Antilles Current between the surface and γ^n=27.8 kg m^{-3} (~1400 m depth, layers 1-6), with respective transports of -19.7±0.6 Sv and -14.2±2.0 Sv (Fig. 3.7a, b) (Bryden et al., 2005; Hernández-Guerra et al., 2010; Johns et al., 2008). In the Caribbean Sea (12.6-17.8ºN) at A22 and between layers 7 to 9 (1250-4500 m depth), three consecutive gyres are observed (Fig. 3.7c), as previously mentioned in Casanova-Masjoan et al. (2018). These three gyres are smaller eddies; they cannot be classified as recirculating fluxes since their net transport is zero, nor can they be rings branching from the flow of the Caribbean Sea, as they are located beneath it (in layers 7-9 and 3-6, respectively). The first eddy is cyclonic, characterized by a positive transport at 13-14°N (Fig. 3.7c), followed by a negative transport at 14-15°N (Fig. 3.7c). The next two consecutive eddies are both anticyclonic, exhibiting negative transport followed by positive transport at 15.5-16.5°N and 17-18°N, respectively (Fig. 3.7c).

The Florida Current receives an influx by the westward transport within the Caribbean Sea, then, it converges with the Antilles Current north of the Bahamas. This interaction contributes to the GS poleward transport, as described by Meinen et al. (2019). The GS mass transport is known to increase downstream, ranging from about 32 Sv in the Florida Current to 100-150 Sv in the open North Atlantic Ocean (Leaman et al., 1989; Meinen et al., 2010). The computation of the GS mass transport is conducted within specific latitudinal ranges, namely 36.9-38.4ºN for A22 (66ºW) and 37.6-40.9ºN for A20 (52ºW). The GS spans from the surface to the seafloor (~5250 m depth, layer 13; Fig. 3.7a, b, c, d). The GS mass transport at the A22/A20 locations are 103.7±3.5/97.3±3.6 Sv (Table 3.4). Immediately south of the GS, a westward recirculation known as the GS recirculation (GSR) occurs (Casanova-Masjoan et al., 2018; Santana-Toscano et al., 2023). The GSR is computed within latitudinal ranges of 33.2-36.9ºN for A22 and 33.8-37.6ºN for A20, resulting in mass transports of –73.6±4.3/–52.8±4.2 Sv, respectively (Fig. 3.7a, b, c, d; Table 4). The latitudinal ranges and density levels chosen to compute the GS and GSR mass transports follows closely the approaches of Casanova-Masjoan et al. (2018) and Santana-Toscano et al. (2023) for the A22 and A20 sections, respectively. The negative (westward) signal of the GSR in Fig. 3.7a, b, c and d from 33.2ºN to 36.9ºN (A22) and from 33.8ºN to 37.6ºN (A20) is visually coherent through the density layers chosen (Table 3.4). The same approach is used to compute the GS mass transport. The positive (eastward) signal just after the GSR (36.9-38.4ºN for the A22 and 37.6-40.9ºN for the A20) is coherent through the density layers chosen (Table 3.4). As the GS loses heat to the atmosphere along its trajectory toward the pole, it undergoes cooling and increases its density in the northern North Atlantic. Consequently, it descends to deeper layers (γ^n=27.875 kg m^{-3} to γ^n=28.14 kg m^{-3}, layers 7-13) and flows to the south as the DWBC (Talley et al., 2011). The DWBC flows from the northern North Atlantic to the equator through the western NASG. It crosses the 52ºW longitude at 40.9-42.2ºN (A20, Fig. 3.7c, d) with a mass transport of -25.4±6.1 Sv in spring 2021 (Table 3.4). Along its path, the DWBC also reaches 66ºW, traversing the latitudinal ranges of 36.4-39.1ºN at the northern crossing and 18.6-23.6 ºN at the southern crossing (A22, Fig. 3.7c, d). At these locations, its mass transports are -19.1±5.7 Sv and 19.1±7.6 Sv, respectively (Table 3.4). Then, the DWBC progresses to the equator and crosses again the 52ºW longitude, but this time in the latitude range of 8.9-9.8ºN (A20, Fig. 3.7c, d). The DWBC mass transport at this location is 21.8±3.7 Sv (Table 3.4).

Finally, the AABW is confined to the deepest layer, between the neutral density layer of γ^n=28.14 kg m^{-3} (~4750 m depth, layer 14) and the bottom of the ocean (~5500 m depth). Although its net transport is zero, its westward mass transport is -3.9±3.1 / -2.7±3.4 Sv (Table 3.4) between the latitudinal ranges 22.6-25.6 / 15.1-21.0 ºN (Fig. 3.7e) for the A22/A20 sections. The meridional distribution of this flow of the AABW consists of three relatively large anticyclonic gyres spanning approximately 10-15 ºN, 22-27 ºN, and 27-34 ºN at the A20 section. However, only one cyclonic gyre appears at the A22 section, spanning from 20 to 25 ºN. This distribution seems to be coupled to the shallower deep layers as they present the same meridional structure (Fig. 3.7e).

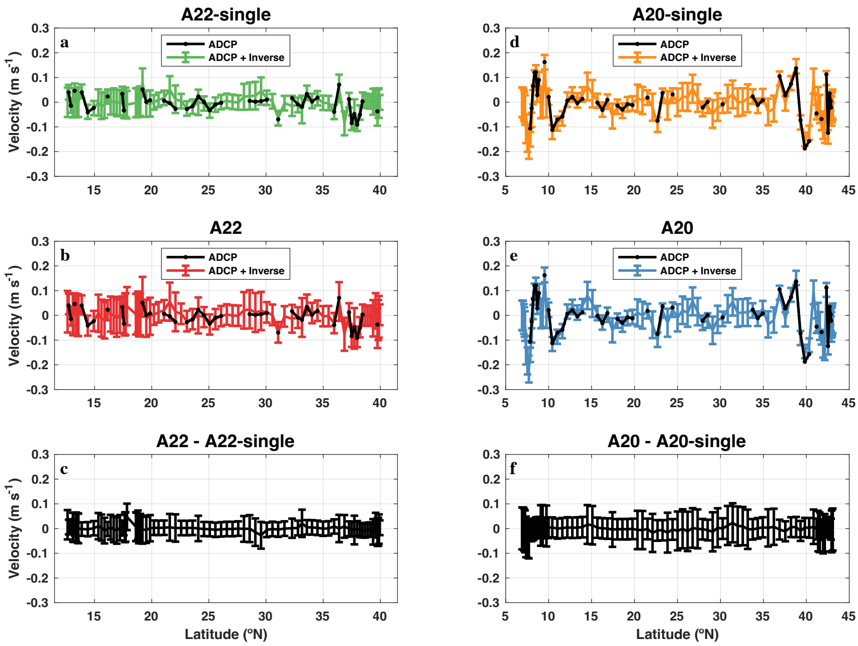

Figure 3.6. ADCP-adjusted geostrophic velocity (black lines) and ADCP-adjusted velocity plus the reference level velocity estimated from the inverse model versus latitude for the A22 (66ºW) and A20 (52ºW) single inverse box models (a and d, respectively), for the three-box inverse model including both A22 (66ºW) and A20 (52ºW)sections (b and e, respectively) and for the difference between the three-box and single-box inverse models (c and f). Error bars correspond to inverse modeling calculations. Gaps in the ADCP-adjusted velocity correspond to station pairs where the initial geostrophic velocity could not be adjusted to ADCP velocity. X-axis varies between the two sections.

3.3.2 Heat and Freshwater Fluxes

The heat transport west of the two surveys is estimated from the inverse model result:

$$\mathrm{H} = \sum_i \sum_j c_{p_{ij}} pt_{ij} \rho_{ij} y_{ij} z_{ij} u_{ij}$$

where H is the net heat transport across the section (PW), $c_{p_{ij}}$ is the specific heat capacity ($m^2 s^{-2} °C^{-1}$) in layer i at station pair j, pt_{ij} is the potential temperature (°C), ρ_{ij} is the neutral density (kg m^{-3}), y_{ij} is the horizontal distance (m), z_{ij} is the vertical distance (m) and u_{ij} is the perpendicular velocity (m s^{-1}) to the section from the inverse model. The heat flux is not different from zero in the A20 section (0.1±0.1 PW; 1 PW = 10^{15} W) and in the A22 section (-0.1±0.1 PW). Additionally, the heat flux from the ERA5 daily-averaged hourly data at the water surface, computed as the sum of the net solar radiation at the surface, the latent, thermal and sensible heats, yields values of 0.1±2.3 PW and 0.3±0.8 PW for the A20 and A22 sections, respectively. Both values reveal a slightly positive net heat flux at the water surface, but not significantly different from zero. The ERA5 datasets used consists in hourly data for the aforementioned variables in the areas enclosed by the A20-American continent and A22-American continent, respectively. This hourly data spans the duration of the hydrographic cruises.

The freshwater flux shows the air-sea interactions of the waters enclosed by an oceanographic section. In this work, the freshwater fluxes west of the two surveys are estimated as in Joyce et al. (2001):

$$\bar{F} = -\sum_i \sum_j T_{ij} S'_{ij} / S_0$$

where $\bar{F}$ is the excess of precipitation plus runoff over evaporation in the closed volume, T_{ij} is the mass transport in layer i at station pair j from the inverse model, S_0 is the mean salinity, and S'_{ij}=S_{ij}-S_0, the salinity anomaly.

The resulting freshwater fluxes are 0.1±0.1 Sv and -0.1±0.1 Sv for the A20 and A22 sections, respectively. Similar to the heat flux estimates, both freshwater fluxes are not significantly different from zero. Additionally, the freshwater flux from the ERA5 daily-averaged hourly data at the water surface, computed as the sum of total precipitation, evaporation and runoff, provides a value of -0.2±1.7 Sv and -0.1±0.5 Sv for the A20 and A22 sections, respectively. These values are not significantly different from those obtained through the inverse model results based on hydrographic data. The ERA5 product used comprises hourly data of the variables cited before in the areas bounded by the A20-American continent and A22-American continent, respectively. This hourly data spans the duration of the hydrographic cruises.

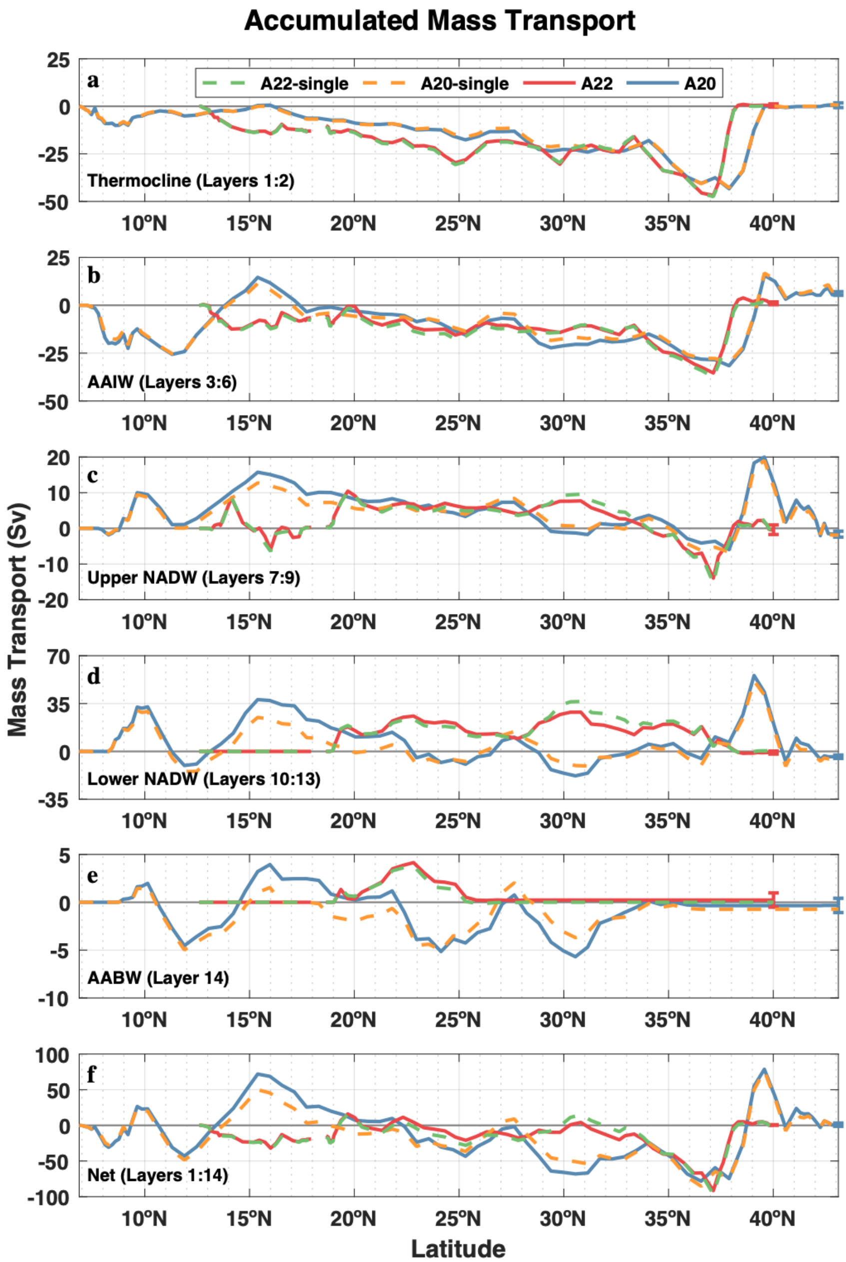

Fig. 3.7. Northward accumulated mass transport (Sv) after the single-box and three-box inverse models for the A22 (66ºW) (dashed green and solid red lines, respectively) and A20 (52ºW) (dashed orange and solid blue lines, respectively) hydrographic sections. (a) Thermocline transport estimated for layers 1 to 2. (b) AAIW transport estimated for layers 3 to 6. (c) Upper NADW transport estimated for layers 7 to

9. (d) Lower NADW transport estimated for layers 10 to 13. (e) AABW transport estimated for layer 14. (f) Net transport estimated for layers 1 to 14. Y-axis range varies between subplots.

Table 3.4. Mass transports, latitude range and layers of the main currents of the A22 and the A20 sections computed from the three-box inverse solution

		A22		A20	
	Layers	Latitudinal range (ºN)	Transport (Sv)	Latitudinal range (ºN)	Transport (Sv)
Caribbean	1:6	12.6-17.8	-19.7±0.6		
Antilles Current	1:6	18.6-21.1	-14.2±2.0		
NBC	1:6			6.9-9.5	-17.4±1.9
NEC	1:3			17.4-25.0	-23.4±4.3
GSR	1:13	33.2-36.9	-73.6±4.3	33.8-37.6	-52.8±4.2
GS	1:13	36.9-38.4	103.7±3.5	37.6-40.9	97.3±3.6
North DWBC	7:13	36.4-39.1	-19.1±5.7	40.9-42.2	-25.4±6.1
South DWBC	7:13	18.6-23.6	19.1±7.6	8.9-9.8	21.8±3.7
AABW	14	22.6-25.6	-3.9±3.1	15.1-21.0	-2.7±3.4

3.4. Discussion

This study provides valuable insights into the use of single- versus three-box inverse models for analyzing zonal circulation in the North Atlantic Ocean. Consistent with previous findings (Arumí-Planas et al., 2023; Caínzos et al., 2023), single-box models in our analysis effectively capture short-term variability, as shown by the results for the 2021 hydrographic data. This supports the idea that single-box models represent the ocean state at the time of the cruise. The two sections analyzed in this study were sampled during the same season, making the results representative of the ocean's state during that specific period rather than a decadal average. This seasonal consistency ensures the reliability of the single-box model in capturing GS transports for the time of observation. Remarkably, despite this seasonal representation, the GS transports derived from this work align well with decadal means reported in previous studies. This agreement likely reflects the stability and dominance of the GS within the broader circulation system, where its variability is relatively well-constrained over longer timescales.

This study has also provided recent estimations of the mass transport of the main components of the AMOC and the zonal currents at 52 ºW and 66ºW in the western NASG for the 2021 A22/A20 occupations. It has also provided estimations of the heat and freshwater fluxes occurring in the enclosed water volume.

The NBC is a northward-flowing current that has its origins on the Brazilian continental shelf. During the spring of 2021 and at the 52ºW longitude, the NBC transports -17.4±1.9 Sv. As previously stated, the NBC is a highly variable current with an average transport of approximately 16 Sv, representing a reduction in flow compared to the Brazil Current south of 11ºS (Johns et al., 1998; Schott et al., 2005; Stramma et al., 1995). Both this result and the spring 2012 result (-15.6±1.6 Sv) estimated by Santana-Toscano et al. (2023) agree with this decreasing transport northward. Likewise, estimates from other seasons by Santana-Toscano et al. (2023) also supports the transport reduction northward of the equator (–5.6±0.7 Sv and -15.8±1.2 Sv for 1997-summer and 2003-fall, respectively). The yearly mean estimate (-16±2 Sv) presented by Garzoli et al. (2004) using inverted echo sounders at 2-3ºN, 47.4-47.1ºW during 1998-

1999 coincides with the previous fall and spring values, which may indicate that these estimates are representative of the mean values of their respective years of sampling. North of the NBC and at 52ºW, the NEC flows westwards with a mass transport of -23.4±4.3 Sv. This result significantly differs from the spring estimate computed from 2012 data by Santana-Toscano et al. (2023) (-10.6±2.8 Sv). This difference may suggest that an interannual variability of the NEC's transport predominates, which should be addressed by studying the variability of its feeding currents: the southern branches of the Azores Current and the Canary Current (Hernández-Guerra et al., 2002; Stramma, 1984). This is possibly corroborated with Santana-Toscano et al. (2023)'s study that indicate a weakening of the NEC in fall and spring (-12.3±3.6 Sv and -10.6±2.8 Sv, respectively) compared to summer (-28.6±2.5 Sv), which does not agree with the spring value found here (-23.4±4.3 Sv). Thus, interannual variability of the three sampling periods is the most plausible explanation for the NEC variability than seasonality.

The net westward flow of the NBC and NEC feed the Caribbean Sea flow (-19.7±0.6 Sv) and the Antilles Current (-14.2±2.0 Sv). The mass transport estimate inside of the Caribbean Sea from spring 2021 (-19.7±0.6 Sv) is significantly weaker than the mass transports estimated in previous studies at the same location (-24 Sv in summer 1997 by Joyce et al., 2001; and -24.4±1.0 Sv and -24.2±1.1 Sv in fall 2003 and spring 2012 by Casanova-Masjoan et al., 2018). This difference should not be attributed to the NBC/NEC variability, as their strengthening/weakening over the four sampling periods does not correlate with the variability in flow in the Caribbean Sea. Thus, the causes of the weaker flow in the Caribbean Sea in 2021-spring should be searched in its other feeding sources. Although the Antilles Current has not been estimated in summer 1997, the mass transport for the 2003-fall (-9.2±3.1 Sv) and 2012-spring (-15.9±2.0 Sv) by Casanova-Masjoan et al. (2018) are not significantly different from our 2021-spring estimates (-14.2±2.0 Sv). However, the mean estimate over 11 years (1986-1997) of a deployed mooring over 26.5ºN (Bryden et al., 2005) reveals a weaker transport of the Antilles Current (5.1 Sv, no error estimate given). Similar results were found later in the same region by Meinen et al. (2004) using 1-year-long records of inverted echo sounders (6±3 Sv), by Johns et al. (2008) between March 2004 - May 2005 (6.0 Sv, no error estimate given) and by Meinen et al. (2019) in the period 2005-2015 (4.7±7.5 Sv).

These transports were computed as northward components at 26.5ºN while both Casanova-Masjoan et al. (2018) and this study's results were computed as westward components in the range of ~18-20ºN. Likewise, the depth range is also different between those two estimates (0-1000m depth) and the ones from Casanova-Masjoan et al. (2018) and ours (0-1200m and 0-1400m depth, respectively). Therefore, the different zonal/meridional and depth boundaries where the Antilles Current transport is estimated may explain the results disparities shown above. A thorough study of the components of the Antilles Current between 18-25ºN may enlighten these discrepancies.

The Caribbean Sea flow feeds the Florida Current, which flows northward outside of the Caribbean Basin and converges with the Antilles Current to form the GS. At the A22 section location (66ºW), the GS carries 103.7±3.5 Sv in 2021-spring. Just south of it, the GSR transports –73.6±4.3 Sv to the west. Therefore, a net eastward transport of 30.1±5.5 Sv flows towards the A20 section location (52ºW). According to Casanova-Masjoan et al. (2018), the net eastward transports in spring 2012 and fall 2003 from the GS (123.8±4.4 Sv and 100.1±4.6 Sv, respectively) and the GSR (−43.0±10.9 Sv and −59.8±8.8 Sv, respectively) transports are 80.8±11.6 Sv and 40.3±9.9 Sv, respectively. Not only are significant differences found between transports in the same season (30.1±5.5 Sv and 80.8±11.6 Sv in the spring of 2021 and 2012), but the 2021-spring value is like the 2003-fall value. Thus, the GS system may potentially present both seasonal and interannual variability at this location. The GS, on its path to the northern North Atlantic, crosses the A20 section (52ºW) with a mass transport of 97.3±3.6 Sv in 2021-spring. Just south of it, the GSR transports -52.8±4.2 Sv to the west. Therefore, the net eastward transport of the GS system is 44.5±5.5 Sv. According to Santana-Toscano et al. (2023), the net eastward transports in spring 2012 and fall 2003 from the GS system (181.1±14.9/-145.3±19.8 Sv and 102.7±13.5/-72.3±17.4 Sv for the GS/GSR, respectively) are 35.8±24.8 Sv and 30.4±22.0 Sv, respectively. While the fall 2003 estimate coming from 66ºW is not significantly different from the estimate at 52ºW, the GS system transports significantly differ in spring 2012 and spring 2021. As stated before, the GS system variability may be influenced not only by seasonal variability, but also by interannual variability (Pérez-Hernández & Joyce, 2014). The GS mass transports of the A22 and

A20 sections calculated in this study (103.7±3.5 Sv and 97.3±3.6 Sv, respectively) align with the 2010-2014 4-year mean GS transport (102 Sv) at 68.5ºW, derived from Oleander Line and Line W data (Andres et al., 2020). This agreement confirms the reliability of the inverse box model methodology and highlights the effectiveness of inverse modeling as an effective tool for observing GS mass transports in the future.

The GS flows poleward and, during its journey, transfers heat to the atmosphere. This process results in a cooling of the water mass and an increase in density. Because of this increased density, the water mass sinks to deeper ocean layers (γ^n=27.875 kg m^{-3} to γ^n=28.14 kg m^{-3}, layers 7-13) and begins to circulate to the south as the DWBC (Talley et al., 2011). At the A20 location (52ºW), the DWBC flows with a mass transport of -25.4±6.1 Sv during spring 2021. It is not significantly different from previous results presented in 2012-spring, 2003-fall, and 1997-summer (-37.9±10.2 Sv, -14.4±10.8 Sv and -21.2±8.9 Sv, respectively) (Santana-Toscano et al., 2023). This westward flow arrives at 66ºW (A22) with a mass transport of -19.1±5.7 Sv, which is consistent with the mass transport at 52ºW. As occurred at 52ºW, the mass transport of the DWBC is not significantly different from previously estimated DWBC transports at the same location (-14.9±2.5 Sv and -17.3±2.9 Sv for 2012-spring and 2003-fall) (Casanova-Masjoan et al., 2018). The DWBC flows equatorward and crosses eastward at 66ºW with a mass transport of 19.1±7.6 Sv. Previous measurements of the DWBC sampled in different seasons at the same location are not statistically different (17.6±8.6 Sv and 30.9±10.3 Sv for 2012-spring and 2003-fall, respectively; Casanova-Masjoan et al., 2018). Lastly, the DWBC flows through the A20 section with a mass transport of 21.8±3.7 Sv. In contrast, the DWBC presents a lower mass transport (44.5±9.8 Sv, 2012-spring) in the last spring estimate. However, fall 2003 and summer 1997 estimates (14.2±8.1 Sv and 29.0±9.1 Sv) are still consistent with the mass transport in 2021. Overall, the DWBC mass transports appear to remain constant over the years, with the exceptions of the southern-crossing DWBC at 52ºW in 2012-spring, which seems anomalous when compared to the spring 2021 estimate and from its feeding transport at 66ºW. The DWBC mass transports computed here at the northern crossings of the two sections (-25.4±6.1 Sv and -19.1±5.7 Sv at the A20 and A22 sections) are also consistent with the 4-year (2004-2014) mean DWBC transport computed from high resolution mooring data at Line W (22.8±1.9 Sv; Toole et al., 2017). Since 2004, the DWBC transport has been monitored using current meter-equipped moorings at the western end of the RAPID array. These measurements reveal a time-mean transport of −31.0 ± 1.0 Sv with a standard deviation of approximately 19 Sv based on 12-hourly data (Johnson et al., 2023). The DWBC transport observed in both southern crossings during this study (19.1±7.6 Sv and 21.8±3.7 Sv at 66ºW and 52ºW, respectively) aligns well with the range of values recorded by the RAPID array. This consistency between the DWBC transports computed from inverse box models and long-term observational data, similar to the agreement observed for the GS transports, further reinforces the robustness and reliability of the inverse box model methodology across different oceanic current systems, making it a valuable tool for future large-scale circulation studies. Nevertheless, the DWBC transport estimates at 66°W (19.1 ± 7.6 Sv) and 52°W (21.8 ± 3.7 Sv) from this study are lower than those reported by Biló and Johns (2020) at 26.5ºN. Observations from LADCP and CTD casts (2001–2018) indicate transport values of −31.15 ± 7.7 Sv and −29.30 ± 4.2 Sv, respectively, while mooring data (2008–2018) show a mean transport of −28.34 ± 3.8 Sv. Model outputs from the eddy-resolving Ocean Model For the Earth Simulator (OFES) estimate a much lower transport of −9.33 Sv (Biló & Johns, 2020). Nevertheless, Argo-based geostrophic velocity fields (2004–2016) yield −22.79 ± 8.7 Sv (Biló & Johns, 2020), which align with the results presented in this work. These discrepancies underscore the regional variability of the DWBC and the influence of differing methodologies, spatial resolution, and temporal coverage used in each study.

The heat fluxes estimated in the water volumes enclosed between the American Continent and the A20 (52ºW) section (0.1±0.1 PW) and between the American Continent and the A22 (66ºW) section (-0.1±0.1 PW) are not significantly different from zero. Although the A20 heat flux differs greatly from the previous estimate in the same season (spring 2012) and for the 1997-summer estimate (-0.6±0.1 PW and -0.7±0.1 PW, respectively), our estimated heat transport is not significantly different from the fall estimate (0.1±0.1 PW; Santana-Toscano et al., 2023). This result suggests that the oceanographic conditions in spring 2021 and fall 2003 were similar, as the GS transports are not significantly different during those periods. The A22 heat flux does not present significant changes from previous sampled seasons (-0.2±0.1 PW for both spring 2012 and fall 2003; Casanova-Masjoan et al., 2018) except for 1997-summer (-0.4±0.1 PW; Joyce et al., 2001) during which the heat loss to the atmosphere is lower.

The freshwater fluxes estimated are 0.1±0.1 Sv and -0.1±0.1 Sv (A20 and A22), respectively. This implies that no gain/loss of freshwater occurs west of both 66ºW and 52ºW. A20 (52ºW) freshwater flux is significantly different from the other sampled periods (0.6±0.1 Sv, 0.3±0.1 Sv and 0.6±0.1 Sv for 2012-spring, 2003-fall and 1997-summer; Santana-Toscano et al., 2023). Additionally, the A22 (66ºW) freshwater flux is significantly different from the same-season estimate in 2012 (0.2±0.1 Sv, Casanova-Masjoan et al., 2018) and for the summer 1997 estimate (0.3±0.1 Sv; Joyce et al., 2001). Thus, the variability of the freshwater fluxes does not reveal a seasonality pattern as the estimates from the same season significantly differ. Therefore, the variability of the freshwater flux over the A20 and A22 hydrographic sections may be attributed to the interannual scale.

A value of zero in terms of heat and freshwater fluxes is indeed significant. It can indicate that, for the period under investigation (March-May 2021), the system may not have experienced significant divergence or convergence in heat/freshwater across the section analyzed. Thus, a zero flux should not be interpreted as a limitation but rather as an important finding.

These fluxes have been compared previously to the ERA5-derived heat/freshwater flux estimates, and the values were not significantly different than our result. This further supports the robustness of the inverse box method and the relevance of the zero-flux result for March-May 2021. Moreover, the inverse box model method used to calculate these fluxes has been validated through various studies, producing non-zero results for the heat/freshwater fluxes in other scenarios (Casanova-Masjoan et al., 2018; Hall, 2004; Joyce et al., 1999, 2001; Santana-Toscano et al., 2023). Hence, there is no inherent limitation in the methodology that would cause the fluxes to artificially trend towards zero.

This work illustrates the consistent mass transports of the main AMOC currents at the western NASG, specifically the GS and the DWBC. By focusing on them, the study provides a robust depiction of the persistent and stable nature of their mass transport, which is crucial for understanding the larger climatic and oceanographic processes influenced by the AMOC. The inverse methodology used in previous works makes the findings reliable and ensures that the representation of these two limbs of the AMOC, along with the other currents studied in this paper, is also accurate. This consistency is fundamental in assessing the role these currents play in global heat distribution and their impacts on climate systems in comparison to previous works. While this study's use of seasonally sampled data has certain limitations, it is important to recognize the unique strengths of GO-SHIP surveys. These surveys provide the highest spatial resolution, covering the entire ocean basin from coast to coast, which other observational methods cannot achieve. Moreover, GO-SHIP data offer the most accurate measurements, making them essential for calibrating long-term time series collected by other instruments. Although seasonal sampling might not fully capture interannual or decadal variability, the precision and breadth of GO-SHIP surveys remain invaluable for understanding the AMOC's behavior. Rather than being a drawback, these surveys serve as a critical foundation upon which other methods can build. Nevertheless, incorporating continuous, long-term monitoring in future research would complement the GO-SHIP data, offering a more detailed understanding of episodic events and long-term shifts that influence the GS and DWBC. It's also important to note that AMOC strength and stability depend on interior flows and eastern boundary currents, which are beyond the scope of this study.

Building upon the findings of this study, a promising avenue for future research involves extending the inverse box model methodology to longer timescales and higher temporal resolutions using existing datasets. The agreement between the heat and freshwater fluxes derived from the GO-SHIP A20/A22 sections in 2021 and ERA5 data demonstrates the capability of the box model to reliably estimate fluxes over shorter timeframes. This opens the possibility of filling data gaps between GO-SHIP occupations by leveraging daily-averaged surface datasets such as ERA5. Incorporating these data into the inverse model framework could enable continuous monitoring of heat and freshwater fluxes, which is critical for capturing variability on interannual to decadal scales. Additionally, applying this methodology across multiple hydrographic sections, or integrating satellite-derived datasets and reanalysis products, could provide a more comprehensive understanding of ocean circulation and its role in climate dynamics. For example, combining ERA5-derived surface fluxes with subsurface hydrographic profiles from Argo floats or moored arrays could refine estimates of the vertical structure of transport and fluxes. These approaches would enhance the resolution and applicability of the box model, enabling studies of long-term trends and variability in key regions, such as the western NASG, where consistent results from multiple-box models suggest robustness to aliasing effects. Therefore, while this study confirms the utility of the box model for short-term investigations, its extension to broader spatial and temporal domains represents a valuable direction for advancing oceanographic research.

Chapter 4: Anthropogenic Carbon Trends in the Western NASG

This chapter has been submitted to *Journal of Geophysical Research: Oceans* as:

Santana Toscano, D., Brown, P., Hernández Guerra, A. 2025. Anthropogenic Carbon Dynamics: Concentrations, Transports and Trends in the Western NASG.

4.1. Introduction

The ocean serves as a vital regulator of Earth's climate by absorbing nearly one-third of the CO_2 released into the atmosphere through human activities such as fossil fuel burning and land-use changes (Friedlingstein et al., 2023; Gruber et al., 2019; Khatiwala et al., 2009). This process mitigates the effects of anthropogenic emissions but simultaneously drives significant changes in the marine carbonate system, such as reductions in pH and carbonate ion concentrations ($[CO_3^{2-}]$; Doney et al., 2020; Gattuso et al., 2015). These changes, collectively termed Ocean Acidification (OA), reflect the imbalance created by increasing atmospheric CO_2 levels and have wide-ranging implications for marine ecosystems, biogeochemical cycles, and global climate regulation (Caldeira & Wickett, 2003, 2005; Doney et al., 2009; Orr et al., 2005; Raven et al., 2005). Understanding the ocean's role as a carbon sink, particularly in regions with intense CO_2 uptake like the North Atlantic Ocean, is crucial for predicting the future trajectory of global carbon dynamics (Asselot et al., 2024; Curbelo-Hernández et al., 2024)

The North Atlantic Ocean is recognized as one of the strongest oceanic CO_2 sinks, storing approximately 23–38% of the global anthropogenic carbon (C_{anth}) inventory (Khatiwala et al., 2013; Sabine et al., 2004). This phenomenon is driven by two key mechanisms: the efficient absorption of atmospheric CO_2 in subtropical North Atlantic surface waters, aided by low Revelle factors, and the subsequent poleward transport of these carbon-enriched waters (Brown et al., 2021; Pérez et al., 2013; Sabine et al., 2004). Deep-water formation processes in the subpolar North Atlantic then facilitate the subduction of C_{anth} into the ocean, ensuring its long-term storage (Pérez et al., 2010; Sabine et al., 2004).This intricate interplay between surface uptake, transport, and deep storage positions the North Atlantic as a critical player in the global carbon cycle (Gruber et al., 2019).

Within this larger system, the western North Atlantic Subtropical Gyre (NASG) emerges as a region of particular interest. Characterized by high CO_2 fluxes driven by air-sea disequilibria, this region experiences significant seasonal and interannual variability in C_{anth} uptake (Bonou et al., 2024). Seasonal temperature fluctuations dominate the variability in CO_2 solubility, while biological processes such as photosynthesis and remineralization further modulate the carbon dynamics (Gruber et al., 2019; Raven et al., 2005). Additionally, physical processes such as the strength and variability of the Atlantic Meridional Overturning Circulation (AMOC), along with climatic drivers like the North Atlantic Oscillation (NAO), exert a strong influence on C_{anth} distribution and storage (García-Ibáñez et al., 2016; Pérez et al., 2018). Changes in these processes, whether through natural variability or anthropogenic forcing, can significantly alter the region's capacity to act as a carbon sink (Pérez et al., 2013).

The long-term accumulation of C_{anth} in the ocean has consequences beyond the uptake of atmospheric CO_2. It alters the carbonate chemistry of seawater, increasing the Revelle factor and reducing the buffering capacity of the ocean, thereby making it more sensitive to further CO_2 increases (Caldeira & Wickett, 2003). In the western NASG, this process is of particular concern, as changes in oceanic circulation patterns, deep-water formation, and surface warming could diminish the region's ability to sequester carbon over time. Furthermore, the impacts of OA, such as the shoaling of the aragonite saturation horizon and the subsequent exposure of sensitive marine ecosystems to undersaturated conditions, underscore the urgency of understanding the dynamics of C_{anth} in this region (Feely et al., 2004; Guinotte et al., 2006).

While significant progress has been made in studying the North Atlantic, particularly regarding C_{anth} concentrations and uptake dynamics, there is still much to uncover about the mechanisms governing C_{anth} transport within the region (Caínzos et al., 2022). Emerging technologies, such as Argo-O_2 floats and neural network-based estimation methods, are revolutionizing the study of C_{anth} by providing unprecedented opportunities to examine its fine-scale distribution, temporal evolution, and transport (Asselot et al., 2024). However, traditional methods, including ship-based measurements of the carbonate system and transient tracers like chlorofluorocarbons (CFCs), remain foundational in this work. These methods offer robust, high-quality data essential for understanding C_{anth} dynamics and serve as critical benchmarks for validating and complementing data from modern technologies (Talley et al., 2016). Together, these approaches enable a more comprehensive understanding of C_{anth} variability and transport processes. Understanding the pathways and rates at which C_{anth} is redistributed through ocean circulation and vertical mixing processes (García-Ibáñez et al., 2016; Pérez et al., 2018) requires a shift from a concentration-centric approach to a transport-focused perspective. Such a shift would provide crucial insights into how atmospheric CO_2 uptake integrates with regional and largescale circulation features, including the AMOC, and its impact on long-term carbon storage. Addressing these gaps is essential for fully understanding the western NASG's role in the global carbon cycle and its response to ongoing climate change (Bonou et al., 2024; Doney et al., 2020; Friedlingstein et al., 2023; Li et al., 2024).

This study focuses on the western NASG, aiming to advance our understanding of the mechanisms governing the transport of C_{anth} within this region. By examining the pathways of C_{anth} redistribution through ocean circulation and the influence of regional dynamics such as the Gulf Stream (GS), the Deep Western Boundary Current (DWBC) and regional currents, we seek to provide a more comprehensive view of its role in the carbon cycle. Through the integration of hydrographic observational data and the inverse modeling approach, this work emphasizes the importance of transport processes in shaping C_{anth} variability. These findings are expected to enhance predictions of how changes in circulation and atmospheric CO_2 levels will influence C_{anth} transport, ultimately contributing to strategies for mitigating the impacts of climate change.

4.2. Data and Methods

4.2.1 Hydrographic Data

This study analyzes hydrographic data collected from two meridional sections, A20 (52°W) and A22 (66°W), located in the western NASG (Fig. 4.1). These sections were sampled as part of repeat hydrography surveys conducted in 1997, 2003, 2012, and 2021. Each section intersects key oceanographic features, including major currents such as the GS, the DWBC, the North Brazil Current (NBC), and the North Equatorial Current (NEC). These currents play a critical role in the transport and redistribution of heat, freshwater, and biogeochemical properties across the region, making these sections ideal for studying variability in ocean circulation and C_{anth} transport (Casanova-Masjoan et al., 2018; Joyce et al., 2001; Santana-Toscano et al., 2023, 2025). For this study, we utilized 77, 82, 81, and 90 high-quality stations from the A22 section in 1997, 2003, 2012, and 2021, respectively, and 95, 88, 83, and 90 high-quality stations from the

A20 section for the same years. Sampling for both sections was conducted during boreal summer in 1997, boreal fall in 2003, and boreal spring in 2012 and 2021.

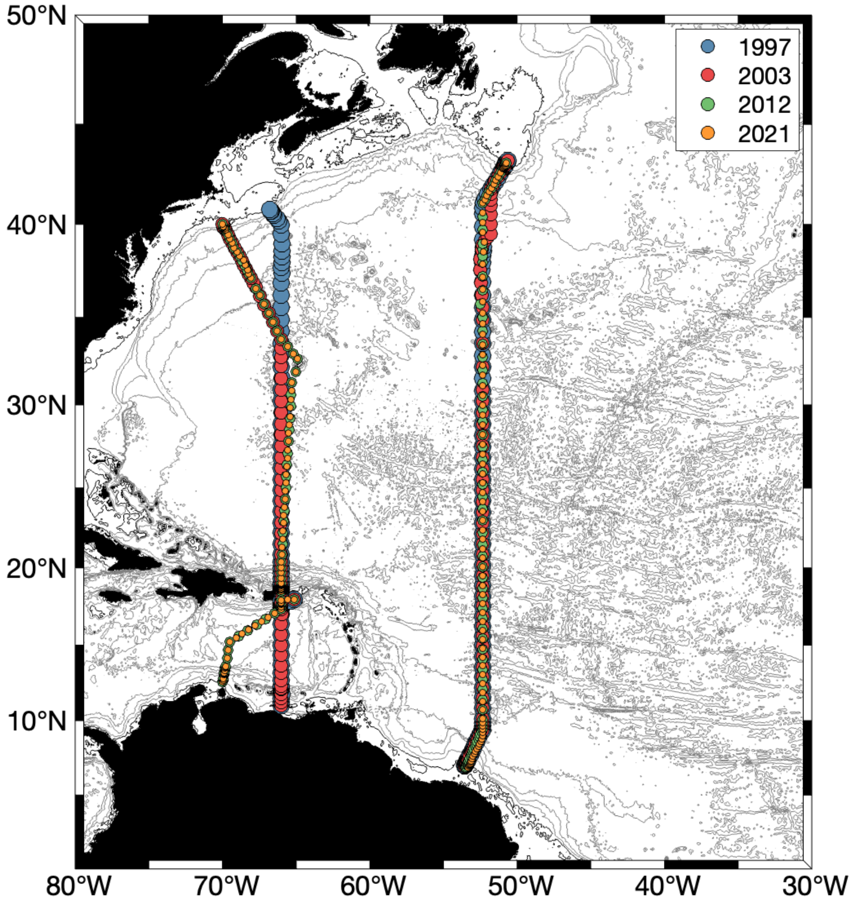

Figure 4.1. Map of the hydrographic sections defining the boundaries of the inverse box model. The A20 section is positioned nominally at 52ºW, while the A22 section lies at 66ºW. Stations sampled during the 1997, 2003, 2012, and 2021 surveys are represented by blue, red, green, and orange dots, respectively, for each section.

The hydrographic data were collected as part of the Global Ocean Ship-Based Hydrographic Investigations Program (GO-SHIP) and are publicly available through the CLIVAR and Carbon Hydrographic Data Office (CCHDO). The data sets include measurements of temperature, salinity, dissolved oxygen, and a suite of biogeochemical variables, such as total alkalinity (AT), dissolved inorganic carbon (CT), and nutrients (nitrate, phosphate, silicate). To facilitate analysis, variables were interpolated onto a uniform grid using a neutral density framework (γ^n; Jackett and McDougall, 1997). This approach aligns water properties along isopycnal surfaces, which better represent the continuity of water masses compared to depth levels. Interpolation was firstly performed every 2 dbar, consistent with the vertical resolution of the CTD casts, using a 2D linear interpolation with Delaunay triangulation for scattered data and nearest extrapolation for missing values.

4.2.2 Atmospheric Data

Wind velocity data used to estimate Ekman transport were obtained from the National Center for Environmental Prediction Reanalysis II (NCEP-DOE) project, provided by the National Oceanic and Atmospheric Administration (NOAA; Kanamitsu et al., 2002). The hourly data were averaged over the duration of each cruise and calculated at a height of 10 meters above sea level. The dataset spanned the area between each section and the American coastline, with a spatial resolution of 2.5º x 2.5º, while maintaining the same latitudinal boundaries as the cruises.

The data on atmospheric CO_2 concentrations used in this study were retrieved from the NOAA Global Monitoring Laboratory (GML) Carbon Cycle Greenhouse Gases (CCGG) database. This dataset provides hourly, daily, and monthly averages of atmospheric CO_2 dry air mole fractions, based on quasi-continuous measurements from multiple locations, including Barrow (Alaska), Mauna Loa (Hawaii), American Samoa, and the South Pole, spanning from 1973 to the present (Thoning et al., 2024).

4.2.3 Geostrophy and Inverse Model

The geostrophic velocity between station pairs was estimated using the thermal wind equation, referencing the neutral density layer of $\gamma^n = 28.14$ kg m^{-3} as the level of no motion. This reference layer lies between the North Atlantic Deep Water (NADW) and the Antarctic Bottom Water (AABW; Table 4.1), which flow in opposite directions (Casanova-Masjoan et al., 2018; Joyce et al., 2001; Santana-Toscano et al., 2023). For station pairs where the seafloor is shallower than this reference level, the closest common depth was used as the reference. The relative geostrophic velocity was then adjusted using ADCP measurements, following the methodology outlined by Comas-Rodríguez et al. (2010) and Santana-Toscano et al. (2023).

This adjustment involved visually comparing the vertical profiles of geostrophic velocities, mean SADCP velocities between station pairs, and mean LADCP velocities for each station. When the ADCP velocity profiles aligned with the geostrophic velocities, an adjustment was performed over a selected depth interval where they matched. However, not all station pairs underwent adjustment due to inconsistencies in the shear between ADCP and geostrophic velocity profiles, leaving some geostrophic velocities unadjusted.

Table 4.1. Neutral density limits for each layer and their associated water masses, with the level of no motion highlighted in bold.

Layer	**Neutral density (γ^n) range**	**Water mass**
1	$\gamma^n < 26.4$	North Atlantic Subtropical Underwater (STUW)
2	$26.4 < \gamma^n < 26.6$	Subtropical Mode Water (STMW)
3	$26.6 < \gamma^n < 27$	Antarctic Intermediate Water (AAIW)
4	$27 < \gamma^n < 27.5$	
5	$27.5 < \gamma^n < 27.7$	
6	$27.7 < \gamma^n < 27.8$	
7	$27.8 < \gamma^n < 27.875$	Labrador Sea Water (LSW)
8	$27.875 < \gamma^n < 27.925$	
9	$27.925 < \gamma^n < 27.975$	
10	$27.975 < \gamma^n < 28$	Iceland-Scotland Overflow Water (ISOW)
11	$28 < \gamma^n < 28.05$	
12	$28.05 < \gamma^n < 28.1$	Denmark Strait Overflow Water (DSOW)
13	$28.1 < \gamma^n <$ **28.14**	

14	**28.14** < γ^n < bot.	Antarctic Bottom Water (AABW)

The initial geostrophic estimation of velocity for each station pair is computed assuming a null velocity at a reference level. However, this level of no motion has a velocity different from zero. Inverse models are used to estimate reference-level velocities for each station pair by applying mass conservation constraints as equations in a matrix form (Ganachaud & Wunsch, 2000; Hernández-Guerra et al., 2019; Wunsch, 1978, 1996):

$$Ab + n = -Y$$

where A is a matrix containing the mass of each layer at station pairs, b is a vector of unknown reference velocities and adjustments to Ekman transport, n is the noise vector, and Y is a vector representing mass transport imbalances in each layer from the relative velocity field. The combination of mass conservation equations and their associated uncertainties forms an underdetermined system, which can be solved using the Gauss-Markov estimator. This method provides an estimate that minimizes the error with the real value based on initial and noise information. Additionally, it quantifies uncertainties in the solution (Wunsch, 1996).

A single-box inverse model was applied independently to each section, A20 and A22, and for each of the years surveyed. This approach has been widely used in previous studies (Arumí-Planas et al., 2023; Caínzos et al., 2023; Casanova-Masjoan et al., 2018; Hall, 2004; Joyce et al., 2001; Santana-Toscano et al., 2023). The single-box models consist of 14 mass conservation equations, corresponding to 14 neutral density layers spanning the water column (Table 4.1). Additionally, an overall mass conservation equation was included for the entire water column. Unknowns in the inverse model were solved using the Gauss-Markov method, minimizing error variances while requiring a priori variances for both velocities and equations. Following Santana-Toscano et al., 2025, a priori velocity variances of $(0.03 \text{ m s}^{-1})^2$ were used for station pairs with ADCP adjustments, and higher variances of $(0.06 \text{ m s}^{-1})^2$ were applied to unadjusted pairs. A priori equation variances were set at $(2 \text{ Sv})^2$ for surface layers and $(1 \text{ Sv})^2$ for deeper layers and overall mass conservation.

4.2.4 C_{anth} Estimations

The concentration of C_{anth} cannot be directly measured in the ocean and is instead inferred from other water sample parameters using methods that assume a steady-state ocean. Among these, back-calculation techniques, such as ΔC* (Gruber et al., 1996), tracer combining oxygen, inorganic carbon and total alkalinity (TrOCA); (Touratier et al., 2007), and φC_T^0 (Pérez et al., 2008; Vázquez-Rodríguez et al., 2009) are widely used, alongside approaches based on transit time distributions (Waugh et al., 2006). Here, the φC_T^0 back-calculation method is used to estimate the preformed dissolved inorganic carbon concentration of a water sample when it last interacted with the surface. This method uses variables such as total alkalinity (AT), oxygen utilization, salinity, and temperature, while accounting for temporal variations in CO_2 air-sea disequilibrium. Its ability to handle regions with strong mixing processes makes it an improvement over the ΔC* method (Caínzos et al., 2022; Matear et al., 2003; Thomas & Ittekkot, 2001). The C_{anth} concentration (µmol/kg) distribution along the A20 (Fig. 4.2a–d) and A22 (Fig. 4.2e–h) hydrographic sections demonstrates a clear increase over the past four decades, observed across all depths.

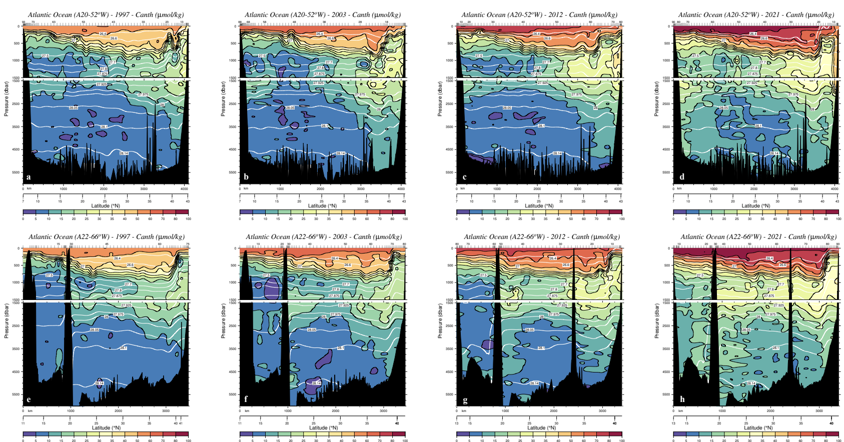

Figure 4.2. Vertical sections of C_{anth} concentration (µmol/kg) at A20 (52ºW; a–d) and A22 (66ºW; e–h) with neutral density (γ^n, kg m^{-3}) shown as white contours.

The transport of C_{anth} was evaluated across the western NASG by combining biogeochemical data with geostrophic velocity estimates derived from inverse models. The transport of any property (T) is calculated for each pair of consecutive hydrographic stations and between two neutral density interphases using the following equation (Caínzos et al., 2022):

$$T = \iint C\rho v dy d\gamma^n$$

where C represents the concentration of the property, ρ is the in situ density, v is the geostrophic velocity from the inverse model perpendicular to the section, and $dyd\gamma^n$ refers to the area over which the computation is performed, taking into account the distance between stations and the 'vertical extent of each vertical layer, respectively.

4.3. Results

Figure 4.3 depicts the C_{anth} transport (kmol/s) by water mass for the A20 (a, b) and A22 (c–e) sections, divided to reflect distinct regional dynamics. Positive values of zonal transport correspond to eastward fluxes, while negative values indicate westward fluxes. Below 28ºN (panels a and d), surface and intermediate layer transport is predominantly westward, driven by currents like the NBC, NEC, and Antilles Current (Casanova-Masjoan et al., 2018; Santana-Toscano et al., 2023). Above 28ºN (panels b and e), the eastward C_{anth} transport is dominated by the GS, which exhibits significantly higher net transport in surface and intermediate layers due to its greater intensity compared to the westward currents (Santana-Toscano et al., 2023). Panel c focuses on the Caribbean Sea, where the C_{anth} transport reflects the typical westward mass transport of the region (Casanova-Masjoan et al., 2018; Joyce et al., 2001). Across all panels, the deep and bottom layers show much weaker C_{anth} transport than the surface and intermediate layers, consistent with the lower C_{anth} concentrations at these depths (Fig. 4.2). However, features such as the DWBC are evident, with slight eastward transport in the deep layers of panels a and d and westward transport in panels b and e. Despite seasonal variability in the surveyed years (blue: 1997, red: 2003, green: 2012, orange: 2021), an overall increasing trend is evident in the surface and intermediate layers across all panels.

Figure 4.4 illustrates the northward accumulated C_{anth} transport for each water mass, section, and surveyed year, using the same color scheme as in Figure 4.3. For the A20 (Fig. 4.4.a–g) and A22 (Fig. 4.4.h–n) sections, water masses are arranged from the shallowest on the left to the deepest on the right. The accumulated C_{anth} transport closely mirrors the mass transport distribution in the region (Casanova-Masjoan et al., 2018; Santana-Toscano et al., 2023), particularly where C_{anth} concentrations are highest—namely in the STUW and STMW layers. In panels a–b and h–i, the transport exhibits a gradual westward trend from the southernmost latitude up to 33ºN, where the slope increases sharply, signaling a much stronger westward flow, which is the GS recirculation (GSR). Beyond the GSR, at 37.5ºN, the GS emerges as a robust eastward jet, maintaining consistent C_{anth} transport up to the northernmost latitude (Casanova-Masjoan et al., 2018; Santana-Toscano et al., 2023). Other water masses, however, show less pronounced C_{anth} transport, with variations in x-axis scaling between shallower and intermediate panels. For example, the AAIW and LSW layers (Fig. 4.4.c, j, k, and d) display a highly variable distribution across latitudes. These layers generally exhibit a net eastward C_{anth} transport at lower latitudes in most surveys and sections, followed by the characteristic westward and eastward transport transitions associated with the GSR and GS, respectively. As the analysis moves to deeper layers, distinct patterns emerge. The ISOW layer lacks a significant C_{anth} transport signal, while the DSOW layer exhibits a similar eastward-to-westward transport pattern observed in shallower layers, though this is inconsistent across surveys. Finally, the AABW layer presents the weakest C_{anth} transport among all layers, remaining nearly zero in most cases.

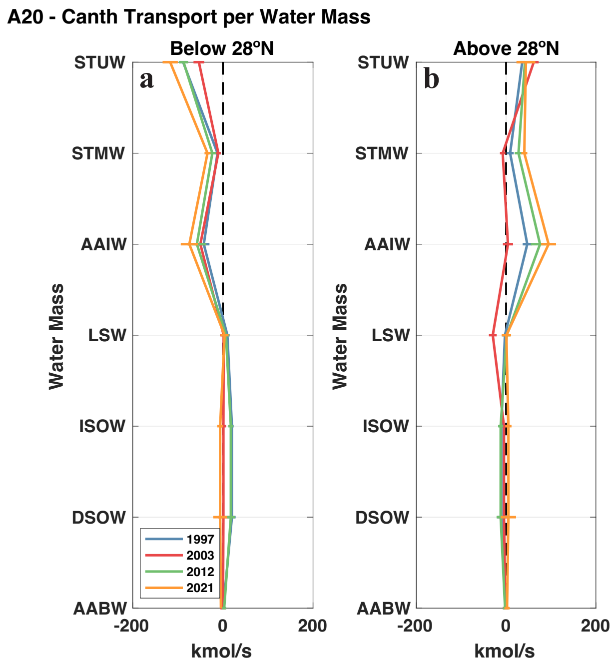

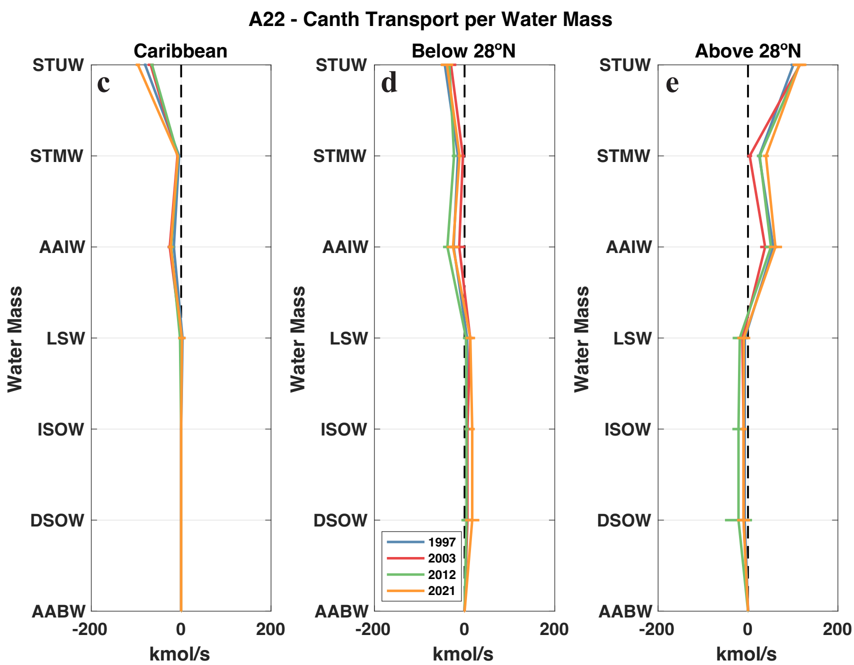

Figure 4.3. Vertical distribution of C_{anth} transport (kmol/s) by water mass and year, with 1997, 2003, 2012, and 2021 represented by blue,

red, green, and orange lines, respectively. Panels a and b show the A20 section (52ºW), while panels c to e depict the A22 section (66ºW). The figure highlights three distinct dynamical regions within the western NASG: the Caribbean Sea (c), the southern regions (a, c), and the northern regions (b, e), separated by the 28ºN latitude.

Figures 4.3 and 4.4 illustrate a net increase in C_{anth} transport over time. To investigate the factors contributing to this increase, we analyzed how much is driven by the rise in C_{anth} concentration versus the variability in mass transport within the region. A linear regression was performed between C_{anth} transport and mass transport, and the results are presented in Figure 4.5. This figure displays the slope of the linear trend for each water mass over the years surveyed in the A22 (a) and A20 (b) sections. As expected, the most significant growth in C_{anth} transport over time is observed in the surface and intermediate layers. In the STUW layer, C_{anth} transport increased from approximately 50 to 75 µmol/kg between 1997 and 2021, followed by the immediately deeper STMW layer, which grew from roughly 28 to 43 µmol/kg. For deeper water masses, signals were separated into northern and southern regions, as these masses are not present throughout the entire basin, and including all latitudes would underrepresent regional differences. Among the three deeper water masses (LSW, ISOW, and DSOW), a pronounced change is evident when comparing northern and southern signals. Both the northern and southern LSW signals show consistent growth over the years, with similar values observed in both the A22 and A20 sections. Meanwhile, ISOW and DSOW exhibit higher variability, particularly in the A22 section, but they maintain the previously noted dominance of northern over southern rates of C_{anth} transport change. The overall trend of increasing C_{anth} transport across all water masses over the years indicates that this rise is primarily driven by the increase in C_{anth} concentration rather than by changes in mass transport within the region.

After identifying the increase in C_{anth} concentration as the primary driver of the rise in C_{anth} transport over the years in the western NASG, a critical question arises: Is the western NASG, along with the surrounding areas, absorbing CO_2 from the atmosphere at a rate sufficient to keep up with the rapid increase in atmospheric CO_2? To explore this, we examined the temporal trends of atmospheric CO_2 concentrations at four key monitoring stations—Barrow, Alaska (BRW); Mauna Loa, Hawaii (MLO); American Samoa (SMO); and the South Pole (SPO)—as well as the mean atmospheric CO_2 concentration derived from these stations. Figure 4.6 presents these trends, alongside the temporal trends of mean oceanic C_{anth} concentrations observed in the A20 and A22 sections during the surveyed years. The individual monitoring stations exhibit a consistent upward trajectory in atmospheric CO_2 from 1970 to 2025 (Figure 4.6a-d). Despite geographic differences, the trends across stations are remarkably similar, indicating a globally uniform increase in atmospheric CO_2 concentrations over time. The mean oceanic C_{anth} concentration in the A20 and A22 sections closely mirrors the upward trend of atmospheric CO_2 (Figure 4.6e). While the fitted trends for both atmospheric CO_2 and oceanic C_{anth} concentrations are similar, subtle differences may suggest variability in the region's ability to absorb atmospheric CO_2. These differences could arise from factors such as ocean circulation, temperature variability, and water mass dynamics, which influence the efficiency of CO_2 uptake in the region. The resemblance between atmospheric CO_2 and C_{anth} concentration trends implies that the western NASG is effectively capturing a portion of the increased atmospheric CO_2. However, as atmospheric CO_2 levels continue to rise, it is crucial to assess whether the region's capacity to sequester CO_2 remains proportional to these increases. Monitoring stations located across diverse latitudes, from the Arctic to the Antarctic, emphasize the global nature of atmospheric CO_2 trends and suggest that the observations in the NASG reflect broader global processes rather than isolated regional phenomena.

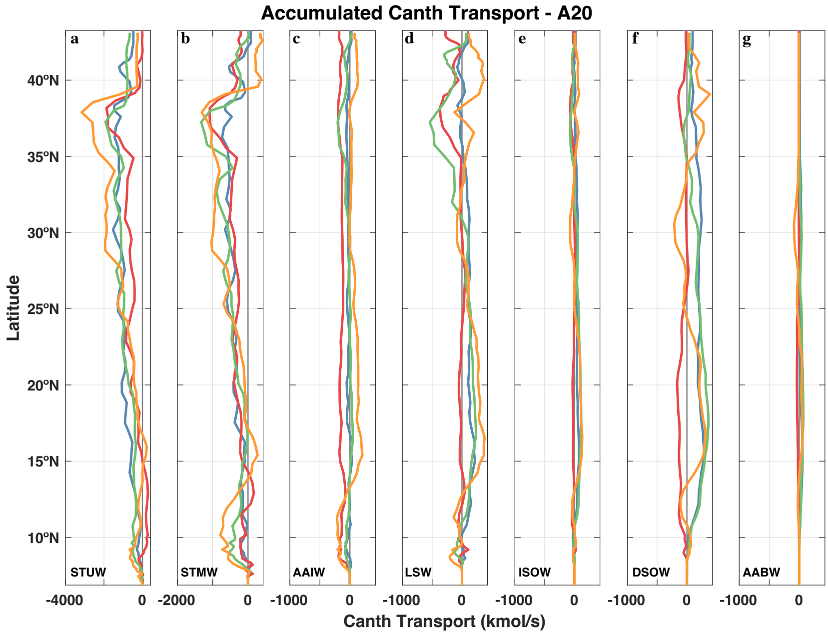

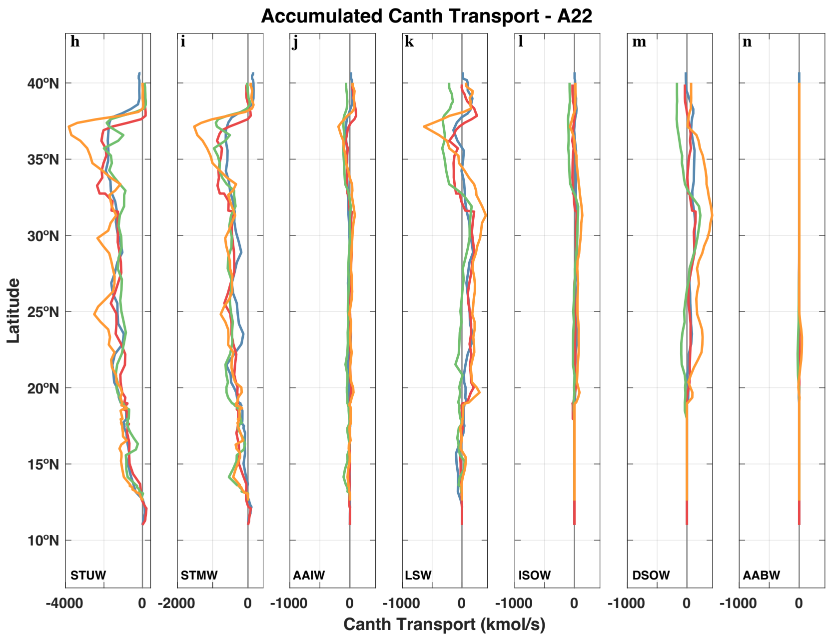

Figure 4.4. Northward accumulated C_{anth} transport (kmol/s) for each water mass, section, and surveyed year, with colors corresponding to those in Figure 4.3. Panels a–g represent the A20 section (52ºW), and panels h–n represent the A22 section (66ºW). Water masses are

arranged from the shallowest on the left to the deepest on the right. X-axis vary between subplots.

4.4. Discussion

The findings of this study highlight the dominance of surface and intermediate layers in driving C_{anth} transport in the western NASG, particularly within the STUW and STMW layers. Similarly, Asselot et al. (2024) identify the upper subtropical waters and Subpolar Mode Water (SPMW) as key pathways for C_{anth} penetration, with vertical homogenization facilitated by winter convection. The consistent upward trends in C_{anth} concentrations across surface layers reflect the strong linkage between air-sea CO_2 fluxes and oceanic uptake, as reported in both studies. However, the stratified nature of the subtropical NASG likely contributes to differences in the vertical mixing and storage efficiency of C_{anth} compared to the Subpolar North Atlantic (SPNA), where deeper winter convection allows for more pronounced C_{anth} penetration into intermediate and deep layers. This work underscores the role of the GS and its recirculation in influencing C_{anth} transport patterns in the western NASG, particularly through its eastward flow in surface and intermediate layers. While the GS plays an important role in modulating C_{anth} distribution in the subtropical region, the North Atlantic Current (NAC) emerges as a critical link, carrying C_{anth}-rich waters from the subtropics into the SPNA. The NAC facilitates the transformation of these waters into SPMW and LSW through deep convection processes in the subpolar gyre (Asselot et al., 2024; Pérez et al., 2008; Vázquez-Rodríguez et al., 2009). The variability of C_{anth} transport in deep layers, including the ISOW and DSOW, as observed in this study, aligns with Asselot et al.'s (2024) findings regarding the stepwise deepening of C_{anth} within the SPNA. However, while deep water formation and convection drive significant C_{anth} trapping in the SPNA, the weaker signals observed in the NASG may be attributed to the role of deep water mass circulating great distances from its origin regions until this region, in contrast to the SPNA as a source of C_{anth}. The DSOW's intermittent eastward and westward transport patterns in this study also suggest a more variable influence of deep boundary currents compared to the consistent deep transport pathways identified in the SPNA (Asselot et al., 2024).

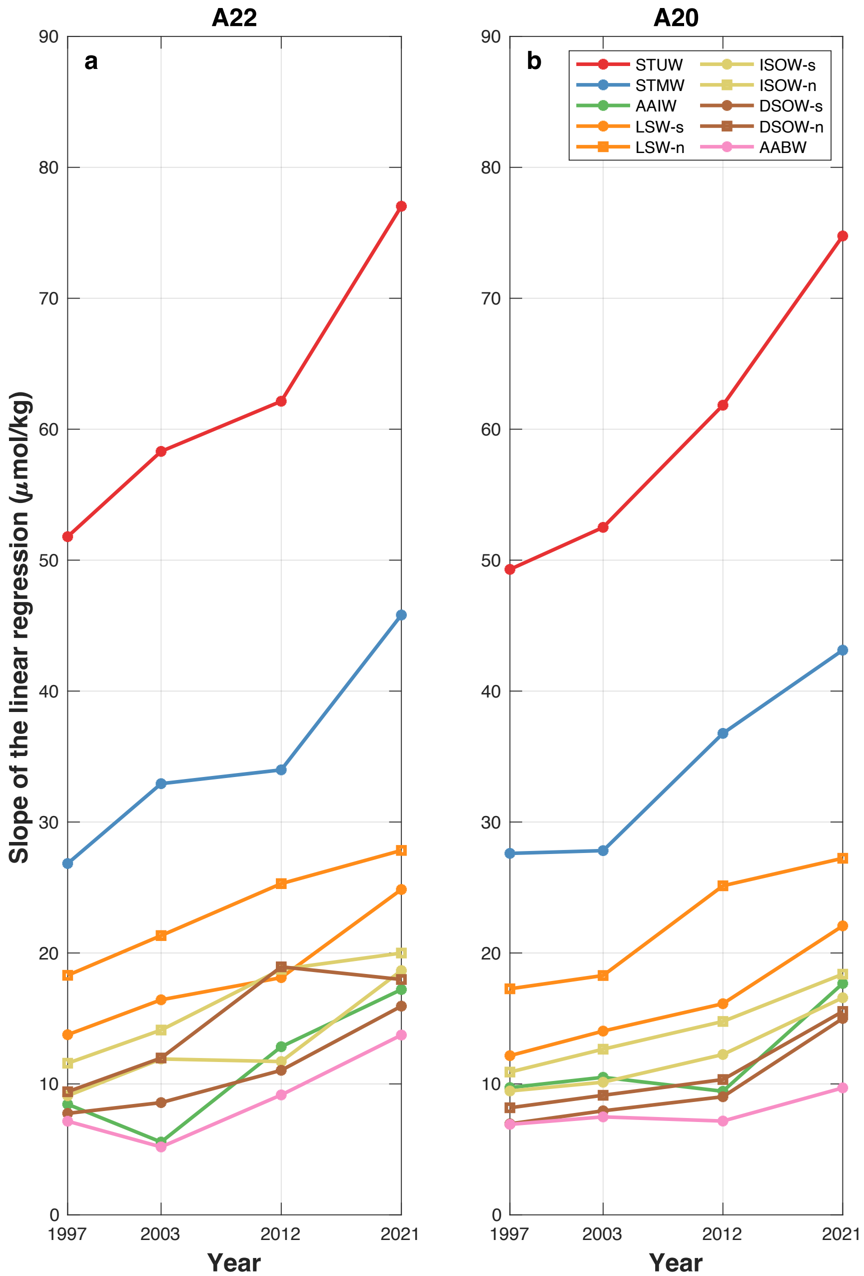

Figure 4.5. Slope of the linear regression (μmol/kg) between C_{anth} transport (kmol/s) and mass transport (Sv) for each water mass over the surveyed years (1997, 2003, 2012, and 2021) in the A22 (a) and

A20 (b) sections. The analysis separates water masses into northern (n) and southern (s) signals for deeper masses. The color scheme represents different water masses: STUW (red), STMW (blue), AAIW (green), LSW (orange), ISOW (yellow), DSOW (brown) and AABW (magenta).

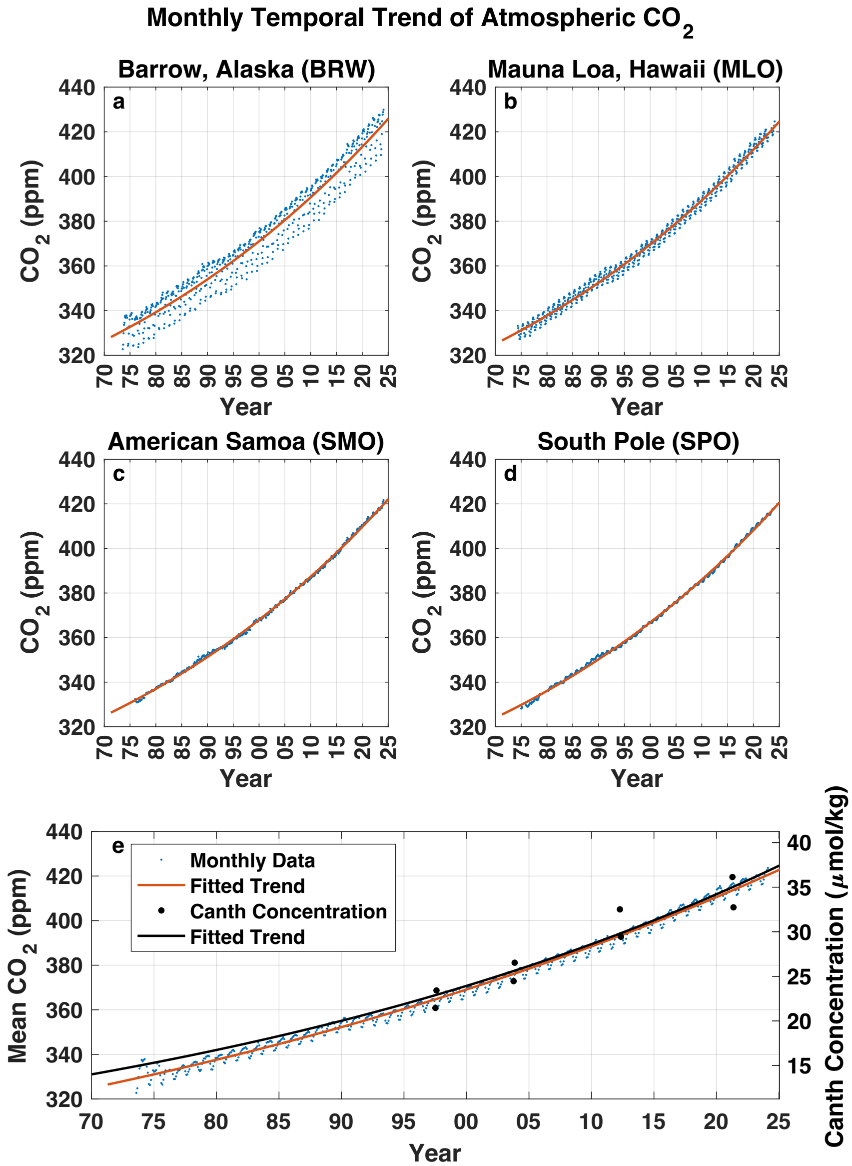

Figure 4.6. Temporal trends of atmospheric CO_2 concentrations (ppm) and oceanic C_{anth} concentrations (mol/kg) from 1970 to 2025.

Panels a–d show the atmospheric CO_2 concentrations recorded at four monitoring stations: Barrow, Alaska (BRW; a), Mauna Loa, Hawaii (MLO; b), American Samoa (SMO; c), and the South Pole (SPO; d). Panel e displays the mean atmospheric CO_2 concentration derived from these stations (blue dots and red fitted trend) alongside the mean C_{anth} concentration from the A20 and A22 sections (black dots and black fitted trend).

Bonou et al. (2024) documented consistent increases in CO_2 parameters, such as pCO_2 and TCO_2, across the tropical Atlantic from 1985 to 2022, largely driven by rising atmospheric CO_2 levels. While their analysis highlights basin-wide trends, similar results (increasing in CO_2 concentration, C_{anth} concentration and also C_{anth} transport) presented here focus on the western NASG, therefore serving as validating part of the broader vision shown in their work. Bonou et al. (2024) attribute seasonal peaks in pCO_2 and TCO_2 to upwelling and biological activity, particularly during boreal spring and summer. Similarly, this study observes seasonal elevations in C_{anth} transport, but these are modulated latitudinally by the regional currents occurring and/or crossing the region (NBC, NEC, GS, DWBC).

Brown et al. (2021) explored the relationship between the AMOC and C_{anth} transport, emphasizing the impact of AMOC strength on northward transport. They found that a weakening AMOC reduced C_{anth} transport, which was partly mitigated by increasing surface C_{anth} concentrations. Similarly, this study highlights the predominant role of regional currents like the GS and DWBC, which are branches of the AMOC, in shaping C_{anth} transport patterns in the western NASG. A notable aspect shared by both studies is the significant variability in C_{anth} transport. Brown et al. (2021) observed interannual fluctuations tied to AMOC variability, while this study documents variations across surveyed years from the last 4 decades in the NASG. In both cases, surface and intermediate layers show the strongest transport trends. This reflects the sensitivity of C_{anth} transport to circulation dynamics and the pivotal role of upper-layer processes in redistributing C_{anth}-rich waters. Deep and bottom layers are addressed differently in the two studies but reveal complementary findings. Brown et al. (2021) emphasize the role of the AMOC's deep limb in transporting C_{anth} southward and facilitating its long-term sequestration in the deep ocean. This aligns with the results of this study, where weaker C_{anth} transport signals in deeper water masses, such as LSW, ISOW and DSOW, reflect limited concentrations and localized transport dynamics.

The results of this study can be contextualized alongside those of Pérez et al. (2018), which emphasize the role of the AMOC in the transport and storage of C_{anth} in the North Atlantic. In the NASG, this study identifies increasing trends in C_{anth} transport in surface and intermediate layers, primarily driven by rising atmospheric CO_2 concentrations and mediated by currents such as the GS and DWBC. Similarly, Pérez et al. (2018) demonstrate that the upper limb of the AMOC plays a critical role in delivering C_{anth} to the SPNA. Their findings show that AMOC-driven transport has led to a persistent increase in C_{anth} concentrations in SPMW and deeper layers, consistent with the upward trajectory observed in this study for northern regions. Another parallel lies in the recognition of vertical stratification's role in modulating C_{anth} transport. This study finds weaker C_{anth} transport signals in deeper layers of the NASG, consistent with the lower concentrations observed in LSW, ISOW and DSOW. Pérez et al. (2018) expand on this by linking the transport of acidified waters in the lower AMOC limb to significant shoaling of the ASH, which threatens cold-water coral ecosystems. Both studies highlight the vulnerability of deeper water masses to anthropogenic perturbations, though with a greater emphasis on ecological impacts in Pérez et al. (2018). Finally, both works address the interplay between C_{anth} transport and long-term changes in atmospheric CO_2. Pérez et al. (2018) estimate that doubling atmospheric CO_2 levels would severely exacerbate ocean acidification, reducing carbonate availability by up to 79% in preindustrial levels. This projection complements this study's findings, which suggest that rising C_{anth} concentrations are a major driver of increased transport across all water masses in the NASG.

Chapter 5: Conclusions

- The analyses across the three studies reveal that the main currents of the Atlantic circulation exhibit significant seasonal and interannual variability. The NBC, NEC, GS system, and DWBC show mass transport estimates that align with previous research, though interannual differences—particularly in the NEC and GS—emphasize the influence of variable forcing mechanisms.

- Comparisons between observational data and ocean model outputs indicate that reanalysis products such as GLORYS, with their finer spatial resolution and data assimilation, best capture these transport features, while models like MOM and ECCO yield differing estimates due to their distinct configurations.

- Heat flux estimates indicate a persistent net export of heat from the ocean to the atmosphere, with trends pointing toward increasing heat loss over time. In contrast, freshwater fluxes generally reflect a net gain, with precipitation and runoff exceeding evaporation, although near-zero flux values during some periods suggest minimal net divergence or convergence across the studied sections.

- The use of inverse box models in these studies enables a clear characterization of mass transports in key AMOC components, such as the GS and DWBC, using seasonal hydrographic data. This approach effectively demonstrates the spatial and temporal evolution of these currents, complementing detailed observational analyses from moorings.

- Finally, the analysis of C_{anth} transport in the western NASG shows that the surface and intermediate layers are the predominant drivers of its distribution, with the GS system playing a central role. Rising atmospheric CO_2 levels have led to increasing C_{anth} concentrations and transport, highlighting the strong connection between air–sea CO_2 fluxes and oceanic uptake. The stratified nature of the region results in pronounced transport signals in the upper layers, while deeper water masses exhibit weaker signals, reflecting differences in vertical mixing and storage efficiency.

Appendix A: Data Availability

Hydrographic data were obtained from the CCHDO website as part of the International WOCE and GO-SHIP project databases. The datasets for the A20 cruises (1997, 2003, 2012, and 2021) are accessible at the following links: 1997, 2003, 2012, and 2021. Similarly, the datasets for the A22 cruises (1997, 2003, 2012, and 2021) can be found here: 1997, 2003, 2012, and 2021. Wind velocity data were sourced from the NCEP-DOE Reanalysis II project, provided by NOAA, and are available at NCEP-DOE Reanalysis II. Atmospheric CO_2 concentration data were retrieved from the NOAA GML CCGG database, accessible at NOAA GML CCGG. Matlab code for C_{anth} estimation using the PHI-CT0 method is available for download at C_{anth} PHI-CT0 Toolbox.

Appendix B: Three-Box Inverse Model

The absolute geostrophic velocity (u_a) for a given station pair, as a function of pressure p, is the sum of a relative velocity (u) and the velocity at the reference level (b):

$$u_a(p) = u(p) + b$$

The inverse model finds the optimal solution for b for each station pair. First, we apply mass conservation for the entire water column:

$$\iint \rho u_a dS = 0$$

$$\iint \rho(u + b) dS = 0$$

$$\sum_{j=1}^{N} \sum_{q=1}^{Q} \rho_{jq}(u_{jq} + b_j) a_{jq} = 0$$

where the area integral dS is over the entire area of the section, and in the differential version, area is a_{jq} for each station pair j and isoneutral layer q. The term $\rho_{jq} u_{jq}$ is first summed over each 2 dbar interval within layer q. Due to noise from eddies, internal waves, aliasing, measurements errors and other sources of error, total mass conservation is not exact:

$$\sum_{j=1}^{N}\sum_{q=1}^{Q}\rho_{jq}u_{jq}a_{jq} + \sum_{j=1}^{N}\sum_{q=1}^{Q}\rho_{jq}b_{j}a_{jq} = n_{total}$$

where n_{total} is the noise.

Considering mass conservation in each layer q, we have the following equations:

$$\sum_{j=1}^{N}\rho_{jq}b_{j}a_{jq} + n_{q} = -\sum_{j=1}^{N}\rho_{jq}u_{jq}a_{jq}$$

where n_q is the layer noise.

This equation can be developed according to boxes 1, 2 and 3 (Table 3):

Box 1: A20-Continent

Layers 1-14 (Equations 1-14):

$$\rho_{jq}b_{j}a_{jq} + n_{q} = -\sum_{j=1}^{89}\rho_{jq}u_{jq}a_{jq} \qquad ,j = 1{:}89, q = 1{:}14$$

Overall (Equation 15):

$$\sum_{q=1}^{14}\rho_{jq}b_{j}a_{jq} + n_{q} = -\sum_{q=1}^{14}\sum_{j=1}^{89}\rho_{jq}u_{jq}a_{jq} \qquad ,j = 1{:}89, q = 15$$

Box 2: A22-Continent

Layers 1-7 (Equations 16-22):

$$\rho_{jq}b_{j}a_{jq} + n_{q} = -\sum_{j=90}^{175}\rho_{jq}u_{jq}a_{jq} \qquad ,j = 90{:}175, q = 16{:}22$$

Caribbean (Layers 8-9, Equations 23-24):

$$\rho_{jq}b_j a_{jq} + n_q = -\sum_{j=90}^{118} \rho_{jq}u_{jq}a_{jq} \qquad ,j = 90{:}\,118, q = 23{:}\,24$$

Atlantic (Layers 8-14, Equations 25-31):

$$\rho_{jq}b_j a_{jq} + n_q = -\sum_{j=119}^{175} \rho_{jq}u_{jq}a_{jq} \qquad ,j = 119{:}\,175, q = 25{:}\,31$$

Sum of Layers 1-7 and 8-14 (Atlantic) (Equation 32):

$$\sum_{q=1}^{14} \rho_{jq}b_j a_{jq} + n_q = -\sum_{q=1}^{14}\sum_{j=90}^{175} \rho_{jq}u_{jq}a_{jq} \qquad ,j = 90{:}\,175, q = 32$$

Sum of Caribbean Layers 8-9 (Equation 33):

$$\sum_{q=8}^{9} \rho_{jq}b_j a_{jq} + n_q = -\sum_{q=8}^{9}\sum_{j=90}^{118} \rho_{jq}u_{jq}a_{jq} \qquad ,j = 90{:}\,118, q = 33$$

Sum of Atlantic Layers 8-14 (Equation 34):

$$\sum_{q=8}^{14} \rho_{jq}b_j a_{jq} + n_q = -\sum_{q=8}^{14}\sum_{j=119}^{175} \rho_{jq}u_{jq}a_{jq} \qquad ,j = 119{:}\,175, q = 34$$

Box 3: A20-A22

Layers 1-7 (Equations 35-41):

$$\rho_{jq}b_j a_{jq} + n_q = -\sum_{j=1}^{89} \rho_{jq}u_{jq}a_{jq} \qquad ,j = 1{:}\,89, q = 35{:}\,41$$

Atlantic, Layers 8-14 (Equations 42-48):

$$\rho_{jq} b_j a_{jq} + n_q = -\sum_{j=119}^{175} \rho_{jq} u_{jq} a_{jq} \qquad , j = 119{:}\,175, q = 42{:}\,48$$

Overall (Equation 49):

$$\sum_{q=1}^{14} \rho_{jq} b_j a_{jq} + n_q = -\sum_{q=1}^{14} \sum_{j=1}^{175} \rho_{jq} u_{jq} a_{jq} \qquad , j = 1{:}\,175, q = 49$$

Next, the general equation is written as:

$$\sum_{j=1}^{N} e_{jq} b_j + n_q = -y_q$$

where:

$e_{jq} = \rho_{jq} a_{jq}$

$y_q = \sum_{j=1}^{N} \rho_{jq} u_{jq} a_{jq}$

The matrix equation is rewritten as:

Ab + n = -Y

where **b** is a N x 1 vector of the unknowns (reference velocities and adjustment of the Ekman transport), **A** is a (Q + 1) x N matrix, **n** is a (Q + 1) x 1 vector, and **Y** is a (Q + 1) x 1 vector of values calculated from the CTD data. (Q is for the equations for each layer and the +1 is the equation for conservation of the whole water column.)

The Ekman transport is included in the first layer, leading to the following system:

$$\begin{pmatrix} e_{11} & \cdots & e_{1n} & 1 \\ e_{21} & & e_{2n} & 0 \\ \vdots & \ddots & \vdots & \vdots \\ e_{q,1} & & e_{q,n} & 0 \\ e_{q+1,1} & \cdots & e_{q+1,n} & 1 \end{pmatrix} \begin{pmatrix} b_1 \\ \vdots \\ b_n \\ \Delta T_{Ek} \end{pmatrix} = \begin{pmatrix} y_1 + T_{Ek} \\ y_2 \\ \vdots \\ y_q \\ y_{q+1} + T_{Ek} \end{pmatrix}$$

To solve this matrix, the Gauss-Markov estimator is applied (Wunsch, 1996), as in Hernández-Guerra & Talley (2016):

The idea behind the Gauss-Markov estimator is to choose, among all possible solutions of the system, the one that deviates the least from the real solution. The deviation of the estimate (x̃) from the solution (x) will be given by:

$$P = \langle (\bar{x} - x)\left((\bar{x} - x)\right)^T \rangle$$

a matrix whose main diagonal is intended to be minimized.

We will assume that we know the first and second-order moments as:

$$\langle x \rangle = x_0$$

$$\langle xx^T \rangle = R_{xx}$$

$$\langle n \rangle = 0$$

$$\langle nn^T \rangle = R_{nn}$$

Therefore, the solution we find must be expressed in terms of this a priori known information: R_{xx} and R_{nn}.

The inverse model of this work is linear, so between the estimator of the solution and the observations there is a relationship of the type

$$\bar{x} = By$$

This allows us to apply the Gauss-Markov theorem to find the values of B that minimize the deviation between $\bar{x}$ and x. After mathematical operations, $\bar{x}$ and P can be expressed as:

$$\tilde{x} = R_{xx}A^T(AR_{xx} + R_{nn})^{-1}y$$

$$P = R_{xx} - R_{xx}A^T(AR_{xx} + R_{nn})^{-1}AR_{xx}$$

expressions which allow us to estimate the solution of the equation system and its uncertainty from the a priori information. Using the estimated value of the solution, an estimate for the noise and its uncertainty can also be obtained:

$$\tilde{n} = (I - AR_{xx}A^T(AR_{xx} + R_{nn})^{-1})y$$

$$P_{nn} = APA^T$$

Appendix C: Resumen en Castellano

El Giro Subtropical del Atlántico Norte (NASG, por sus siglas en inglés) desempeña un papel clave en la circulación oceánica a gran escala y en la regulación del clima, especialmente debido a su conexión con la Circulación de Vuelco Meridional del Atlántico (AMOC). Esta tesis estudia la dinámica física y biogeoquímica del oeste del NASG, centrándose en la circulación de este a oeste, el transporte de calor y agua dulce, y las tendencias del carbono antropogénico (Canth). Para ello, se utilizan datos oceanográficos de las secciones A20 y A22, recopilados en los años 1997, 2003, 2012 y 2021, en combinación con técnicas de modelado inverso de caja. Una de las principales innovaciones metodológicas es el uso de un modelo inverso de tres cajas, que mejora los enfoques tradicionales de una sola caja al incorporar más restricciones observacionales. Esto permite estimaciones más precisas del transporte de masas de agua y su variabilidad a lo largo de décadas. Los resultados se comparan con modelos numéricos como GLORYS, ECCO y MOM para evaluar qué tan bien reproducen los patrones de transporte observados. Se encontró que, aunque corrientes como la Corriente del Golfo (GS) y la Corriente de Contorno Profunda del Oeste (DWBC) varían a nivel estacional y de año en año, su transporte promedio a largo plazo es consistente con estudios previos. Esto refuerza la fiabilidad del método de modelado inverso. La GS es el principal transportador de calor y agua dulce hacia el norte, mientras que la DWBC lleva aguas densas hacia el sur, formando la rama inferior de la AMOC. Las estimaciones de flujo de calor indican que en la sección A20 hay una transferencia neta de calor del océano a la atmósfera, con variaciones entre los distintos años de muestreo debido a la influencia de la atmósfera. En cuanto al agua dulce, los datos sugieren que con el tiempo ha habido un aumento en la precipitación y el aporte de agua continental en comparación con la evaporación, una tendencia que también se observa en productos de reanálisis. Además de la circulación oceánica, la tesis analiza cómo el oeste del NASG contribuye a la absorción y transporte de carbono generado por la actividad humana. Los resultados muestran que la GS y la Corriente del Atlántico Norte son clave para mover aguas ricas en carbono desde las regiones subtropicales hasta las subpolares, ayudando a la captura y almacenamiento de CO_2 atmosférico a largo plazo. Sin embargo, el aumento de CO_2 también está relacionado con una mayor acidificación del océano, lo que se refleja en la disminución de la concentración de iones carbonato y en el ascenso de la "frontera de saturación" del aragonito en la región. El monitoreo continuo y en alta resolución es esencial para seguir estos cambios y mejorar las predicciones sobre la interacción entre el océano y el clima en el futuro.

Bibliography

Adcroft, A., Anderson, W., Balaji, V., Blanton, C., Bushuk, M., Dufour, C. O., et al. (2019). The GFDL Global Ocean and Sea Ice Model OM4.0: Model Description and Simulation Features. Journal of Advances in Modeling Earth Systems, 11(10), 3167–3211. https://doi.org/10.1029/2019MS001726

Alexander-Astiz Le Bras, I., Sonnewald, M., & Toole, J. M. (2019). A Barotropic Vorticity Budget for the Subtropical North Atlantic Based on Observations. Journal of Physical Oceanography, 49(11), 2781–2797. https://doi.org/10.1175/JPO-D-19-0111.1

Andres, M., Donohue, K. A., & Toole, J. M. (2020). The Gulf Stream's path and time-averaged velocity structure and transport at 68.5°W and 70.3°W. Deep Sea Research Part I: Oceanographic Research Papers, 156, 103179. https://doi.org/10.1016/j.dsr.2019.103179

Arumí-Planas, C., Pérez-Hernández, M. D., Pelegrí, J. L., Vélez-Belchí, P., Emelianov, M., Caínzos, V., et al. (2023). The South Atlantic Circulation Between 34.5°S, 24°S and Above the Mid-Atlantic Ridge From an Inverse Box Model. Journal of Geophysical Research: Oceans, 128(5), e2022JC019614. https://doi.org/10.1029/2022JC019614

Asselot, R., Carracedo, L. I., Thierry, V., Mercier, H., Bajon, R., & Pérez, F. F. (2024). Anthropogenic carbon pathways towards the North Atlantic interior revealed by Argo-O2, neural networks and back-calculations. Nature Communications, 15(1), 1630. https://doi.org/10.1038/s41467-024-46074-5

Asselot, R., Thierry, V., Carracedo, L. I., Mercier, H., Velo, A., Bajon, R., & Pérez, F. F. (2024, October 15). Temporal evolution of anthropogenic carbon in the subpolar North Atlantic gyre between 2011 - 2021. Authorea Preprints. Authorea. https://doi.org/10.22541/essoar.172901267.76656819/v1

Biló, T. C., & Johns, W. E. (2019). Interior Pathways of Labrador Sea Water in the North Atlantic From the Argo Perspective. Geophysical Research Letters, 46(6), 3340–3348. https://doi.org/10.1029/2018GL081439

Biló, Tiago Carrilho, & Johns, W. E. (2020). The Deep Western Boundary Current and Adjacent Interior Circulation at 24°–30°N: Mean Structure and Mesoscale Variability. Journal of

Physical Oceanography, 50(9), 2735–2758. https://doi.org/10.1175/JPO-D-20-0094.1

Bonou, F., Dossa, A. N., Dahunsi, A. M., & Sohou, Z. (2024). Interannual and Seasonal Variability of CO2 Parameters in the Tropical Atlantic Ocean. Journal of Marine Science and Engineering, 12(12), 2248. https://doi.org/10.3390/jmse12122248

Bower, A., Lozier, S., Biastoch, A., Drouin, K., Foukal, N., Furey, H., et al. (2019). Lagrangian Views of the Pathways of the Atlantic Meridional Overturning Circulation. Journal of Geophysical Research: Oceans, 124(8), 5313–5335. https://doi.org/10.1029/2019JC015014

Bower, A. S., & Hunt, H. D. (2000). Lagrangian Observations of the Deep Western Boundary Current in the North Atlantic Ocean. Journal of Physical Oceanography, 30(5), 764–783. https://doi.org/10.1175/1520-0485(2000)030<0764:LOOTDW>2.0.CO;2

Bower, A. S., Lozier, M. S., Gary, S. F., & Böning, C. W. (2009). Interior pathways of the North Atlantic meridional overturning circulation. Nature, 459(7244), 243–247. https://doi.org/10.1038/nature07979

Brown, P. J., McDonagh, E. L., Sanders, R., Watson, A. J., Wanninkhof, R., King, B. A., et al. (2021). Circulation-driven variability of Atlantic anthropogenic carbon transports and uptake. Nature Geoscience, 14(8), 571–577. https://doi.org/10.1038/s41561-021-00774-5

Bryden, harry L., Johns, W. E., & Saunders, P. M. (2005). Deep western boundary current east of Abaco: Mean structure and transport. Journal of Marine Research, 63(1), 35–57. https://doi.org/10.1357/0022240053693806

Caínzos, V., Hernández-Guerra, A., McCarthy, G. D., McDonagh, E. L., Cubas Armas, M., & Pérez-Hernández, M. D. (2022). Thirty Years of GOSHIP and WOCE Data: Atlantic Overturning of Mass, Heat, and Freshwater Transport. Geophysical Research Letters, 49(4), e2021GL096527. https://doi.org/10.1029/2021GL096527

Caínzos, Verónica, Velo, A., Pérez, F. F., & Hernández-Guerra, A. (2022). Anthropogenic Carbon Transport Variability in the Atlantic Ocean Over Three Decades. Global Biogeochemical Cycles, 36(11), e2022GB007475. https://doi.org/10.1029/2022GB007475

Caínzos, Verónica, Pérez-Hernández, M. D., Santana-Toscano, D., Arumí-Planas, C., & Hernández-Guerra, A. (2023). Consistent picture of the horizontal circulation of the Atlantic Ocean over 3 decades. Ocean Science, 19(4), 1009–1045. https://doi.org/10.5194/os-19-1009-2023

Caínzos, Verónica, Hernández-Guerra, A., Farneti, R., Pérez-Hernández, M. D., & Talley, L. D. (2023). Mass, Heat, and Freshwater Transport From Transoceanic Sections in the Atlantic Ocean at 30°S and 24.5°N: Single Sections Versus Box Models? Geophysical Research Letters, 50(11), e2023GL103412. https://doi.org/10.1029/2023GL103412

Caldeira, K., & Wickett, M. E. (2003). Anthropogenic carbon and ocean pH. Nature, 425(6956), 365–365. https://doi.org/10.1038/425365a

Caldeira, K., & Wickett, M. E. (2005). Ocean model predictions of chemistry changes from carbon dioxide emissions to the atmosphere and ocean. Journal of Geophysical Research: Oceans, 110(C9), 1–12. https://doi.org/10.1029/2004JC002671

Casanova-Masjoan, M., Joyce, T. M., Pérez-Hernández, M. D., Vélez-Belchí, P., & Hernández-Guerra, A. (2018). Changes across 66°W, the Caribbean Sea and the Western boundaries of the North Atlantic Subtropical Gyre. Progress in Oceanography, 168, 296–309. https://doi.org/10.1016/j.pocean.2018.09.013

Casanova-Masjoan, M., Pérez-Hernández, M. D., Pickart, R. S., Valdimarsson, H., Ólafsdóttir, S. R., Macrander, A., et al. (2020). Along-Stream, Seasonal, and Interannual Variability of the North Icelandic Irminger Current and East Icelandic Current Around Iceland. Journal of Geophysical Research: Oceans, 125(9), e2020JC016283. https://doi.org/10.1029/2020JC016283

Chomiak, L., Volkov, D., & Schmid, C. (2023). The interior spreading story of Labrador Sea Water. Frontiers in Marine Science, 10, 1270463. https://doi.org/10.3389/FMARS.2023.1270463/BIBTEX

Chomiak, L. N., Yashayaev, I., Volkov, D. L., Schmid, C., & Hooper, J. A. (2022). Inferring Advective Timescales and Overturning Pathways of the Deep Western Boundary Current in the North Atlantic Through Labrador Sea Water Advection. Journal of Geophysical Research: Oceans, 127(12), e2022JC018892. https://doi.org/10.1029/2022JC018892

Comas-Rodríguez, I., Hernández-Guerra, A., & McDonagh, E. L. (2010). Referencing geostrophic velocities using ADCP data Referencing geostrophic velocities using ADCP data. Scientia Marina, 74(2), 331–338. https://doi.org/10.3989/scimar.2010.74n2331

Curbelo-Hernández, D., Pérez, F. F., González-Dávila, M., Gladyshev, S. V., González, A. G., González-Santana, D., et al. (2024, June 11). Ocean Acidification trends and Carbonate System dynamics in the North Atlantic Subpolar Gyre during 2009–2019. https://doi.org/10.5194/egusphere-2024-1388

Doney, S. C., Fabry, V. J., Feely, R. A., & Kleypas, J. A. (2009). Ocean Acidification: The Other CO2 Problem. Annual Review of Marine Science, 1(1), 169–192. https://doi.org/10.1146/annurev.marine.010908.163834

Doney, S. C., Busch, D. S., Cooley, S. R., & Kroeker, K. J. (2020). The impacts of ocean acidification on marine ecosystems and reliant human communities. Annual Review of Environment and Resources, 45(Volume 45, 2020), 83–112. https://doi.org/10.1146/ANNUREV-ENVIRON-012320-083019/CITE/REFWORKS

Dossa, A. N., Silva, A. C., Chaigneau, A., Eldin, G., Araujo, M., & Bertrand, A. (2021). Near-surface western boundary circulation off Northeast Brazil. Progress in Oceanography, 190, 102475. https://doi.org/10.1016/j.pocean.2020.102475

Feely, R. A., Sabine, C. L., Lee, K., Berelson, W., Kleypas, J., Fabry, V. J., & Millero, F. J. (2004). Impact of anthropogenic CO2 on the CaCO3 system in the oceans. Science, 305(5682), 362–366. https://doi.org/10.1126/SCIENCE.1097329/SUPPL_FILE/FEELY.SOM.PDF

Fischer, J., & Schott, F. A. (2002). Labrador Sea Water Tracked by Profiling Floats—From the Boundary Current into the Open North Atlantic. Journal of Physical Oceanography, 32(2), 573–584. https://doi.org/10.1175/1520-0485(2002)032<0573:LSWTBP>2.0.CO;2

Forget, G., Campin, J.-M., Heimbach, P., Hill, C. N., Ponte, R. M., & Wunsch, C. (2015). ECCO version 4: an integrated framework for non-linear inverse modeling and global ocean state estimation. Geoscientific Model Development, 8(10), 3071–3104. https://doi.org/10.5194/gmd-8-3071-2015

Friedlingstein, P., O’Sullivan, M., Jones, M. W., Andrew, R. M., Bakker, D. C. E., Hauck, J., et al. (2023). Global Carbon Budget 2023. Earth System Science Data, 15(12), 5301–5369. https://doi.org/10.5194/essd-15-5301-2023

Fukumori, I., Wang, O., Fenty, I., Forget, G., Heimbach, P., & Ponte, R. M. (2021). Synopsis of the ECCO Central Production Global Ocean and Sea-Ice State Estimate, Version 4 Release 4. https://doi.org/10.5281/ZENODO.4533349

Ganachaud, A. (2003). Large-scale mass transports, water mass formation, and diffusivities estimated from World Ocean Circulation Experiment (WOCE) hydrographic data. Journal of Geophysical Research: Oceans, 108(C7). https://doi.org/10.1029/2002JC001565

Ganachaud, A., & Wunsch, C. (2000). Improved estimates of global ocean circulation, heat transport and mixing from hydrographic data. Nature, 408(6811), 453–457. https://doi.org/10.1038/35044048

García-Ibáñez, M. I., Zunino, P., Fröb, F., Carracedo, L. I., Ríos, A. F., Mercier, H., et al. (2016). Ocean acidification in the subpolar North Atlantic: rates and mechanisms controlling pH changes. Biogeosciences, 13(12), 3701–3715. https://doi.org/10.5194/bg-13-3701-2016

Gary, S. F., Susan Lozier, M., Böning, C. W., & Biastoch, A. (2011). Deciphering the pathways for the deep limb of the Meridional Overturning Circulation. Deep Sea Research Part II: Topical Studies in Oceanography, 58(17–18), 1781–1797. https://doi.org/10.1016/j.dsr2.2010.10.059

Garzoli, S. L., Ffield, A., Johns, W. E., & Yao, Q. (2004). North Brazil Current retroflection and transports. Journal of Geophysical Research: Oceans, 109(C1), C01013. https://doi.org/10.1029/2003JC001775

Gattuso, J. P., Magnan, A., Billé, R., Cheung, W. W. L., Howes, E. L., Joos, F., et al. (2015). Contrasting futures for ocean and society from different anthropogenic CO2 emissions scenarios. Science, 349(6243). https://doi.org/10.1126/SCIENCE.AAC4722/SUPPL_FILE/GATTUSO.SM.PDF

Gruber, N., Sarmiento, J. L., & Stocker, T. F. (1996). An improved method for detecting anthropogenic CO2 in the oceans. Global Biogeochemical Cycles, 10(4), 809–837. https://doi.org/10.1029/96GB01608

Gruber, N., Clement, D., Carter, B. R., Feely, R. A., van Heuven, S., Hoppema, M., et al. (2019a). The oceanic sink for anthropogenic CO2 from 1994 to 2007. Science, 363(6432), 1193–1199. https://doi.org/10.1126/science.aau5153
Gruber, N., Clement, D., Carter, B. R., Feely, R. A., van Heuven, S., Hoppema, M., et al. (2019b). The oceanic sink for anthropogenic CO2 from 1994 to 2007. Science, 363(6432), 1193–1199. https://doi.org/10.1126/science.aau5153
Guinotte, J. M., Orr, J., Cairns, S. D., Freiwald, A., Morgan, L., & George, R. (2006). Will human-induced changes in seawater chemistry alter the distribution of deep-sea scleractinian corals? https://doi.org/10.1890/1540-9295(2006)004
Hall, M. M., Joyce, T. M., Pickart, R. S., Smethie, W. M., & Torres, D. J. (2004). Zonal circulation across 52°W in the North Atlantic. Journal of Geophysical Research: Oceans, 109(C11), C11008. https://doi.org/10.1029/2003JC002103
Hátún, H., Sandø, A. B., Drange, H., Hansen, B., & Valdimarsson, H. (2005). Influence of the Atlantic Subpolar Gyre on the Thermohaline Circulation. Science, 309(5742), 1841–1844. https://doi.org/10.1126/science.1114777
Hellerman, S. (1980). Charts of the Variability of the Wind Stress over the Tropical Atlantic. In Oceanography and Surface Layer Meteorology in the B/C Scale (pp. 63–75). Elsevier. https://doi.org/10.1016/B978-1-4832-8366-1.50022-4
Hernández-Guerra, A., & Joyce, T. M. (2000). Water masses and circulation in the surface layers of the Caribbean at 66°W. Geophysical Research Letters, 27(21), 3497–3500. https://doi.org/10.1029/1999GL011230
Hernández-Guerra, A, Machín, F., Antoranz, A., Cisneros-Aguirre, J., Gordo, C., Marrero-Díaz, A., et al. (2002). Temporal variability of mass transport in the Canary Current. Deep Sea Research Part II: Topical Studies in Oceanography, 49(17), 3415–3426. https://doi.org/10.1016/S0967-0645(02)00092-9
Hernández-Guerra, A., Fraile-Nuez, E., López-Laatzen, F., Martínez, A., Parrilla, G., & Vélez-Belchí, P. (2005). Canary Current and North Equatorial Current from an inverse box model. Journal of Geophysical Research: Oceans, 110(C12), 1–16. https://doi.org/10.1029/2005JC003032
Hernández-Guerra, Alonso, & Talley, L. D. (2016). Meridional overturning transports at 30°S in the Indian and Pacific Oceans

in 2002–2003 and 2009. Progress in Oceanography, 146, 89–120. https://doi.org/10.1016/j.pocean.2016.06.005

Hernández-Guerra, Alonso, Joyce, T. M., Fraile-Nuez, E., & Vélez-Belchí, P. (2010). Using Argo data to investigate the Meridional Overturning Circulation in the North Atlantic. Deep Sea Research Part I: Oceanographic Research Papers, 57(1), 29–36. https://doi.org/10.1016/j.dsr.2009.10.003

Hernández-Guerra, Alonso, Pelegrí, J. L., Fraile-Nuez, E., Benítez-Barrios, V., Emelianov, M., Pérez-Hernández, M. D., & Vélez-Belchí, P. (2014). Meridional overturning transports at 7.5N and 24.5N in the Atlantic Ocean during 1992–93 and 2010–11. Progress in Oceanography, 128, 98–114. https://doi.org/10.1016/j.pocean.2014.08.016

Hernández-Guerra, Alonso, Talley, L. D., Pelegrí, J. L., Vélez-Belchí, P., Baringer, M. O., Macdonald, A. M., & McDonagh, E. L. (2019). The upper, deep, abyssal and overturning circulation in the Atlantic Ocean at 30°S in 2003 and 2011. Progress in Oceanography, 176, 102136. https://doi.org/10.1016/j.pocean.2019.102136

Jackett, D. R., & McDougall, T. J. (1997). A Neutral Density Variable for the World's Oceans. Journal of Physical Oceanography, 27(2), 237–263. https://doi.org/10.1175/1520-0485(1997)027<0237:ANDVFT>2.0.CO;2

Johns, W. E., Lee, T. N., Beardsley, R. C., Candela, J., Limeburner, R., & Castro, B. (1998). Annual Cycle and Variability of the North Brazil Current. Journal of Physical Oceanography, 28(1), 103–128. https://doi.org/10.1175/1520-0485(1998)028<0103:ACAVOT>2.0.CO;2

Johns, W. E., Beal, L. M., Baringer, M. O., Molina, J. R., Cunningham, S. A., Kanzow, T., & Rayner, D. (2008a). Variability of Shallow and Deep Western Boundary Currents off the Bahamas during 2004–05: Results from the 26°N RAPID–MOC Array. Journal of Physical Oceanography, 38(3), 605–623. https://doi.org/10.1175/2007JPO3791.1

Johns, W. E., Beal, L. M., Baringer, M. O., Molina, J. R., Cunningham, S. A., Kanzow, T., & Rayner, D. (2008b). Variability of Shallow and Deep Western Boundary Currents off the Bahamas during 2004–05: Results from the 26°N RAPID–MOC Array. Journal of Physical Oceanography, 38(3), 605–623. https://doi.org/10.1175/2007JPO3791.1

Johnson, G. C., Lumpkin, R., Atkinson, C., Biló, T., Boyer, T., Bringas, F., et al. (2023). Global Oceans. Bulletin of the American Meteorological Society, 104(9), S146–S206. https://doi.org/10.1175/BAMS-D-23-0076.2

Joyce, T. M., & Zhang, R. (2010). On the Path of the Gulf Stream and the Atlantic Meridional Overturning Circulation. Journal of Climate, 23(11), 3146–3154. https://doi.org/10.1175/2010JCLI3310.1

Joyce, T. M., Pickart, R. S., & Millard, R. C. (1999). Long-term hydrographic changes at 52 and 66°W in the North Atlantic Subtropical Gyre & Caribbean. Deep Sea Research Part II: Topical Studies in Oceanography, 46(1–2), 245–278. https://doi.org/10.1016/S0967-0645(98)00102-7

Joyce, T. M., Hernandez-Guerra, A., & Smethie, W. M. (2001). Zonal circulation in the NW Atlantic and Caribbean from a meridional World Ocean Circulation Experiment hydrographic section at 66°W. Journal of Geophysical Research: Oceans, 106(C10), 22095–22113. https://doi.org/10.1029/2000JC000268

Joyce, T. M., Thomas, L. N., Dewar, W. K., & Girton, J. B. (2013). Eighteen Degree Water formation within the Gulf Stream during CLIMODE. Deep Sea Research Part II: Topical Studies in Oceanography, 91, 1–10. https://doi.org/10.1016/j.dsr2.2013.02.019

Kanamitsu, M., Ebisuzaki, W., Woollen, J., Yang, S.-K., Hnilo, J. J., Fiorino, M., & Potter, G. L. (2002). NCEP–DOE AMIP-II Reanalysis (R-2). Bulletin of the American Meteorological Society, 83(11), 1631–1644. https://doi.org/10.1175/BAMS-83-11-1631

Khatiwala, S., Primeau, F., & Hall, T. (2009). Reconstruction of the history of anthropogenic CO2 concentrations in the ocean. Nature, 462(7271), 346–349. https://doi.org/10.1038/nature08526

Khatiwala, S., Tanhua, T., Mikaloff Fletcher, S., Gerber, M., Doney, S. C., Graven, H. D., et al. (2013). Global ocean storage of anthropogenic carbon. Biogeosciences, 10(4), 2169–2191. https://doi.org/10.5194/bg-10-2169-2013

Leaman, K. D., Johns, E., & Rossby, T. (1989). The Average Distribution of Volume Transport and Potential Vorticity with Temperature at Three Sections across the Gulf Stream. Journal of Physical Oceanography, 19(1), 36–51.

https://doi.org/10.1175/1520-0485(1989)019<0036:TADOVT>2.0.CO;2

Lee, T., & Cornillon, P. (1995). Temporal variation of meandering intensity and domain-wide lateral oscillations of the Gulf Stream. Journal of Geophysical Research: Oceans, 100(C7), 13603–13613. https://doi.org/10.1029/95JC01219

Lellouche, J.-M., Greiner, E., Le Galloudec, O., Garric, G., Regnier, C., Drevillon, M., et al. (2018). Recent updates to the Copernicus Marine Service global ocean monitoring and forecasting real-time 1/12° high-resolution system. Ocean Science, 14(5), 1093–1126. https://doi.org/10.5194/os-14-1093-2018

Li, X., Wu, Z., Ouyang, Z., & Cai, W.-J. (2024). The source and accumulation of anthropogenic carbon in the U.S. East Coast. Science Advances, 10(32). https://doi.org/10.1126/sciadv.adl3169

Matear, R. J., Wong, C. S., & Xie, L. (2003). Can CFCs be used to determine anthropogenic CO2? Global Biogeochemical Cycles, 17(1). https://doi.org/10.1029/2001GB001415

Meinen, C. S., & Garzoli, S. L. (2014). Attribution of Deep Western Boundary Current variability at 26.5°N. Deep Sea Research Part I: Oceanographic Research Papers, 90(1), 81–90. https://doi.org/10.1016/j.dsr.2014.04.016

Meinen, C. S., Garzoli, S. L., Johns, W. E., & Baringer, M. O. (2004). Transport variability of the Deep Western Boundary Current and the Antilles Current off Abaco Island, Bahamas. Deep Sea Research Part I: Oceanographic Research Papers, 51(11), 1397–1415. https://doi.org/10.1016/j.dsr.2004.07.007

Meinen, C. S., Baringer, M. O., & Garcia, R. F. (2010). Florida Current transport variability: An analysis of annual and longer-period signals. Deep Sea Research Part I: Oceanographic Research Papers, 57(7), 835–846. https://doi.org/10.1016/j.dsr.2010.04.001

Meinen, C. S., Johns, W. E., Moat, B. I., Smith, R. H., Johns, E. M., Rayner, D., et al. (2019). Structure and Variability of the Antilles Current at 26.5°N. Journal of Geophysical Research: Oceans, 124(6), 3700–3723. https://doi.org/10.1029/2018JC014836

Munk, W. H. (1950). On the Wind-Driven Ocean Circulation. Journal of Meteorology, 7(2), 80–93. https://doi.org/10.1175/1520-0469(1950)007<0080:OTWDOC>2.0.CO;2

Orr, J. C., Fabry, V. J., Aumont, O., Bopp, L., Doney, S. C., Feely, R. A., et al. (2005). Anthropogenic ocean acidification over the twenty-first century and its impact on calcifying organisms. Nature, 437(7059), 681–686. https://doi.org/10.1038/nature04095

Pérez, F. F., Vázquez-Rodríguez, M., Louarn, E., Padín, X. A., Mercier, H., & Ríos, A. F. (2008). Temporal variability of the anthropogenic CO2 storage in the Irminger Sea. Biogeosciences, 5(6), 1669–1679. https://doi.org/10.5194/bg-5-1669-2008

Pérez, F. F., Vázquez-Rodríguez, M., Mercier, H., Velo, A., Lherminier, P., & Ríos, A. F. (2010). Trends of anthropogenic CO2 storage in North Atlantic water masses. Biogeosciences, 7(5), 1789–1807. https://doi.org/10.5194/bg-7-1789-2010

Perez, F. F., Fontela, M., García-Ibáñez, M. I., Mercier, H., Velo, A., Lherminier, P., et al. (2018). Meridional overturning circulation conveys fast acidification to the deep Atlantic Ocean. Nature, 554(7693), 515–518. https://doi.org/10.1038/nature25493

Pérez, Fiz F., Mercier, H., Vázquez-Rodríguez, M., Lherminier, P., Velo, A., Pardo, P. C., et al. (2013). Atlantic Ocean CO2 uptake reduced by weakening of the meridional overturning circulation. Nature Geoscience, 6(2), 146–152. https://doi.org/10.1038/ngeo1680

Pérez-Hernández, M. D., & Joyce, T. M. (2014). Two modes of Gulf Stream variability revealed in the last two decades of satellite altimeter data. Journal of Physical Oceanography, 44(1), 149–163. https://doi.org/10.1175/JPO-D-13-0136.1

Pérez-Hernández, M. D., Hernández-Guerra, A., Cana-Cascallar, L., Arumí-Planas, C., Caínzos, V., González-Santana, A. J., et al. (2023). The Seasonal Cycle of the Eastern Boundary Currents of the North Atlantic Subtropical Gyre. Journal of Geophysical Research: Oceans, 128(4). https://doi.org/10.1029/2022JC019487

Pérez-Hernández, M. Dolores, Hernández-Guerra, A., Fraile-Nuez, E., Comas-Rodríguez, I., Benítez-Barrios, V. M., Domínguez-Yanes, J. F., et al. (2013). The source of the Canary current in fall 2009. Journal of Geophysical Research: Oceans, 118(6), 2874–2891. https://doi.org/10.1002/jgrc.20227

Pérez-Hernández, M. Dolores, Pickart, R. S., Torres, D. J., Bahr, F., Sundfjord, A., Ingvaldsen, R., Renner, A. H. H., Beszczynska-

Möller, A., Appen, W., et al. (2019). Structure, Transport, and Seasonality of the Atlantic Water Boundary Current North of Svalbard: Results From a Yearlong Mooring Array. Journal of Geophysical Research: Oceans, 124(3), 1679–1698. https://doi.org/10.1029/2018JC014759

Pérez-Hernández, M. Dolores, Pickart, R. S., Torres, D. J., Bahr, F., Sundfjord, A., Ingvaldsen, R., Renner, A. H. H., Beszczynska-Möller, A., von Appen, W., et al. (2019). Structure, Transport, and Seasonality of the Atlantic Water Boundary Current North of Svalbard: Results From a Yearlong Mooring Array. Journal of Geophysical Research: Oceans, 124(3), 1679–1698. https://doi.org/10.1029/2018JC014759

Raven, J., Caldeira, K., Elderfield, H., Hoegh-Guldberg, O., Liss, P., Riebesell, U., et al. (2005). Ocean acidification due to increasing atmospheric carbon dioxide, 60. Retrieved from https://royalsociety.org/topics-policy/publications/2005/ocean-acidification/

Rayner, D., Hirschi, J. J.-M., Kanzow, T., Johns, W. E., Wright, P. G., Frajka-Williams, E., et al. (2011). Monitoring the Atlantic meridional overturning circulation. Deep Sea Research Part II: Topical Studies in Oceanography, 58(17–18), 1744–1753. https://doi.org/10.1016/j.dsr2.2010.10.056

Reid, J. L. (1994). On the total geostrophic circulation of the North Atlantic Ocean: Flow patterns, tracers, and transports. Progress in Oceanography, 33(1), 1–92. https://doi.org/10.1016/0079-6611(94)90014-0

Sabine, C. L., Feely, R. A., Gruber, N., Key, R. M., Lee, K., Bullister, J. L., et al. (2004). The oceanic sink for anthropogenic CO2. Science, 305(5682), 367–371. https://doi.org/10.1126/SCIENCE.1097403/SUPPL_FILE/SABINE.SOM.PDF

Santana-Toscano, D., Pérez-Hernández, M. D., Macdonald, A. M., Arumí-Planas, C., Caínzos, V., & Hernández-Guerra, A. (2023a). Zonal circulation in the North Atlantic ocean at 52°W from WOCE-WHP and CLIVAR sections: 1997, 2003 and 2012. Progress in Oceanography, 216, 103069. https://doi.org/10.1016/j.pocean.2023.103069

Santana-Toscano, D., Pérez-Hernández, M. D., Macdonald, A. M., Arumí-Planas, C., Caínzos, V., & Hernández-Guerra, A. (2023b). Zonal circulation in the North Atlantic ocean at 52°W from WOCE-WHP and CLIVAR sections: 1997, 2003 and

2012. Progress in Oceanography, 216, 103069. https://doi.org/10.1016/j.pocean.2023.103069
Santana-Toscano, D., Pérez-Hernández, M. D., Arumí-Planas, C., & Hernández-Guerra, A. (2025). Estimating the western North Atlantic Subtropical Gyre zonal currents in 2021 through single- and three-box inverse models. Progress in Oceanography, 231, 103415. https://doi.org/10.1016/j.pocean.2025.103415
Schott, F. A., Zantopp, R., Stramma, L., Dengler, M., Ju¨, J., Fischer, J., & Wibaux, M. (2004). Circulation and Deep-Water Export at the Western Exit of the Subpolar North Atlantic. Journal of Physical Oceanography, 34(4), 817–843. https://doi.org/10.1175/1520-0485(2004)034
Schott, F. A., Dengler, M., Zantopp, R., Stramma, L., Fischer, J., & Brandt, P. (2005). The Shallow and Deep Western Boundary Circulation of the South Atlantic at 5°–11°S. Journal of Physical Oceanography, 35(11), 2031–2053. https://doi.org/10.1175/JPO2813.1
Van Sebille, E., Baringer, M. O., Johns, W. E., Meinen, C. S., Beal, L. M., Femke De Jong, M., et al. (2011). Propagation pathways of classical Labrador Sea water from its source region to 26°N. Journal of Geophysical Research: Oceans, 116(C12), 12027. https://doi.org/10.1029/2011JC007171
da Silveira, I. C. A., de Miranda, L. B., & Brown, W. S. (1994). On the origins of the North Brazil Current. Journal of Geophysical Research: Oceans, 99(C11), 22501–22512. https://doi.org/10.1029/94JC01776
Spall, M. A. (1996). Dynamics of the Gulf Stream/Deep Western Boundary Current Crossover. Part I: Entrainment and Recirculation. Journal of Physical Oceanography, 26(10), 2152–2168. https://doi.org/10.1175/1520-0485(1996)026<2152:DOTGSW>2.0.CO;2
Stewart, K. D., Kim, W. M., Urakawa, S., Hogg, A. McC., Yeager, S., Tsujino, H., et al. (2020). JRA55-do-based repeat year forcing datasets for driving ocean–sea-ice models. Ocean Modelling, 147, 101557. https://doi.org/10.1016/j.ocemod.2019.101557
Stommel, H. (1948). The westward intensification of wind-driven ocean currents. Eos, Transactions American Geophysical Union, 29(2), 202–206. https://doi.org/10.1029/TR029i002p00202

Stommel, H., Arons, A. B., & Faller, A. J. (1958). Some Examples of Stationary Planetary Flow Patterns in Bounded Basins. Tellus A: Dynamic Meteorology and Oceanography, 10(2), 179–187. https://doi.org/10.3402/tellusa.v10i2.9238

Stramma, L. (1984). Geostrophic transport in the Warm Water Sphere of the eastern subtropical North Atlantic. Journal of Marine Research, 42(3), 537–558. https://doi.org/10.1357/002224084788506022

Stramma, L., Fischer, J., & Reppin, J. (1995). The North Brazil Undercurrent. Deep-Sea Research 1, 42(5), 773–795.

Talley, L. D., Pickard, G. L., Emery, W. J., & Swift, J. H. (2011). Descriptive physical oceanography : an introduction. (Elsevier, Ed.) (Sixth Edit). Academic Press.

Talley, L. D., Feely, R. A., Sloyan, B. M., Wanninkhof, R., Baringer, M. O., Bullister, J. L., et al. (2016). Changes in Ocean Heat, Carbon Content, and Ventilation: A Review of the First Decade of GO-SHIP Global Repeat Hydrography. Annual Review of Marine Science, 8(1), 185–215. https://doi.org/10.1146/annurev-marine-052915-100829

Thomas, H., & Ittekkot, V. (2001). Determination of anthropogenic CO2 in the North Atlantic Ocean using water mass ages and CO2 equilibrium chemistry. Journal of Marine Systems, 27(4), 325–336. https://doi.org/10.1016/S0924-7963(00)00077-4

Thoning, K. W., Crotwell, A. M., & Mund, J. W. (2024, July 6). Atmospheric Carbon Dioxide Dry Air Mole Fractions from continuous measurements at Mauna Loa, Hawaii, Barrow, Alaska, American Samoa and South Pole, 1973-present. https://doi.org/https://doi.org/10.15138/YAF1-BK21

Toole, J.M., Curry, R. G., Joyce, T. M., McCartney, M., & Peña-Molino, B. (2011). Transport of the North Atlantic Deep Western Boundary Current about 39°N, 70°W: 2004–2008. Deep Sea Research Part II: Topical Studies in Oceanography, 58(17–18), 1768–1780. https://doi.org/10.1016/j.dsr2.2010.10.058

Toole, John M., Andres, M., Le Bras, I. A., Joyce, T. M., & McCartney, M. S. (2017). Moored observations of the Deep Western Boundary Current in the NW Atlantic: 2004–2014. Journal of Geophysical Research: Oceans, 122(9), 7488–7505. https://doi.org/10.1002/2017JC012984

Touratier, F., Azouzi, L., & Goyet, C. (2007). CFC-11, 14C and H tracers as a means to assess anthropogenic CO2 concentrations

in the ocean. Tellus B, 59(2), 318–325. https://doi.org/10.1111/j.1600-0889.2006.00247.x
Tracey, K. L., & Watts, D. R. (1986). On Gulf Stream meander characteristics near Cape Hatteras. Journal of Geophysical Research: Oceans, 91(C6), 7587–7602. https://doi.org/10.1029/JC091iC06p07587
Tsujino, H., Urakawa, L. S., Griffies, S. M., Danabasoglu, G., Adcroft, A. J., Amaral, A. E., et al. (2020). Evaluation of global ocean–sea-ice model simulations based on the experimental protocols of the Ocean Model Intercomparison Project phase 2 (OMIP-2). Geoscientific Model Development, 13(8), 3643–3708. https://doi.org/10.5194/gmd-13-3643-2020
Våge, K., Pickart, R. S., Spall, M. A., Moore, G. W. K., Valdimarsson, H., Torres, D. J., et al. (2013). Revised circulation scheme north of the Denmark Strait. Deep Sea Research Part I: Oceanographic Research Papers, 79, 20–39. https://doi.org/10.1016/j.dsr.2013.05.007
Vázquez-Rodríguez, M., Touratier, F., Lo Monaco, C., Waugh, D. W., Padin, X. A., Bellerby, R. G. J., et al. (2009). Anthropogenic carbon distributions in the Atlantic Ocean: data-based estimates from the Arctic to the Antarctic. Biogeosciences, 6(3), 439–451. https://doi.org/10.5194/bg-6-439-2009
Vélez-Belchí, P., Pérez-Hernández, M. D., Casanova-Masjoan, M., Cana, L., & Hernández-Guerra, A. (2017). On the seasonal variability of the Canary Current and the Atlantic Meridional Overturning Circulation. Journal of Geophysical Research: Oceans, 122(6), 4518–4538. https://doi.org/10.1002/2017JC012774
Waugh, D. W., Hall, T. M., McNeil, B. I., Key, R., & Matear, R. J. (2006). Anthropogenic CO2 in the oceans estimated using transit time distributions. Tellus B: Chemical and Physical Meteorology, 58(5), 376. https://doi.org/10.1111/j.1600-0889.2006.00222.x
Worthington, L. V. (1976). On the North Atlantic circulation.
Wunsch, C. (1996). The Steady Ocean Circulation Inverse Problem. In The Ocean Circulation Inverse Problem (pp. 212–296). Cambridge University Press. https://doi.org/10.1017/CBO9780511629570.006
Wunsch, Carl. (1978). The North Atlantic general circulation west of 50°W determined by inverse methods. Reviews of Geophysics, 16(4), 583–620. https://doi.org/10.1029/RG016i004p00583